Lehrstuhl für Methodik der Fernerkundung
Ingenieurfakultät Bau Geo Umwelt

From laboratory spectroscopy to remote sensing: Methods for the retrieval of water constituents in optically complex waters

Anna Theresa Göritz

Vollständiger Abdruck der von der Ingenieurfakultät Bau Geo Umwelt der Technischen Universität München zur Erlangung des akademischen Grades eines

Doktor-Ingenieurs (Dr.-Ing.)

genehmigten Dissertation.

Vorsitzende:

Univ.-Prof. Dr.-Ing. habil. Xiaoxiang Zhu

Prüfende der Dissertation:

1. Univ.-Prof. Dr.-Ing. habil. Richard Bamler
2. Univ.-Prof. Dr.rer.nat. Astrid Bracher
3. Univ.-Prof. Dr.rer.nat. habil. Alexander Damm (nur schriftliche Beurteilung)

Die Dissertation wurde am 18.07.2018 bei der Technischen Universität München eingereicht und durch die Ingenieurfakultät Bau Geo Umwelt am 13.09.2018 angenommen.

Abstract

Optical remote sensing of water bodies allows for the spatio-temporal monitoring of water constituents such as phytoplankton or colored dissolved organic matter (CDOM). In optically complex waters as found in many inland and coastal waters, the analysis of the backscattered sunlight over water remains challenging. Recent satellites of high spatial resolution and advances in hyperspectral techniques are opening new possibilities for mapping these environments and potential threats such as toxic cyanobacteria blooms. For this purpose, inversion algorithms are applied which ultimately rely on the knowledge of the spectral characteristics of all optically active constituents. In case of cyanobacteria, these properties are highly variable which complicates their monitoring.

In order to characterize the spectral properties of cyanobacteria and their variability, a laboratory setup has been developed and validated (ENVILAB) which enables studies under well-defined and adjustable light, nutrient and temperature conditions. It consists of a light source, tunable in spectral composition and intensity, a photobioreactor and an automated sample transportation and measurement system. External instruments are linked to the photobioreactor which measure absorption and excitation-emission-fluorescence spectra. Spectral attenuation measurements through the bioreactor enable growth monitoring and time series analysis of spectral changes. The ENVILAB permits to systematically investigate the optical properties of phytoplankton and their variability. This information is required for the development of remote sensing algorithms, as well as to estimate and improve their accuracy. Furthermore, triggering factors for changes in the phytoplankton physiology can be studied.

CDOM is a major light absorber in many inland waters. Its fluorescence signatures are typically neglected in passive remote sensing. Moreover, its absorption strongly interferes with the spectral signatures of cyanobacteria and other phytoplankton. To better simulate the spectral features of CDOM, a bio-optical model has been developed. Building up on laboratory absorption and fluorescence measurements, the Gaussian Light Emission and Absorption Model (GLEAM) enables the coupled simulation of all relevant optical properties of CDOM: absorption coefficient, excitation-emission fluorescence radiance, and spectral fluorescence quantum efficiency. The GLEAM parametrization of the optical properties of CDOM can serve as input to radiative transfer modelling, making it of high value for remote sensing.

Abstract

Continuous water monitoring with spaceborne optical sensors, as required for water quality assessment or long term ecosystem studies, is often hampered by clouds. In a final contribution, the water constituent retrieval under variable cloud cover was addressed. Current retrieval methods usually presuppose clear skies. It was found that concentrations of CDOM and Chlorophyll-*a* (an indicator for phytoplankton such as cyanobacteria) can be retrieved from in-water irradiance measurements even under challenging weather conditions. Furthermore, a recently published glint model was extended by the inclusion of a component which accounts for cloud contribution to the surface reflectance signal. Different surface reflection correction procedures were compared and best performing approaches applied for water constituent retrieval. Although further investigation is required to disentangle the spectral contribution of surface reflection and water constituents, this study demonstrated the potential of linking in-water and above-water measurements and of the extended glint model for all-weather remote sensing from airborne systems, unmanned aerial vehicles (UAV) and measurement platforms or ships.

Zusammenfassung

Optische Fernerkundung ermöglicht die zeitliche und räumliche Beobachtung von Wasserinhaltsstoffen wie beispielsweise Phytoplankton oder Gelbstoff. In optisch komplexen Gewässern, wie zum Beispiel vielen Binnen- und küstennahen Gewässern, stellt die Analyse des rückgestreuten Lichts über Wasser eine große Herausforderung dar. Neueste Satelliten mit hoher räumlicher Auflösung sowie moderne Hyperspektraltechniken eröffnen jedoch neue Möglichkeiten, optisch komplexe Gewässer und mögliche Gefahren wie zum Beispiel giftige Cyanobakterien-Blüten zu erfassen. Hierzu werden Inversionsalgorithmen angewendet, welche auf der Kenntnis der spektralen Eigenschaften der optisch aktiven Wasserinhaltsstoffe basieren. Im Fall von Cyanobakterien sind diese Eigenschaften allerdings höchst variabel, was deren Beobachtung verkompliziert.

Um die spektralen Eigenschaften von Cyanobakterien und deren Variabilität zu untersuchen, wurde ein neuartiges Laborsystem entwickelt und validiert, das sog. ENVILAB. Dieses erlaubt Studien unter wohl definierten und einstellbaren Licht-, Nährstoff- und Temperaturbedingungen. Es besteht aus einer Lichtquelle, deren Spektrum und Intensität einstellbar sind, aus einem Photobioreaktor, und aus einem System zur automatischen Probenentnahme, Transport und spektralen Untersuchung. An den Photobioreaktor sind externe Geräte angeschlossen, welche Absorptions- und Anregungs-Emissions-Fluoreszenz-Spektren messen. Mit spektral aufgelösten Messungen der Lichttransmission durch den Bioreaktor hindurch lässt sich der zeitliche Verlauf des Bakterienwachstums und spektraler Veränderungen verfolgen. Das ENVILAB ermöglicht somit die systematische Erforschung der optischen Eigenschaften von Cyanobakterien sowie deren Variabilität. Diese Informationen werden für die Entwicklung von Fernerkundungsverfahren, sowie zur Bewertung und Verbesserung ihrer Genauigkeit benötigt. Des Weiteren lassen sich physiologische Veränderungen von Phytoplankton und deren Auslöser untersuchen.

Gelbstoff trägt in vielen Inlandgewässern maßgeblich zur Absorption des Lichtes bei. Fluoreszenz von Gelbstoff wird in der passiven Fernerkundung meist vernachlässigt. Zudem überlagert die Absorption von Gelbstoff die spektralen Signaturen von Cyanobakterien und anderem Phytoplankton. Um die spektralen Eigenschaften von Gelbstoff besser simulieren zu können, wurde ein bio-optisches Modell entwickelt (GLEAM). Dieses “Gauss’sche Licht Emissions-

und Absorptionsmodell" basiert auf Labormessungen der Absorption und der Fluoreszenz und erlaubt die gekoppelte Simulation aller relevanten optischen Parameter von Gelbstoff: den Absorptionskoeffizienten, der Anregungs-Emissions Fluoreszenz sowie der spektralen Quanteneffizienz der Fluoreszenz. Die Parametrisierung der optischen Eigenschaften von Gelbstoff durch das GLEAM kann als Input für Strahlungstransfer-Modellierungen benutzt werden. Dies macht es zu einem wertvollen Werkzeug für die Fernerkundung.

Die kontinuierliche Überwachung von Gewässern durch optische Sensoren aus dem All wird für die Wasserqualitäts-Beurteilung und für Langzeitstudien von Ökosystemen benötigt. Allerdings ist die Beobachtung aus dem All häufig aufgrund bewölkten Himmels unmöglich. Die dritte wissenschaftliche Arbeit dieser Dissertation befasst sich deshalb mit der Bestimmung von Wasserinhaltsstoffen unter variabler Bewölkung. Bisherige Methoden setzen üblicherweise wolkenlose Bedingungen voraus. Es konnte gezeigt werden, daß auch bei herausfordernden Lichtbedingungen die Konzentrationen von Gelbstoff und Chlorophyll-*a* (ein Indikator für Phytoplankton wie z.B. Cyanobakterien) aus der unter Wasser gemessenen Bestrahlungsstärke bestimmt werden können. Des Weiteren wurde ein kürzlich veröffentlichtes Modell für spektrale Oberflächenspiegelungen um eine Komponente erweitert, die die Reflexion von Wolken an der Wasseroberfläche berücksichtigt. Verschiedene Methoden zur Korrektur der Oberflächenspiegelungen wurden verglichen und die am besten funktionierenden Ansätze zur Wasserinhaltstoffbestimmung verwendet. Obwohl weitere Untersuchungen zur Entflechtung der spektralen Anteile von Oberflächenspiegelungen und Wasserinhaltstoffen am Fernerkundungs-Signal nötig sind, konnte die Studie das Potential von kombinierten unter- und über-Wasser Messungen sowie des erweiterten Reflexionsmodells für die All-Wetter Fernerkundung aus der Luft (z.B. von Flugzeugen oder Drohnen) oder vom Wasser aus zeigen.

Contents

List of Figures

1 Introduction

"Die sichtbaren Dinge bilden die Grundlage der Erkenntnis des Unsichtbaren."
"Appearances are a glimpse of the unseen."
Anaxagoras, approx. 500 - 428 B.C. (Diels, 1935; Kirk et al., 1983)

The way in which we perceive our surroundings shapes our understanding of the world. To obtain objective results, scientists rely on sensors to investigate their targets, from the microscopic to the astronomic scale. For observations on regional and global scales, these sensors are mounted on air- or spaceborne platforms. Above dictum pinpoints the challenges but also the potential of these remote sensing techniques: Appearances (i.e., measured signals) often only provide a glimpse of what information is hidden in them. At the same time, advances in signal recording and processing techniques can shed light on phenomena that would otherwise have remained obscure. Thus, remote sensing can help us to expand our knowledge on our world in general and on aquatic ecosystems in particular.

Earth observation using satellites and airborne sensor systems allows for a monitoring of the Earth' surface on a large spatial scale and on a recurrent basis. It enables the assessment of the planet's surface and a detection of its changes with respect to physical, biological, geological, chemical and anthropogenic impacts and transformations. Monitoring of water quality, biodiversity and bio-geochemical dynamics in freshwater resources and coastal zones is of great importance to many stakeholders including aquaculture and resource managers, environmental agencies, policy makers, and finally researchers who seek to unravel underlying ecosystem dynamics and understand sensitivities of water systems to environmental as well as anthropogenic impacts. Fourty years ago, the first satellite sensor for monitoring the ocean, the Coastal Zone Color Scanner (CZCS) was launched by National Aeronautics and Space Administration, U.S. (NASA). The sensor enabled a global estimation of phytoplankton pigments but was, despite its name, restricted mainly to open ocean monitoring (IOCCG, 2000, p.1). Optically more complex environments such as inland and coastal waters with substantial signal contribution from other compounds than phytoplankton (e.g. from Colored Dissolved Organic Matter (CDOM) or suspended matter) had to be omitted due to the low spatial and spectral resolution and sensitivity of the sensor. In the past decades, the field of ocean color analysis has evolved and new sensors with higher sensitivities and spectral resolution have been deployed.

At the same time, methods for information retrieval were continuously refined. Nevertheless, analysis of water systems in which spectral signatures of compounds interfere and partially mask each other remain challenging until today.
This thesis addresses the discrimination and quantification of water constituents in optically complex waters by means of their spectral signatures. Two main groups of water constituents will be focused on. On the one hand, CDOM as major light absorber in many inland waters. On the other hand, phytoplankton and, more specifically, cyanobacteria, which are of great concern with regards to water quality assessment.
In the next sections, a brief introduction to the motivation and scientific relevance of this thesis is presented, resulting in the statement of research objectives and leading to an outlook on the structure of this work.

1.1 Relevance of optically complex waters and their monitoring

Water systems in which light is substantially altered beyond the influence of phytoplankton alone are called optically complex. Sources of this complexity can be constituents such as colored dissolved organic matter or suspended matter, but also reflections of bottom subtrates, as is the case for shallow waters. Many inland waters and coastal areas are optically complex, which imposes additional demands to remote sensing information retrieval methods and sensor specification compared to open ocean waters (IOCCG, 2000, pp.17ff.). Inland waters include lakes, rivers, reservoirs and estuaries. They contain one of the most fundamental natural resources on our planet – freshwater, which is essential for all life. Based on remote sensing observations with LandSat imagery, Verpoorter et al. (2014) derived an estimate of about 117 million lakes (larger than 0.002 km^2), which corresponds to an area of 3.7% of the Earth's terrestrial surface (excluding glaciated regions). Despite their small fraction of surface coverage compared to the ocean, inland waters provide drinking water, food and space for farming, recreational areas, ways of transportation and are of importance to industry and urbanization (Dekker et al., 2017). In addition to their socio-economic significance, inland waters play an important role in global biogeochemical cycles (Tranvik et al., 2009; IPCC, 2013; Moss, 2012). Furthermore, freshwater ecosystems give home to a huge variety of animals and plants, supporting rich biodiversity (Dudgeon et al., 2006; Turak et al., 2017). Due to their sensitivity to environmental changes, they have been assigned an indicator function for human influence on the environment (UNEP, 2012; Williamson et al., 2008).
Coastal zones are often densly populated areas and provide economic, social and cultural benefits for humans (Cohen et al., 1997; Wong et al., 2014; Russi et al., 2016). They are very

productive ecosystems and, as the connection between terrestrial and oceanic environments, of great importance in the context of material and element cycles (Cracknell, 1999; Turpie, 2015; Dekker et al., 2017).
Both inland and coastal waters are threatened by various stressors ranging from climate change to human activities (UNEP, 2012; Vörösmarty et al., 2010; Poff et al., 2016; O'Reilly et al., 2015; Dudgeon et al., 2006; Paerl and Paul, 2012). Among others, risks of this stress include decreasing biodiversity and favoring conditions for harmful algae blooms. In this context, the term 'bloom' refers to a rapid or dense accumulation of phytoplankton or algae. Blooms of very high biomass, with mucilage production or associated with the release of toxins are called Harmful Algae Bloom (HAB)s (Pettersson and Pozdnyakov, 2013, p.3). HABs occur in both marine and freshwater environments and can lead to high biomass. High biomass can result in oxygen depletion and thus kill fish and invertebrates (Paerl and Otten, 2013). Furthermore, if they are accompanied by the production of toxic metabolites - as released for example in certain cyanobacteria dominated HABs - they can become a threat for both animal and human health. HABs therefore constitute a risk not only for the ecosystem but also to the water treatment industry, resource and aquaculture management, and for recreational use of water with associated consequences for tourism. Therefore, a reliable monitoring and identification of harmful algae such as potentially toxic cyanobacteria is crucial. Remote sensing offer spatio-temporal observation capabilities that can complement *in situ* measurements in water monitoring, but its application to cyanobacteria monitoring in optically complex waters is not straight-forward, as explained in the following sections.

1.2 Remote sensing of optically complex waters

Remote sensing can contribute to water quality and habitat monitoring by providing regular, large scale information on different water parameters and, in case of shallow areas, benthic substrates and water depth. Typical parameters derived with optical remote sensing include Chlorophyll-*a* concentration, as an indicator for nutrient levels and phytoplankton biomass, colored dissolved organic matter, suspended matter and Secchi disk depth as measure for visibility and turbidity (Dörnhöfer and Oppelt, 2016). In shallow areas, additional information on bottom depth (bathymetry) and bottom cover (such as macrophytes or corals) can be obtained [e.g. Dierssen et al. (2003); Lesser and Mobley (2007); Hedley et al. (2016)]. Depending on the remote sensing data available, the type of sensor it was acquired with and the water composition, even different groups of phytoplankton can be distinguished [e.g. Bracher et al. (2009); IOCCG (2014); Gege (1997); Simis et al. (2005)].

With reflectance values in the visible wavelength range (VIS) of only a few and sometimes below one percent, aquatic ecosystems dominated by CDOM are presumably amongst the darkest targets in optical Earth observation (Lillesand et al., 2015; IOCCG, 2010; Giardino et al., 2013). The analysis of reflectance obtained over these optically complex environments rely on well calibrated sensors and very accurate correction of atmospheric effects. Furthermore, retrieval methods that can cope with large variations of in-water constituent concentration ranges as well as interfering spectral signatures are required (Gege, 2017). Recently, there has been significant progress in remote sensing of coastal and freshwater systems, pushing the limits of monitoring capabilities: Satellite missions such as the Copernicus twin satellites Sentinel-2A and -2B (launched in June 2015 and March 2016) with a spatial resolution of 10–20 m now allow for a regular mapping of coastal and a number of inland waters which could not be resolved in imagery of previous ocean color satellites. At the same time, there have been considerable advances in atmospheric correction and algorithm development, having "...led to marked improvements in the accuracy, applicability and robustness of remote sensing products for inland waters" (Palmer et al., 2015). Most recently (early 2018), an online portal has been launched which visualizes water quality information for lakes and rivers worldwide, derived from a test data set of Sentinel-2 and Landsat 8 satellite data (EOMAP, 2018; UNESCO, 2018). It demonstrates the spatio-temporal potential of current satellites for inland water quality mapping and serves as an interactive capacity training website.

Several recent studies discuss the potential and also requirements for biodiversity, coastal and inland water mapping with remote sensing (Bracher et al., 2017; Hestir et al., 2015b; Turpie et al., 2017; Muller-Karger et al., 2018; Dekker et al., 2017). There is an increasing need for higher spectral resolution in order to support aquatic ecosystem mapping. With hyperspectral techniques and new sensor technologies on the rise, a new chapter is opened for water constituent discrimination and therefore aquatic ecosystem mapping. Already today, a fascinating amount of information on in-water dynamics can be derived from satellite and airborne measurements despite low signals and spectral interferences. Recent multispectral missions such as Sentinel-2A (S-2A) have the impressive capability of resolving in-water processes driven by organisms of only a few micrometers in size from an altitude of more than 700 km (see the picture of a phytoplankton bloom in the Baltic Sea in Fig.1).

Optical remote sensing of water bodies relies on the detection of spectral signatures in backscattered sunlight that can be related to physical or chemical features such as size, geometry and molecular structure of in-water compounds. The penetration depth of light in water is mainly determined by the water absorption and the concentration and types of in-water constituents. It can range from roughly a hundred meters in very clear waters down to tens of meters or even a few centimeters in very turbid, highly absorbing waters (Stomp et al., 2007). The in-

formation contained in remote sensing signals is integrated over the water column illuminated by the penetrating sunlight. With the help of radiative transfer calculations it is possible from these integrated signals to infer water constituent concentrations or – in shallow areas – bottom properties and water depth.

Retrieval algorithms for remote sensing include empirical, statistical, machine learning and (semi-)analytical approaches (IOCCG, 2000, pp.47ff.). With the help of inversion models not only a classification of compounds, but also their quantitative contribution can be evaluated. These models, as for example implemented in the WAtercolor SImulation software (WASI), rely on specific optical properties which describe the absorption and scattering properties of in-water compounds in the VIS (Gege, 2014b, 2016). Thus, a sound knowledge of these spectral characteristics and their variability under changing external and internal conditions is crucial for a reliable water constituent retrieval.

It is the aim of this thesis to advance the spectral discrimination and quantification of water constituents, in order to improve the monitoring of optically complex waters. From this aim, three main objectives that constitute the guiding themes of this thesis can be derived, which will be formulated in the following section.

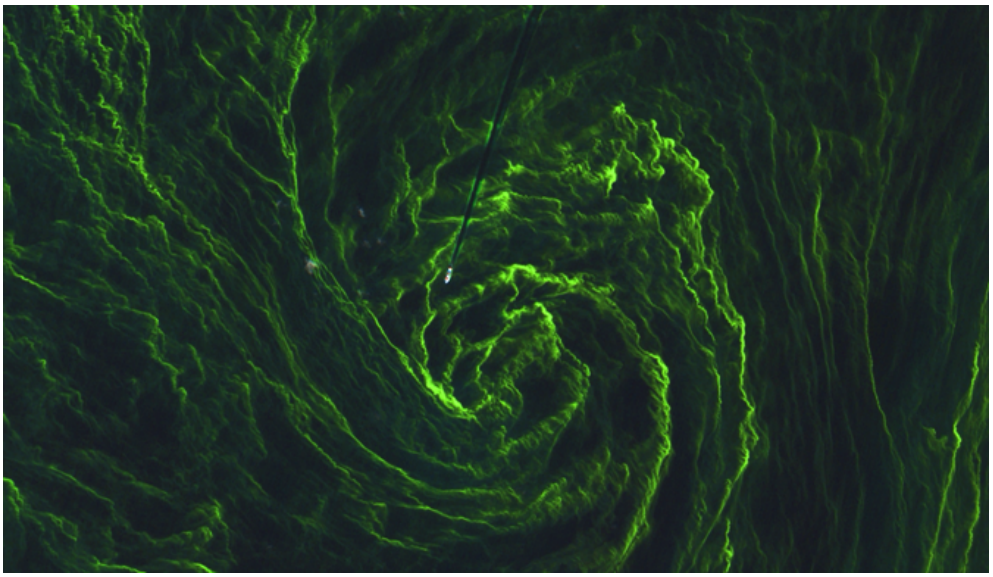

Figure 1: Phytoplankton bloom in the Baltic Sea crossed by a ship (black thin line in the upper center). The image was captured by Sentinel-2A on 7 August 2015 [Source: Copernicus Sentinel data (ESA, 2015)].

1.3 Aim and structure of this thesis

1.3.1 Objectives

In order to improve the classification and quantification of water constituents in optically complex waters, bio-optical models are required which describe the inherent optical properties of in-water constituents with a minimal set of parameters. For this purpose, information on the spectral variability is needed which enables a suitable parametrization, e.g., based on physical or chemical properties such as size and structure or chemical composition.
As explained in Section 1.1, there is a need for the identification and monitoring of potentially toxic cyanobacteria. Cyanobacteria species are capable of adapting their pigmentation, but little is known about the extent and triggering factors of these changes. However, this information is crucial for a reliable remote sensing identification algorithm and for the estimation of associated uncertainties.
What is more, the main identification characteristics in current classification algorithms for phytoplankton and CDOM detection are the specific absorption and backscattering coefficients. Due to restricted sensor capabilities, more complex spectral fluorescence characteristics are rarely considered, even though they can unveil molecular composition-specific information that may serve as additional and complementary discriminator.
While the working-horses of large scale and regular water monitoring are satellites, their effectiveness in the visible wavelengths is limited by the simple fact of cloud coverage. Therefore, sensor systems that are operated beneath clouds provide valuable information that can help to bridge this gap. Since most remote sensing data retrieval algorithms are based on clear-sky models, however, the necessity to adapt these models needs to be investigated.
With this situation in mind, the following objectives of this thesis can be stated:

(I) **Spectral phytoplankton characterization**
Cyanobacteria are typically identified in remote sensing according to their pigment specific absorption and backscattering coefficients. These coefficients have been shown to vary with both species and environmental conditions (Tandeau De Marsac, 1977; Stramski and Morel, 1990; Lutz et al., 2001; Stomp et al., 2004). Since environmental conditions in culture collections differ from natural environments (e.g., with respect to light availability and composition), samples grown in the laboratory usually exhibit very different properties as compared to natural samples. In order to measure the spectral parameters of cyanobacteria, a special laboratory environment is required which enables growth and optical measurements under controllable and systematically adjustable environmental conditions. Special attention shall be paid to light intensities and spectral composition as these are known to influence pigment composition. Furthermore, the

setup shall qualify for microbiological studies (e.g., for research on the toxin potential of certain species). Additionally, it shall include the possibility to record excitation-emission fluorescence which are rarely studied in the context of remote sensing applications.

(II) **Absorption and fluorescence signatures of CDOM**
CDOM is a major light absorber in many inland waters and an important water quality indicator. For a reliable water monitoring, its spectral signal needs to be disentangled from that of other water constituents. CDOM is typically characterized by its absorption coefficients. The latter's spectral shape is commonly described with an exponential decay from blue towards red wavelengths. This model is a simplification of the exact spectral signatures. In order to improve this description, laboratory measurements of the absorption and fluorescence-excitation emission characteristics shall be performed and analyzed with respect to common features. The overall goal is to develop a bio-optical model for CDOM which includes all relevant fluorescence features in order to improve the water constituent retrieval.

(III) **Water monitoring under variable weather conditions**
In order to investigate spatially resolved in-water dynamics of e.g., phytoplankton occurrence and bloom formation, observation capabilities need to be extended. Regular water monitoring using optical satellites is frequently hampered by the fact that clouds obstruct the view towards the Earth. In order to minimize observation gaps and to enable water quality assessment also under non-clear-sky conditions, existing methods need to be evaluated for their applicability to data from sensors operated below the cloud layer. For this purpose, water constituent retrieval from hyperspectral in- and above-water measurements recorded under variable weather conditions shall be performed, and ways for coping with variable surface reflections shall be explored.

1.3.2 Outline

The focus of this publication-based thesis lies on the optical discrimination and quantification of water constituents based on their spectral signatures. This touches upon several distinct but closely connected topics which are reported in separate chapters, according to the objectives (I–III) formulated above. The resulting structure of this thesis is as follows:
Chapter 2 is dedicated to the introduction of the underlying principles as well as the state of the art of spectral water constituent analysis and monitoring with optical remote sensing. In this chapter, the ground is laid for the subsequent presentation of the scientific contribution of this work.

The next chapter (**Chapter 3**) forms the main part of this thesis and presents a compilation and discussion of research results dedicated to the objectives formulated above: It describes the development, testing and assessment of a novel laboratory setup (ENVILAB) which enables systematic studies on changes in the absorption and fluorescence properties of phytoplankton and other water constituents (Chapter 3.1). Furthermore, a new analytical model (GLEAM) for the combined description of the spectral absorption and fluorescence of colored dissolved organic matter is presented (Chapter 3.2). Finally, the challenges of hyperspectral *in situ* measurements under variable illumination conditions are addressed, and the potential of an extended surface reflection model for above-water monitoring under clouds is assessed (Chapter 3.3). The thesis concludes in **Chapter 4** with a summary of the presented contributions, giving an outlook on possible future lines of research.

2 Background and state of the art

When light falls onto the Earth, the electromagnetic field interacts with its atmosphere and surface. The reflected portion of the light carries information on the medium it has passed and interacted with. In order to extract this information, suitable mathematical models need to be employed which relate the signal measured by a sensor (mounted, e.g., on a satellite) to the surface properties of interest.

Changes of the light field inside water can be modeled with the help of radiative transfer theory that describes the interaction of electromagnetic radiation with water and its constituents (Jerlov, 1976; Preisendorfer, 1976). The general vector radiative transfer equation presents a description of these three dimensional interaction processes. Typically, this equation is simplified under a number of assumptions, such as an isotropic, mirror symmetric medium and with only depth dependent water optical properties, which allows a reduction to a one-dimensional formulation. Neglecting polarization effects, finally a scalar approximation can be derived which is commonly used in hydrological modelling (Ocean Optics Webbook, 2018; Mobley, 1994):

$$\begin{aligned}\cos\theta \frac{dL(z,\theta,\varphi,\lambda)}{dz} &= -c(z,\lambda)L(z,\theta,\varphi,\lambda) \\ &+ \int_0^{2\pi}\int_0^{\pi} L(z,\theta',\varphi',\lambda)\beta(z;\theta',\varphi' \rightarrow \theta,\varphi;\lambda)\sin\theta' d\theta' d\varphi' \\ &+ \int_0^{2\pi}\int_0^{\pi} L(z,\theta',\varphi',\lambda')\beta_S(z;\theta,\varphi \rightarrow \theta',\varphi';\lambda' \rightarrow \lambda)\sin\theta' d\theta' d\varphi'.\end{aligned} \tag{2.1}$$

This equation describes the change in spectral radiance L [W m^{-2} sr^{-1} nm^{-1}] of light inside the water as a function of observation depth z, zenith angle θ, azimuth angle φ and wavelength λ. The first term on the right hand side of Eq. (2.1) represents the reduction of radiance due to the beam attenuation $c(z,\lambda)$. The second term, which is also referred to as path function (Gege, 2017), describes the light that is scattered into the beam. It depends on the volume scattering function $\beta(z;\theta',\varphi' \rightarrow \theta,\varphi;\lambda)$. The third term is another source term which summarizes emission processes such as fluorescence, bio-luminescence or Raman-scattering. Here, β_S stands for the respective source volume scattering function. The primed symbols in

Eq. (2.1) represent the initial direction (θ',φ') and the excitation wavelength (λ') for the trans-spectral processes. The latter are processes in which transitions between different wavelengths are involved.
This scalar radiative transfer equation thus links changes in radiance with the Inherent Optical Properties (IOPs) of the medium, such as the beam attenuation coefficient and the volume scattering function.

2.1 Inherent optical properties (IOPs)

IOPs are spectral properties that characterize a medium independently of the illumination and observation geometry. They may be considered as pure material properties, in contrast to Apparent Optical Properties (AOPs), such as reflectance, which vary with both the medium and the ambient light field (Preisendorfer, 1976, p.118).
When light passes through a medium, it is either transmitted, absorbed or scattered. Assuming an infinitesimally small layer of thickness dz, and a beam of parallel light that shines through this layer at a right angle, the transmitted photon flux ϕ_t is (Gege, 2017, pp.33ff.):

$$\phi_t = \phi - d\phi_a - d\phi_b, \tag{2.2}$$

where ϕ is the incident radiant flux and $d\phi_a$, $d\phi_b$ the infinitesimal losses due to absorption and scattering, respectively. In this picture, the absorption coefficient is then defined as:

$$a = \frac{1}{\phi}\frac{d\phi_a}{dz} \qquad \text{with } [a] = \mathrm{m}^{-1}. \tag{2.3}$$

Analogously, the definition of the scattering coefficient is given by:

$$b = \frac{1}{\phi}\frac{d\phi_b}{dz} \qquad \text{with } [b] = \mathrm{m}^{-1}. \tag{2.4}$$

With the scattering angle Ψ between the incident and scattered light beams and the azimuth angle φ, the scattering coefficient b and the backscattering coefficient b_b can be obtained from the volume scattering function $\beta(\Psi)$ (in [$\mathrm{m}^{-1}\mathrm{sr}^{-1}$]) by integration over all directions or all backwards directions:

$$b = \int_0^{2\pi}\int_0^{\pi} \beta(\psi)\sin(\psi)d\psi d\varphi = 2\pi\int_0^{\pi} \beta(\psi)\sin(\psi)d\psi, \tag{2.5}$$

$$b_b = \int_0^{2\pi}\int_{\frac{\pi}{2}}^{\pi} \beta(\psi)\sin(\psi)d\psi d\varphi = 2\pi\int_{\frac{\pi}{2}}^{\pi} \beta(\psi)\sin(\psi)d\psi. \tag{2.6}$$

Finally, the beam attenuation coefficient c, which is the sum of the absorption and scattering coefficients, can be expressed as (Gege, 2017, p.34):

$$c = a + b = \frac{1}{\phi}\frac{d\phi_a + d\phi_b}{dz} = \frac{1}{\phi}\frac{\phi - \phi_t}{dz} \qquad \text{with } [b] = \mathrm{m}^{-1}. \tag{2.7}$$

Inherent optical properties are additive quantities, i.e., they are collectively described as the sum of the IOPs of the individual components (Pettersson and Pozdnyakov, 2013). In remote sensing, they are commonly normalized to the concentration of the compounds which they describe. For example, the Chlorophyll-*a* specific absorption coefficient of phytoplankton is defined as:

$$a^*_{ph} = \frac{1}{C_{Chla}} a_{ph} \qquad \text{with } [a^*_{ph}] = \mathrm{m}^2\mathrm{mg}^{-1}, \tag{2.8}$$

where C_{Chla} is the Chlorophyll-*a* concentration. The asterisk symbol (*) is commonly used to differentiate between IOPs and the corresponding specific inherent optical properties (sIOPs). In the context of aquatic remote sensing, mathematical models for IOPs and AOPs are called bio-optical models.

2.1.1 Water constituents and their optical characteristics

Since the composition of natural waters is highly complex, water constituents are commonly categorized in groups that share similar optical properties or that are retrieved together. The four main groups which are commonly distinguished in aquatic remote sensing applications are (Gege, 2017, p.39):

- Colored dissolved organic matter (CDOM): Filtrate of water (typically 0.2 µm pore size).
- Phytoplankton: Photosynthetic organisms with a size of about 0.2 µm to 2000 µm.
- Total suspended matter (TSM): Inorganic and organic particles.
- Detritus: Non-algal organic fraction of TSM.

A special focus of this thesis lies on the optical properties of CDOM and phytoplankton. The following section will briefly explain the motivations for their monitoring and introduce their IOP characteristics.

Colored dissolved organic matter (CDOM)

CDOM is the filtrate of a natural water sample. It comprises a vast variety of molecules and other compounds smaller than 0.2 µm. Large parts of CDOM are decomposition products of

plant tissue which are also referred to as 'humic substances' (Kirk, 2011, p.65). With the help of chemical analysis, they can be separated into the alkali-non-soluble fraction ('humins') and the soluble portion. The latter is further partitioned according to its reaction to acids. The acid-soluble fraction is called 'fulvic acids' and the precipitated fraction contains the so called 'humic acids' (Kirk, 2011, p.65). The chemical composition of CDOM can give insight into its sources and origin and differs between marine and coastal or inland aquatic environments. For example, it has been reported that fulvic acids from marine samples showed lower abundances of aromatic and phenolic compounds than samples from river streams (Malcolm, 1990).
Two major sources of CDOM are distinguished: In inland waters, the major part of CDOM is found to originate from humic substances in the catchment areas (allochthonous sources)(Kirk, 2011, p.65), so its composition may give insight into the character and utilization of this area. Moreover, water masses can be traced with the help of CDOM monitoring, especially freshwater inputs into oceanic environments [(IOCCG, 2008, pp.37-38) and references therein]. For example, CDOM originating from the Amazon River has been traced into the North Atlantic Ocean. The influence of river water on the ocean's optical properties was observed at more than 1000 km distance from the river mouth during the high flow season (Kirk, 2011; Del Vecchio and Subramaniam, 2004).
The remaining portion of CDOM is generated inside the water body and stems from degradation of organisms, excrement and from microbial activity (autochthonous source) (Pettersson and Pozdnyakov, 2013).
Depending on its concentration and origin in a water body, CDOM changes the blue to green color of a water body and can give it an appearance which is more yellow or brown. These characteristics motivated the alternate (former) expressions for CDOM such as the German word 'Gelbstoff' (Kalle, 1949) and its english translation 'yellow substance' (Kirk, 2011). In the open ocean, light absorption is dominated by phytoplankton, while in many inland and in various coastal waters, CDOM absorption is the largest contributor in the visible spectrum (Gege, 2017, p.42). In the context of phytoplankton monitoring, high CDOM concentrations can become critical since the spectral signatures of the species of interest (e.g., cyanobacteria) can be masked by the optical features of CDOM, which introduces additional uncertainty on phytoplankton identification [e.g., Cipollini and Corsini (1994)]. This is of particular importance in the context of harmful algae bloom identification and monitoring.
CDOM has long been reckoned as one of the main water quality indicators. Being the *colored* fraction of dissolved organic matter it can be measured with optical remote sensing and a long record of such studies exist (Gholizadeh et al., 2016). Dissolved organic matter affects water quality and treatment since it promotes fouling and influences the amount of disinfectants required. Further, health risks due to chlorination of CDOM rich waters have been reported

(Kutser et al. (2017) and literature cited therein).
Apart from tracing flows of water streams and assessing water quality, the relation of CDOM to dissolved organic carbon and its role in biogeochemical cycles is currently investigated in numerous studies (Asmala et al., 2012; Dutkiewicz et al., 2015; Hestir et al., 2015a; Kutser et al., 2015; Vantrepotte et al., 2015; Tranvik et al., 2009). It is well-known that oceans play a major role in global carbon cycles. Recently however, also the contribution of freshwater bodies has come into the focus of research, in order to better understand and quantify the amount, type and fate of carbon in these ecosystems (IPCC, 2013).

Absorption characteristics Monitoring of CDOM with current remote sensing techniques mainly exploits its absorption features. CDOM strongly absorbs light in the ultraviolet (UV) and in the visible short wavelength range. This absorption decreases towards larger wavelengths, mostly vanishing in the red to infrared wavelength range. Figure 2 shows a typical absorption spectrum of CDOM retrieved from lake water. The standard model for the CDOM absorption coefficient as a function of the wavelength assumes an exponential decay (Bricaud et al., 1981):

$$a_{CDOM}(\lambda) = a_{CDOM}(\lambda_0) \cdot e^{-S_{CDOM}(\lambda-\lambda_0)} \tag{2.9}$$

The absorption coefficient at a reference wavelength (e.g., $\lambda_0 = 400\,\text{nm}$ or $440\,\text{nm}$), $a_{CDOM}(\lambda_0)$, is a measure for CDOM concentration. This coefficient is typically rather small in the open ocean with absorption values at 440 nm between approximately $0\,\text{m}^{-1}$ to $0.16\,\text{m}^{-1}$, but can reach a substantial contribution to the overall absorption in certain coastal and many inland waters. There, concentration ranges of $0.004\,\text{m}^{-1}$ to $3.82\,\text{m}^{-1}$ and $0.06\,\text{m}^{-1}$ to $19.1\,\text{m}^{-1}$ are observed, respectively (Kirk, 2011, pp.74-79). For very dark lakes, concentrations at 400 nm up to $63\,\text{m}^{-1}$ have been reported (Kutser et al., 2016).
The exponent in Eq. (2.9), S_{CDOM}, is called slope parameter and its value has been found to vary with both the composition of CDOM but also the wavelength range in which it is determined (Gege, 2017; Loiselle et al., 2009; Massicotte and Markager, 2016; Sipelgas et al., 2003). This wavelength range dependency shows the shortcoming of this single exponential modelling approach. As a consequence, multi-component Gaussian models have been proposed (Gege, 2004a; Massicotte and Markager, 2016).

Scattering and fluorescence characteristics In general, two types of scattering processes need to be distinguished: elastic and inelastic scattering. Elastic scattering occurs without exchange of energy, i.e., the scattered light retains the same wavelength as the incoming light. In inelastic scattering processes such as fluorescence, energy is exchanged between the light field and the scatterer, thereby changing the scattered light's wavelength.

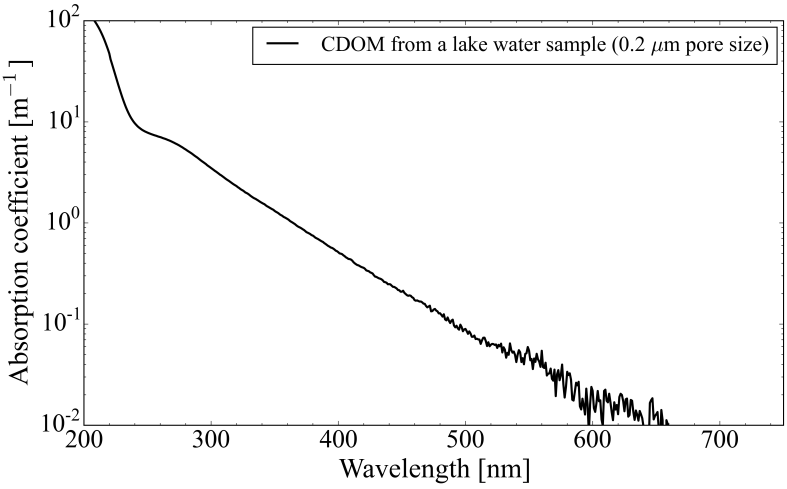

Figure 2: Typical absorption spectrum of a lake water CDOM sample (from Großer Ostersee, November 2015) measured with a double beam photometer. Plot in logarithmic scale.

Elastic scattering of CDOM can be described by Rayleigh scattering. Rayleigh scattering refers to scattering of light by particles that are much smaller than the wavelength. Its intensity is proportional to $1/\lambda^4$. Elastic scattering by CDOM is typically neglected in aquatic remote sensing due to its low contribution to the beam attenuation.

Fluorescence, in turn, as an inelastic scattering process, has been shown to provide a robust estimate of CDOM concentration in light detection and ranging (LIDAR) studies in both marine and freshwater observations [e.g., Hoge et al. (1995); Palmer et al. (2013)]. In passive remote sensing, in which the backscattered sunlight is analyzed (in contrast to active remote sensing which uses artificial light sources for the monitoring), CDOM fluorescence has been mostly neglected in the past. Nevertheless, in coastal and inland waters with higher CDOM concentrations, fluorescence can affect even passive remote sensing signals (Grassl et al., 2002). However, data such as on freshwater CDOM fluorescence for remote sensing applications is rare, and reliable models for inclusion of these trans-spectral processes into spectral radiative transfer calculations are missing. It is is one of the main targets of this thesis to fill this observational and descriptive gap.

Phytoplankton

Phytoplankton are small photosynthetic organisms which, as primary producers, form the basis of the aquatic food web. They occur in various shapes and some form groups or colonies. Depending on their cell size, phytoplankton can be categorized into classes of picoplankton (0.2 -

2 µm), nanoplankton (2 - 20 µm) and microplankton (20-200 µm) (Sieburth et al., 1978). Common genera of phytoplankton are diatoms, coccolithophores, dinoflagellates and cyanobacteria.
Despite of its small size, phytoplankton plays a fundamental role in global element cycles. Based on remote sensing observations, it was estimated that phytoplankton is responsible for about 50 % of global primary production (Longhurst et al., 1995).
Apart from their role in carbon cycling and oxygen production, some phytoplankta such as certain cyanobacteria can fix nitrogen gas (Stal, 2015). Others (e.g., dinoflagellates) produce dimethyl sulfoniopropionate (DMSP), a precursor to dimethyl sulphide (DMS) which can form sulfate aerosols when released to the atmosphere. These aerosols influence the formation of clouds (Sanchez et al., 2018) and are thus investigated in the context of ocean-atmosphere interaction studies (IOCCG, 2014; Kettle and Andreae, 2000).
Some phytoplankton can cause harmful agal blooms (HABs). As explained in Section 1.1, these HABs, caused for example by certain cyanobacteria, can threaten aquatic ecosystem either by the production of excessive biomass or by the release of toxins. Genera of freshwater cyanobacteria capable of harmful toxin production include Microcystis, Dolichospermum (formerly referred to as Anabaena), Planktothrix, as well as Cylindrospermopsis (Chorus and Bartram, 1999). Depending on the dominant genera involved, different liver toxins or neurotoxins such as anatoxins, saxitoxins, microcystins or cylindrospermopsins and even a combination of these can be released (Carmichael, 2012). High nutrient loads, increasingly stratified waters and rising temperatures, longer retention times as well as salination have been shown to promote cyanobacterial dominance (Paerl and Huisman, 2008). Some of these risk factors can be related to global climate change and human activities, thus fostering the need for a sound understanding and for monitoring capabilities of harmful algae blooms.
Remote sensing has been shown to add spatial and temporal information on cyanobacterial bloom detection (Simis et al., 2005; Kutser, 2009; Matthews et al., 2010; Kahru and Elmgren, 2014). There have been advances in mapping the cyanobacteria pigment phycocyanin using bio-optical modelling (Li and Song, 2017), and even species associated with a recurring toxic bloom have recently been targeted in algorithm development (Kudela et al., 2015). Nevertheless, data on spectral characteristics of cyanobacteria is limited and investigations on their variability are required in order to improve current detection and monitoring techniques. This is particularly important for low cyanobacteria concentrations, e.g., when they are not (yet) dominating the phytoplankton community (Li and Song, 2017).

Absorption characteristics The inherent optical properties of phytoplankton (on single cell level) are determined by its cell size and shape, pigmentation and cellular structure (Kirk,

1975a,b, 1976; Matthews, 2017).

The pigment composition shapes the spectral characteristics of the phytoplankton absorption. In eukaryotic phytoplankton (i.e., phytoplankton that possesses a membrane-enclosed nucleus), light harvesting pigments for photosynthesis are located in the thylakoid membrane in the chloroplasts (Kirk, 2011, p.265). The number of these chloroplasts per cell varies with the type of phytoplankton. In prokaryotic phytoplankton (i.e., phytoplankton without membrane-enclosed nucleus) such as cyanobacteria, the pigments can be found in the thylakoids within the cytoplasm. There are three main types of pigments: chlorophylls, carotenoids and biliproteins. While all phytoplankton have chlorophylls and carotenoids, biliproteins can be found only in rhodophyta, cyanobacteria and cryptophyta (Kirk, 2011, Chapter 8).

Since all phytoplankton contain Chlorophyll-*a*, this pigment with its distinctive spectral features serves as main indicator for phytoplankton and as a proxy for its abundance (Matthews, 2017). The two major absorption peaks of Chl-*a* are located at around 440 nm and 675 nm (cf. Fig. 3). With very low absorption in the green, this pigment is responsible for the typical green colour of phytoplankton. Pigment concentrations can be determined with the help of high pressure liquid chromatography (HPLC) or in a spectrophotometer or fluorimeter after extraction from cells (Fargion and Mueller, 2000). Concentration of Chl-*a* as observed in natural waters range from 0.01 mg m^{-3} up to 10,000 mg m^{-3} [(Matthews, 2017) and references therein]. Note that the peak positions of pigment spectra in solvent differ from those observed in the in-vivo absorption.

In addition to Chlorophyll-*a*, all phytoplankton possess carotenoids, but varying in type and composition. They serve for light harvesting as well as for protection from damage due to high fluxes in UV radiation and absorb light in a wavelength range of approximately 400 nm to 500 nm (Falkowski and Raven, 2007; Frank et al., 1986). The variation in type and composition of carotenoids amongst phytoplankton classes makes their presence a potential feature for phytoplankton differentiation. For example, β-carotenoid is present in all major phytoplankton classes except for cryptophyta. These contain alloxanthin which, in turn, is rare in other classes. In cyanobacteria, β-carotenoid is the predominant carotenoid accompanied by echinenone, zeaxanthin and myxoxanthophyll. In brown algae, diatoms and hyptophyta, fucoxanthin is the principle carotenoid (Kirk, 2011, Table 8.2).

Finally, biliproteins, which can be found in rhodophyta, cryptophyta and cyanophyta, absorb light between approximately 500 nm and 700 nm. They can be separated into phycoerythrins (PE) with an absorption around 550 nm, phycoerythrocyanins (PEC) with an absorption around 570 nm, phycocyanins (PC) with an absorption around 600 nm and allophycocyanins (APC) with an absorption around 650 nm (Zhao et al., 2012; Bryant, 1982). The latter is typically only a minor component present in rhodo- and cyanophyta, while PE tends to prevail in rhodophyta

and PC in cyanophyta (Kirk, 2011, p.294).

Pigments are not homogeneously distributed in the cell, but rather packed into units such as chloroplasts or cells. This is called 'packaging effect' and was described by Duysens (1956). It was observed that the specific absorption spectrum is flattened and lowered with increasing cell size (Kirk, 1975a,b, 1976; Bricaud et al., 1981).

Figure 3 shows an absorption spectrum of cyanobacteria grown in culture collection and a phytoplankton spectrum which was derived from the difference of total absorption and CDOM absorption of a lake water sample. Both spectra show the presence of phycobili-pigments in addition to chlorophylls and carotenoids.

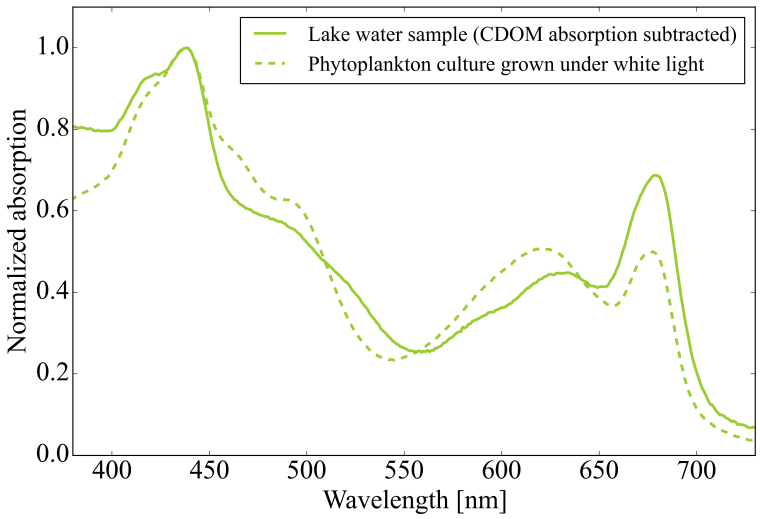

Figure 3: Normalized absorption spectrum of a phytoplankton culture in comparison with an absorption spectrum derived from a lake water sample after subtraction of CDOM absorption. The pronounced peaks around 430 nm and 675 nm correspond to Chl-*a* absorption, while spectral features between 450 nm and 500 nm can be associated with carotenoids, and those between 550 nm and 650 nm with phycobilipigments.

Scattering characteristics Scattering properties of phytoplankton are determined by its cell size, shape and refractive index. They are often approximated by Mie theory which assumes homogeneous, spherical cells and by application of the so called 'anomalous diffraction approximation' (van de Hulst, 1957) for particles with a relative refractive index close to one. Phytoplankton cells typically scatter more efficient in forward than in backward directions which results in comparably low backscattering coefficients (Mobley, 1994).

Deviations from Mie theory have been investigated by Kirk, who studied phytoplankton attenuation assuming various cell shapes and structures (Kirk, 1975a,b, 1976). MacCallum et al.

(2004) analyzed the forward scattering of three different unicellular phytoplankton species and found good agreement with Mie theory. Vaillancourt et al. (2004) measured the backscattering of twenty nine different cultures. Their results indicate an overestimation of the real value of the refractive index for these species. Zhou et al. (2012) studied the scattering and backscattering coefficients of fifteen different phytoplankton species. They found good agreement between theory and measurements for the spectral scattering spectra, but an underestimation of the backscattering coefficients at 510 nm. They suggested that large deviations for diatom and cyanobacteria originate from cell chain links and intracellular gas vacuoles. Scattering properties of cyanobacteria which can regulate their buoyancy and therefore adjust their position in the water column to optimal nutrient or light conditions (Whitton and Potts, 2007) are particularly influenced by these gas vacuoles (Dubelaar et al., 1987). Recently, a model using a two-layered sphere approach was proposed to model the impact of gas vacuoles on the IOPs of cyanobacteria *Microcystis aeruginosa* (Matthews and Bernard, 2013).
In summary, there has been success in both modelling and measurement of phytoplankton scattering, but more comprehensive data especially on freshwater phytoplankton is desirable.

Fluorescence characteristics Only a few percent of the energy of photons absorbed by phytoplankton in the ocean is re-emitted as fluorescence, while about 35 % is used in photochemistry and about 60 % is dissipated as heat [calculated from *in situ* measurements by Lin et al. (2016)]. Two important components in the photosynthetic apparatus of phytoplankton are Photosystem I (PSI) and Photosystem II (PSII) which are the light-harvesting complexes. They consist of antennas, where photons are 'harvested', and of reaction centers, to which the photons are transferred. The pigment composition of the antennae defines the photosystems' spectral characteristics and differ between PSI and PSII, as well as between species (Falkowski and Raven, 2007). For eukaryotes (i.e., with membrane-enclosed nucleus), most of this fluorescence is suspected to originate from PSII (emission around 685 nm) which contains major parts of the Chlorophyll-*a* (Matthews, 2017).
In cyanobacteria, which are procaryotes (i.e., without membrane-enclosed nucleus), major parts of the Chlorophyll-*a* are contained in PSI from which light is emitted at lower energies (Simis et al., 2012; Matthews, 2017). Additional fluorescence light is emitted via its phycobilisomes in cyanobacteria which may overlap with chlorophyll signatures as for example observed in *Microcystis aeruginosa* (Ziegmann et al., 2010).
Despite the small fluorescence efficiencies, it is possible to measure sun-induced fluorescence in reflectance measurements. Since the 1970ies there have been various studies on sun-induced Chl-*a*-fluorescence over ocean, coastal and inland waters (Neville and Gower, 1977; Fischer and Kronfeld, 1990; Babin et al., 1996; Huot et al., 2005; Gilerson et al., 2007; McKee

et al., 2007). Satellite-based sensors used in ocean color studies such as MEdium Resolution Imaging Spectrometer (MERIS), MODerate resoultion Imaging Spectrometer (MODIS) or Ocean and Land Colour Instrument (OLCI) have specific bands for detection of fluorescence of Chlorophyll-*a* (Gilerson and Huot, 2017). These are designed to cover the peak in the reflectance at around 685 nm which can be related to Chl-*a* fluorescence. An analysis of this fluorescence peak requires sensors with high sensitivity and narrow bandwidths in the relevant spectral wavelength range. Wolanin et al. (2015) reported that for hyperspectral instruments such as the SCanning Imaging Absorption SpectroMeter for Atmospheric CHartographY (SCIAMACHY), the fluorescence signal of marine phytoplankton can be retrieved from the filling-in of the solar Fraunhofer Fe I line.
Fluorescence signals can be disturbed by high particle backscattering and therefore their application to turbid and eutrophic waters remains challenging (Matthews, 2017).

2.1.2 Variability of the optical properties of phytoplankton

The variability of CDOM IOPs observed in natural water samples depends on its composition (see previous chapter), external factors such as salinity and on photochemical or microbial degradation (Osburn et al., 2014; Hernes and Benner, 2003). The situation is even more complex for phytoplankton and particularly challenging in the case of cyanobacteria. All phytoplankton are capable of adjusting their pigment content to a certain degree. For example, phytoplankton grown in cultures under low light and high nitrogen conditions typically tend to develop higher chlorophyll concentration than in natural environments (Kirk, 2011, p.279). Numerous studies have analyzed the influence of environmental factors such as irradiance, temperature and nutrient availability on the chlorophyll-to-carbon ratio [e.g., Geider (1987); Riemann et al. (1989); Kiefer and Cullen (1991)], recently even on single cell level using flow-cytometry (Álvarez et al., 2017).
As explained in the previous section, cyanobacteria possess additional light harvesting pigment-protein complexes. Being among the oldest organisms on Earth with an evolutionary history of around 3.5 billion years, they are masters in adaptation to environmental changes (Li and Song, 2017; Paerl and Paul, 2012). Some cyanobacteria are capable of so-called 'complementary chromatic adaptation'. This means they can synthesize pigment-proteins and change the phycoerythrin-phycocyanin ratio in response to the spectral composition of light they are exposed to, thus shaping their own absorption spectrum (Tandeau De Marsac, 1977). There has been considerable advance in understanding these processes on a molecular level (Grossman, 2003), but the full extent of variations in the spectral properties under natural conditions is still to be explored. This is crucial for the identification and quantification of targeted types of phytoplankton with remote sensing.

In addition to the absorption characteristics of phytoplankton, also the scattering properties are affected by the pigment variability. Furthermore, it has been shown, that the backscattering properties of phytoplankton vary over their growth phase [e.g., Moutier et al. (2017)].
Fluorescence of phytoplankton is influenced not only by the species' pigmentation but also by environmental factors such as ambient light and the physiological state of the cells. Additionally, various de-excitation paths exist [for example photo inhibitory quenching, internal state transition and energy dependent quenching (Johnsen et al., 2011)], which may reduce the fluorescence signal's intensity. It is therefore a highly complex signal which, consequently, is rich in information.
Optical properties of phytoplankton may also vary over the course of the day as observed by Poulin et al. (2018), who studied the diurnal changes in the absorption, scattering and attenuation properties of four different phytoplankton species.

In summary, the above clearly shows the relevance of and need for a detailed characterization of water constituent IOPs, their variability and triggering factors of IOP changes.

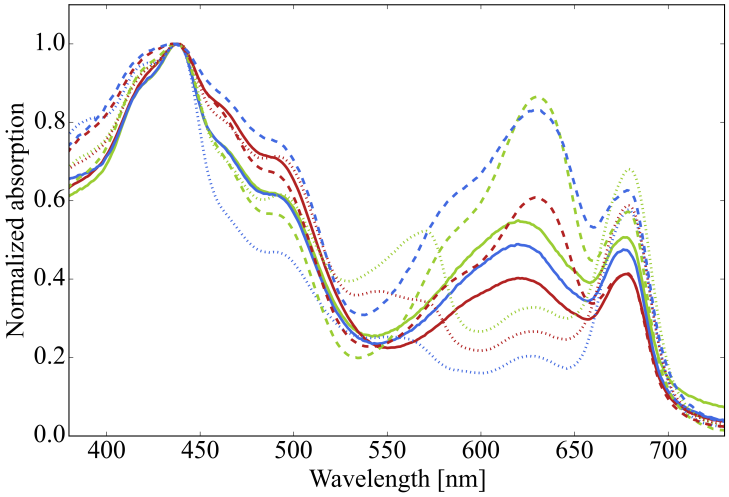

Figure 4: Variability in the normalized absorption spectra of three different phytoplankton species (*Microcystis ae.* - solid, *Synechococcus sp.* - dotted, *Limnothrix re.*- dashed) which were grown under varying light conditions (green, red and white light).

2.2 Laboratory spectroscopy: spectral IOP measurements

Spectral laboratory analysis of water constituents in the context of remote sensing serves different purposes: First, characterization of the IOPs is required for the development of accurate bio-optical models of radiative transfer in water. They further serve as basis for choice of wavelengths in band ratio algorithms and as input to other empirical or statistical approaches in remote sensing applications (IOCCG, 2014). The second purpose is to provide reference measurements in validation activities for remote sensing products. The NASA protocol for ocean color sensor validation gives an overview on methods applied for product validation (Fargion and Mueller, 2000). Spectral measurements performed in connection with this thesis mainly served the purpose of method development (see Section 3.1 and Section 3.2). Technical background information on measurement setups, procedures and data analysis can be found in the respective publications in the Appendix of this thesis.

2.2.1 Absorption and attenuation measurements

Spectral attenuation measurements of water samples are typically performed by measuring the transmission through the sample in a cuvette using a photometer. For this purpose, spectrophotometers are commonly used. With the help of a monochromator consisting of (typically adjustable) slits, a dispersive element such as a grating or prism and optics for guiding and focusing the beam, light of a broadband light source is separated into its wavelength spectrum and directed towards the sample. The spectral resolution is mainly determined by the slit width and the angular dispersion. The latter depends on the properties of the dispersive element (e.g., the line density of the grating). A reduction of the slit width increases the spectral resolution, but light intensity decreases. Therefore a compromise of signal-to-noise ratio and spectral resolution has to be made.

When a sample is positioned into the light beam, the intensity is attenuated by the sample. The transmission T[%] as a function of wavelength is determined by the ratio of the intensity of the attenuated light beam divided by the intensity of the non-attenuated beam. From this, the absorbance is calculated as the negative decadic logarithm. In the case that scattering effects can be neglected (as commonly assumed for CDOM), the attenuation gives the absorption of the samples [see Eq.(2.7)].

For determination of the absorption of a samples with non-negligible scattering, an integration sphere can be used to collected the transmitted and scattered light. The integration sphere is coated with highly reflective material serving as a Lambertian reflector. This way, the light beam inside the sphere is scattered diffusely multiple times with small intensity loss and without spectral changes before it hits the detector. Therefore, all light that is scattered or transmit-

ted into the sphere is collected by the detectors independently of its original direction.
For measurements of substances with very low concentration, as observed for CDOM in some arctic or open ocean environments, different instruments that provide very long path lengths by using long glass fibers cells as cuvettes [e.g., D'Sa et al. (1999)] or multiple reflection inside a liquid filled integrating sphere such as the point-source integrating-cavity absorption meter (PSICAM) (Röttgers and Doerffer, 2007) are available.
Absorption measurements may be affected by temperature, salinity or scattering effects (e.g., due to microbubbles). The measurement of pure water, which is required to determine the CDOM absorption, is particularly difficult due to its low absorption in the visible and potential impurification of the water. Figure 5(a) shows the absorption of pure water (stitched together from different literature values). Absorption of water strongly increases in the red to NIR. Here, different vibration modes such O-H stretching and bending and their harmonics cause spectral features typical for water (Stomp et al., 2007). Vibration of water molecules increases with temperature resulting in a temperature dependency (Röttgers et al., 2014) of their respective spectral signatures which is depicted in Fig. 5(b).

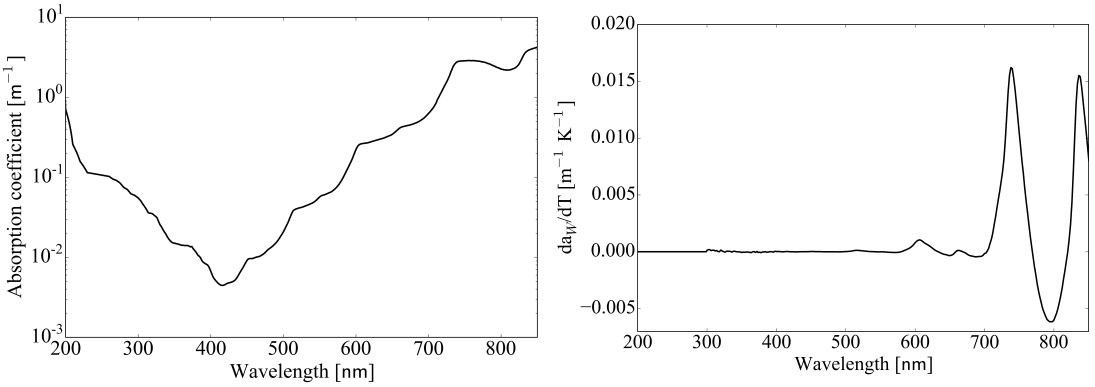

Figure 5: Spectral features of pure water: (a) the absorption coefficient (as implemented in WASI [taken from (Quickenden and Irvin, 1980; Kou et al., 1993; Pope and Fry, 1997; Lu, 2007; Wang, 2008)]. (b) Temperature gradient of pure water absorption (Röttgers et al., 2014).

2.2.2 Fluorescence measurements

Inelastic scattering of light at a molecule which leads to the emission of a photon is called photoluminescence. Depending on the electronic state from which the photons are emitted, the particular process involved is either fluorescence or phosphorescence. The latter refers to processes in which an internal (quantum mechanically forbidden) state conversion, a so called inter-system crossing, has occurred after absorption of the photons, leading to longer lifetimes

(Lakowicz, 2006). Emission without state conversion is called fluorescence. The energy lost in both processes leads to the emission at longer wavelengths of the emitted compared to the absorbed photon (Stokes shift).
For Chlorophyll-*a*, most of the fluorescence light is emitted from around 685 nm which corresponds to the lower excited electronic state. A schematic illustration of these processes and the resulting spectral absorption and emission lines can be found in (Taiz and Zeiger, 2006, p.128, Figure 7.5)]. Various vibrational and rotational states extend the energy range in which absorption and emission becomes possible leading to broadened spectral bands.
Commercial bench-top-fluorimeter are available for recording of steady-state fluorescence spectra in a tunable range. In addition to the excitation monochromator, these instruments contain a second monochromator in which the emitted light is detected as a function of the wavelength. Excitation-emission measurements or matrices (EEMs) can be acquired by selection of a range of excitation wavelengths and automatic acquisition of the corresponding emission spectra. The processing of EEMs involves several steps which are explained in detail in Section 3.2. In the context of the fluorescent part of dissolved organic matter (FDOM), EEM analysis has become very popular since EEMs provide a spectral fingerprint which can give insight into the composition of this compound and its changes, and therefore into the origin or fate of dissolved organic matter [e.g., Coble et al. (1998); Kowalczuk et al. (2005); Bieroza et al. (2009); Gonçalves-Araujo et al. (2015)]. Especially multivariate decomposition methods such as parallel factor analysis (PARAFAC) (Bro, 1997; Murphy et al., 2013, 2014) which enable spectral evaluation in a stack of EEM data, have been proven to be a useful tool for the analysis of CDOM analysis [e.g., Stedmon and Markager (2005); Yamashita et al. (2008); Singh et al. (2010); Gonçalves-Araujo et al. (2015)]. However, analytical models for the analysis and simulation of fluorescence intensities as a function of the excitation and emission wavelengths as required in bio-optical modelling are rare. Moreover, excitation-emission measurements are often performed in relative units rather than absolute numbers, so they cannot be directly integrated into radiative transfer calculations. This hurdle will be tackled in Section 3.2.

2.3 Field spectroscopy: from IOPs to remote sensing

Optical remote sensing allows monitoring of water bodies by spectral detection of the backscattered sunlight. The parameter that is typically measured in remote sensing is the reflectance. In contrast to the absorption and scattering coefficients, reflectance is an apparent optical property (AOP), i.e., it depends on the illumination conditions. Remote sensing reflectance is defined

as (Kirk, 2011, p.174):

$$R_{rs}(\lambda) = \frac{L_w(\lambda)}{E_d(\lambda)} \qquad \text{with } [R_{rs}] = \text{sr}^{-1}, \tag{2.10}$$

where $L_w(\lambda)$ is the water leaving spectral radiance in [W m^{-2} sr^{-1} nm^{-1}] and $E_d(\lambda)$ the downwelling spectral irradiance in [W m^{-2}nm^{-1}], i.e., radiance originating from the sun and the sky integrated over the upper hemisphere. The actual radiance that is detected by the sensor is the upwelling radiance L_u which is the sum of the water radiance L_w and the radiance from surface reflections L_s (Gege, 2017, p.46):

$$L_u(\lambda) = L_w(\lambda) + L_s(\lambda) \qquad \text{with } [L_u(\lambda)] = \text{W m}^{-2}\text{sr}^{-1}\text{nm}^{-1}. \tag{2.11}$$

It is therefore convenient to additionally introduce the remote sensing ratio r_{rs} as the ratio of upwelling radiance L_u to downwelling irradiance E_d.
The water leaving radiance carries the actual information on the state of the water body. The fraction of solar irradiance that enters the water body is altered by the medium it passes. The alteration of irradiance under water is described by the diffuse attenuation coefficient K_d. This parameter is determined by the optical properties of the water and commonly described with the approximation by Gordon (1989):

$$K_d(\lambda) = \kappa \cdot \frac{a(\lambda) + b_b(\lambda)}{\cos\theta_s'} \qquad \text{with } [K_d(\lambda)] = \text{m}^{-1}, \tag{2.12}$$

Where κ is a dimensionless coefficient and $\theta_s^{'}$ the in-water sun zenith angle.
For the remote sensing ratio under water as a function of the absorption and backscattering coefficients the following approximation has been derived (Gordon et al., 1975; Albert, 2005; Gege, 2017):

$$r_{rs}(\lambda) = f_{rs} \cdot \frac{b_b(\lambda)}{a(\lambda) + b_b(\lambda)} \qquad \text{with } [r_{rs}] = \text{sr}^{-1}. \tag{2.13}$$

This model was established for optically deep water (e.g. without bottom contribution), with f_{rs} being a proportionality factor. Different models have been developed for the f_{rs}-factor which itself depends on the illumination conditions. In the parametrization of Albert and Mobley (2003) and Albert (2005), which is implemented in the WASI software used for inversion in Section 3.3, f_{rs} is a function of the absorption and backscattering coefficients, the wind speed, the in-water sun zenith angle and the viewing angle in water.
For remote sensing of shallow areas, the r_{rs} can be parametrized as a function of bottom properties [e.g., Albert (2005)].
With the help of the following relation, the remote sensing reflectance can be determined from

the in-water remote sensing ratio (Mobley, 1994; Lee et al., 1998; Gege, 2017):

$$R_{rs}(\lambda) = \frac{\zeta \cdot r_{rs}(\lambda)}{1 - \Gamma \cdot r_{rs}(\lambda)} + R_{rs}^{surf}(\lambda), \tag{2.14}$$

Where ζ is the water-to-air radiance divergence factor, Γ the internal reflection factor from water to air and $R_{rs}^{surf}(\lambda)$ accounts for surface reflections. The modelling of the surface reflectance R_{rs}^{surf} will be discussed in Section 2.3.2 and a parametrization for coping with spectral surface reflection effects under variable cloud cover is presented in Section 3.3.

2.3.1 Inverse modelling using the WASI software

In the present studies, the Water Color Simulation software (WASI) which is described in Gege (2004b) and in Gege (2014b) was used for forward simulation of the in-water irradiance (see Section 3.1) and inverse analysis of both in-water irradiance and above-water remote sensing reflectance (see Section 3.3). The software allows to model spectral data in a wavelength range of 380 nm to 1000 nm depending on the spectral coverage of the data in the underlying spectral library. Building up on common analytical models for absorption, backscattering, irradiance, remote sensing reflectance and surface reflections, it enables fast analysis of aquatic remote sensing data (Albert, 2005). In the inverse mode, measurements are modeled for a set of start parameters which are then varied with the help of the Simplex algorithm. The best fit is determined by finding the set of parameters which produces the minimal residuum between the measured and the modeled spectrum (Nelder and Mead, 1965; Albert, 2005). While forward simulations serve for sensitivity studies [as for example used in (Dekker et al., 2017)], inverse modelling enables the retrieval of water constituent parameters such as CDOM absorption at 440 nm, Chl-*a* and total suspended matter (TSM) concentration, as it was done in a study related to this project (Dörnhöfer et al., 2016). Here, water constituent retrieval from recent Sentinel-2A imagery was validated using hyperspectral *in situ* measurements. Also, information on the sensor depth or, in case of shallow water, the bottom depth, as well as bottom substrates or cover types can be derived with WASI [e.g., Gege (2014a); Groetsch and Gege (2012); Albert and Gege (2006)]. Challenges lie in the tuning of the fit parameters and in spectral ambiguities. The latter can be partly circumvented by the correct choice of type and number of fit parameters or by iterative fitting as used in Chapter 3.3. The quality of the results further relies on the accuracy of the bio-optical models and spectral data used during simulation.

2.3.2 Incident solar radiation and atmospheric effects

Most part of the light detected above water originates from the sun and has interacted with the atmosphere on its way to the ground and again on its way back towards the sensor. The spectral shape of the solar irradiance at the Earth's surface is similar to the emission of a black body of about 5800 K but with narrow lines to due gas absorption in the photosphere (Fraunhofer lines), and, additionally broader bands due to atmospheric absorption. Molecules responsible for major absorption peaks in the UV and visible wavelength range are ozone, oxygen and water vapour (Kirk, 2011; Mobley, 1994).
Downwelling irradiance at the Earth's surface consists of both direct sunlight and diffuse skylight. The spectral shape of the latter is determined by the type of scattering processes involved which depend on the size of the scatterers in comparison to the incident wavelength and their shapes as well as refractive indices. Common models for downwelling irradiance such as the approach by Gregg and Carder (1990) distinguish between a component for direct sunlight and two components which represent diffuse light from Rayleigh and Mie scattering. Their parametrization of these three components is state-of the-art in aquatic remote sensing (Gege, 2017), and is used for irradiance simulations in Chapter 3.1 and for irradiance inversion Chapter 3.3.
When analyzing satellite data, accurate correction of the atmosphere between the sensor and the target is a very critical step. Due to the high absorption of water and its compounds, water leaving radiance makes up only a small fraction (20 % or less) of the radiance detected at the sensor (Moses et al., 2017; Hovis and Leung, 1977). Correction procedures derived for land and oceanic environments can often not easily be transferred and applied to optically complex water bodies: for example, aerosols may be less homogeneously distributed; altitude and therefore aerosol column height may differ and black pixel assumption may fail (Moses et al., 2017). The latter assumes vanishing reflectance from water in the near infrared wavelength range (where water strongly absorbs light). This characteristic is used for determination of aerosol influence on the signal, but in water bodies with high suspended matter or sediment loads, the assumption does not necessarily hold any more. Finally, coastal and inland waters are typically in proximity to or even enclosed by land. Light scattered by terrestrial objects may also enter the detector. The resulting spectral distortion is called adjacency effect. It is influenced mostly by the viewing geometry, illumination conditions, topography of the surrounding environment and the aerosol optical depth (Moses et al., 2017). Therefore, it is important to compare different algorithms for atmospheric correction and evaluate their applicability to inland water monitoring, as it was done in (Dörnhöfer et al., 2016), and investigate ways of improvement.
Finally, another challenge in the analysis of measurements over water are surface reflections.

These signals need to be disentangled from the actual water signal [see Eq. (2.14)]. Due to the roughness and movements of the water surface, reflections can originate from various directions and add to the specular reflection. For open-ocean environments and sensors with large pixel size, direct sunlight reflections, so-called sun glint, can be modeled as a function of wind speed, viewing geometry, illumination conditions and the slope distribution of the moving surface using a stochastic approach (Cox and Munk, 1954, 1956). With smaller pixel sizes required for inland and coastal water mapping, the statistical assumption for averaging over wave facets may break, requiring novel approaches.
A model for correction of sun glint and diffuse sky light under blue sky conditions has been described recently (Gege and Grötsch, 2016). It enables spectral correction with the help of three different components for irradiance, one for direct sun light and two for diffuse sky light. Parts of the study presented in Chapter 3.3 build up on this approach and extend it in order to model cloud effects.

2.3.3 Field sensors

A large suite of sensors exists which are commonly deployed for optical aquatic remote sensing, ranging from multispectral to hyperspectral and from radiometric to imaging instruments. In multispectral instruments, light is collected at a few selected wavelengths while hyperspectral sensors record signals with a higher number of more narrow and continuously distributed bands.
For in-water measurements, typically a combination of submersible spectroradiometers for simultaneous measurements of L_u, E_d and E_u is used. With a downward looking radiance sensor, the upwelling radiance L_u is recorded, while radiometers equipped with a cosine collector optics measure the down- and upwelling irradiances, E_d and E_u .
Above-water (near surface) measurements are commonly performed using the same set of spectrometers as for the in-water meaurements or with a hand-held spectrometric device. If the latter is equipped with a radiance optic only, the downwelling irradiance E_d can be determined with the help of a portable reflectance standard. When placed on the ground of the measurement platform (e.g., a boat or runway), the incident radiation is recorded. If the spectral reflectance of the standard is known, the downwelling irradiance can be estimated from the radiance measurement (see methods section in (Göritz et al., 2018), Appendix A.3).

The following three chapters present the research results which build up on the background presented here and which address the objectives stated in Section 1.3.1.

3 Research Results

This chapter reports on the research results which were achieved in connection with the objectives described in Section 1.3.1. Findings have been published or submitted as three full-paper peer review articles which can be found in Appendix A. These articles will be briefly recaptured in the following sections, addressing:

- The development of a novel laboratory environment (ENVILAB) for systematic studies on phytoplankton spectral absorption, scattering and fluorescence characteristics under tunable environmental conditions (publication A.1).
- The development of a novel bio-optical model (GLEAM) for the combined simulation of CDOM absorption and fluorescence characteristics based on laboratory experiments (publication A.2).
- The assessment of water constituent retrieval under variable cloud cover and the systematic study of various approaches to account for variable surface reflection (publication A.3).

3.1 Spectroscopic characterization of phytoplankton - the ENVILAB setup

The design, development and validation of a laboratory environment for systematic studies on spectral characteristics of phytoplankton has been reported in publication A.1 (Göritz et al., 2017). In the following section, the main features of this ENVILABwill be summarized and discussed in the context of their relevance for phytoplankton studies.
Figure 6 shows a schematic illustration of the assembly. The main components are:

- a tunable light source to simulate different illumination conditions,
- a photobioreactor with temperature and spectrometric growth control specifically designed for optical and mircobial studies, and
- an automated liquid transportation system which allows for sample transfer into the spectrophotometer and fluorometer as well as for nutrient control.

All components have been designed and built within the framework of this thesis.

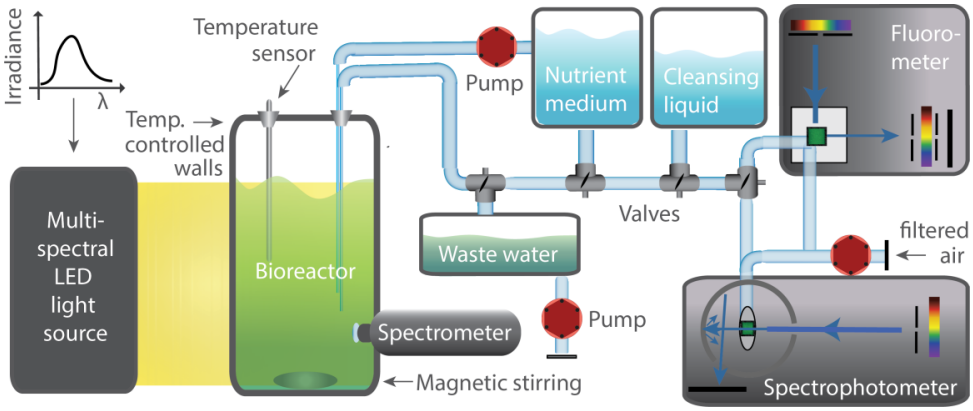

Figure 6: Schematic illustration of the ENVILAB laboratory measurement environment with tunable light source, temperature-controlled photobioreactor and automated liquid transportation and spectrometric measurement control [Reprinted with permission from (Göritz et al., 2017), OSA].

3.1.1 Tunable light source

Various phytoplankton species (in particular cyanobacteria) have been shown to adjust their pigmentation in response to intensity and spectral composition of light (see, e.g., Stramski and Morel (1990); MacColl (1998); Lutz et al. (2001); Kirk (2011) and Fig. 4 in Section 2.1.2). Thus, it is necessary to consider these illumination conditions in phytoplankton growth and experiments which serve their spectral characterization. In contrast to incandescent day light lamps and standard selected color light-emitting diode (LED) light sources or light sources which are optimized for phytoplankton growth in biofuel applications [e.g., used in Carneiro et al. (2009); Teo et al. (2014)], the tunable light source implemented in the ENVILAB enables reproducing the intensity and spectral composition of light found in aquatic environments. With the help of 72 high efficiency LEDs of 24 different peak wavelengths (bandwidths between 13 nm to 38 nm and two broadband LEDs), homogeneously diffused light in the photosynthetically active radiation range of 400 nm to 700 nm can be produced which simulates natural conditions. Furthermore, the light can be tuned in spectral composition and intensity whose maximum matches solar irradiance below the water surface (see Fig. 7). The varying bandwidths and non-uniformly distributed peak center wavelengths of the LEDs result in a spectral overlap of the emission peaks, leading to slight deviations from target spectra, especially for those of lower intensity. Nevertheless, it outperforms conventional light sources for phytoplankton studies with respect to its spectral flexibility and by avoiding distinctive peaks common in, e.g., fluorescent daylight lamps.

Light field tuning Models implemented in WASI (see Section 2.3.1) enable the simulation of in-water irradiance for varying water constituent composition, solar zenith angles and water depths. Via the control software, these spectra can be used as input spectra to the light source which permits reproduction of the irradiance by automatic tuning of the individual LEDs.
This feature becomes important when either natural light conditions or changes in the light environment as for example induced by an increase in CDOM concentration should be studied. Furthermore, it enables day and night cycles and simulation of light for different geographic zones. Diurnal changes have been shown to affect phytoplankton optical properties (Poulin et al., 2018). Furthermore, there is evidence that the transcriptional response of the Microcystin biosynthesis gene cluster in *Microcystis aeruginosa* is affected by changes in light intensity and spectral composition (Kaebernick et al., 2000). Moreover, the toxin production in *Cylindrospermopsis raciborskii* has been reported to be influenced by the illumination conditions and spectral composition of the light field (Carneiro et al., 2009). With its tunable light source and design for microbiological investigation, the ENVILAB opens the route towards further systematic studies on the link between light availability and toxicity of cyanobacteria.

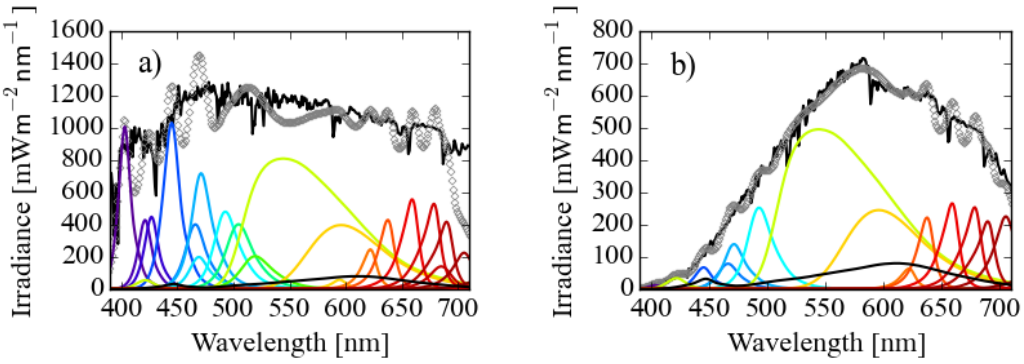

Figure 7: Comparison of desired (black solid line) and realized (grey circles) in-water downwelling irradiance spectra produced by the ENVILAB light source (a) close to the water surface, (b) at 1 m water depth.The contribution of the individual LEDs to the overall signal are illustrated by colored lines [Reprinted with permission from (Göritz et al., 2017), OSA].

3.1.2 Photobioreactor

A photobioreactor is a tank or vessel for cultivating photosynthetic microorganisms while providing controlled growth conditions. For this study, a flat panel design was chosen. The custom-built construction with two opposing borosilicate windows assures optimal coupling to the light source and enables transmission measurements with a spectrometer through the sam-

ple. This permits continuous optical depth measurements at selected wavelengths for growth phase monitoring and automated collection of spectral attenuation time series data.
Experiments with *Synechocystis sp.* (PCC 6803) demonstrated the suitability of the ENVI-LAB for phytoplankton culturing and provided insight into growth monitoring and spectral characterization capabilities. As shown in Fig. 8(a), transmission measurements through the glass windows permit continuous growth monitoring. Note that Fig. 8(a) depicts 3540 individual attenuation measurements recorded in regular time steps over six and a half days. This demonstrates the capabilities for time series studies on changes in pigment composition that are possible with the setup. Further, not only the actual change in pigment composition but also the response time of these changes induced by triggering factors can be studied.

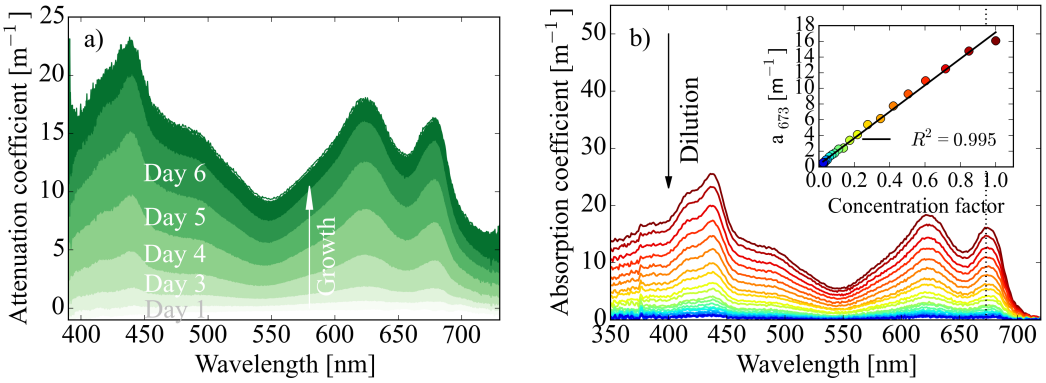

Figure 8: Growth of Synechocystis sp. (PCC 6803) monitored through the reactor windows; transmission was measured every 15 minutes in a series of 10 spectra over a period of 6.3 days leading to the depicted 3540 spectra. (b) Absorption spectra during automated dilution [Reprinted with permission from (Göritz et al., 2017), OSA].

Automated liquid transportation system and nutrient control Nutrient control is another important factor when studying the optical properties of phytoplankton since it has been shown that nutrient stress influences phytoplankton growth, physiology and its optical properties [Parkhill et al. (2001); Kiefer (1973); Stramski et al. (2002)]. Figure 8(b) shows the decrease in phytoplankton concentration when stepwise diluting with nutrient medium. Non-invasive pumping using peristaltic pumps and a cleansing cycle permit sample transportation into cuvettes in external instruments such as a double beam photometer and a fluorimeter and their extraction for microbiological and pigment analysis while keeping impurifications at a minimum. Furthermore, automated injection of nutrients is possible which allows for nutrient

availability studies and investigations at constant phytoplankton concentration.

Temperature control Temperature control is crucial since it ensures stable conditions for phytoplankton growth and spectrometric studies. At the same time, it enables investigation of temperature dependence of the optical properties and physiology. Two heat exchangers and a thermostat permit experiments in a range of about of 3°C to 39°C. Additional mixing of the culture is possible using magnetic stirring.
Increased temperatures have been reported to promote the growth of cyanobacteria (Paerl and Huisman, 2008). Furthermore, in a recent microbiological study, performed as part of the same project as the present thesis, it was found that an increase in temperature in laboratory experiments with *Microcystis aeruginosa* resulted in an upregulation of a gene related to microcystin synthesis (Scherer et al., 2016). Therefore, temperature controlled experiments are required to investigate and understand both, changes in the optical properties and toxicity of cyanobacteria.

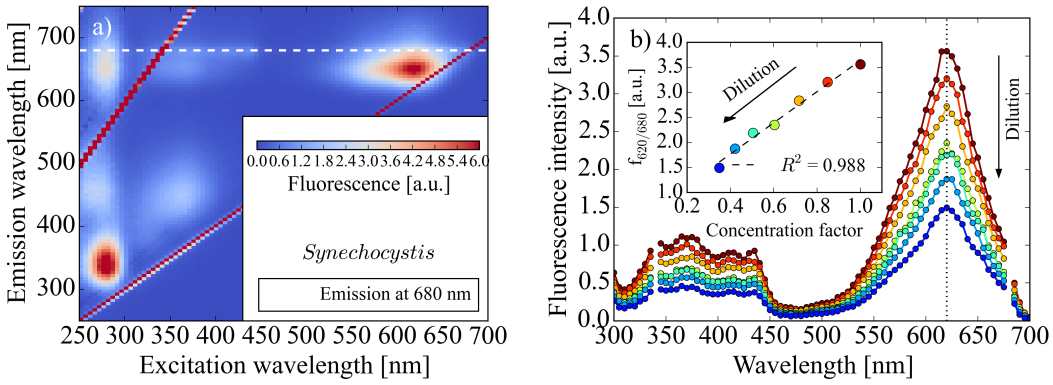

Figure 9: a) Excitation-mission spectrum of *Synechocystis sp.* (PCC6803) after blank subtraction. The dashed line indicates the excitation spectrum at 680 nm emission. (b) Excitation spectrum at 680 nm for PCC 6803 at different dilution steps. The linear decrease of fluorescence intensity at 620/680 nm excitation/emission with dilution (inset) demonstrates the proper function of the automated pumping and mixing system [Reprinted with permission from (Göritz et al., 2017), OSA].

3.1.3 Spectrometric measurements

In addition to transmission measurements through the windows of the bioreactor, absorption and fluorescence excitation-emission spectra can be recorded at user defined time steps. For

this, samples from the bioreactor are pumped by the automated transportation system to cuvettes mounted inside the respective measurement apparatus. During setup validation, spectral measurements on *Synechocystis sp.* (PCC 6803) were performed. Figure 9(b) shows the decrease in phytoplankton concentration and therefore in the absorption when diluted with nutrient medium. The peaks in the absorption spectrum can be related to cell pigments such as chlorophyll (maxima at approximately 436 nm and 673 nm) and phycocyanin (maximum at around 620 nm to 630 nm).
At the same time as the absorption measurements, fluorescence excitation-emission measurements (EEMs) were recorded. An example of such an EEM is depicted in Fig. 9(a). Again, distinct peaks are found in the spectrum due to pigment contribution. A linear decrease in the maximum at around 620 nm excitation and 680 nm emission with decreasing concentration was found as illustrated in Fig. 9(b).

In summary, the novel laboratory setup and measurement system provided by the ENVILAB provides an ideal test stage for future phytoplankton studies and will contribute to advance the understanding of phytoplankton IOP variability. Moreover, it allows the investigation of triggering factors and corresponding links to toxicity of certain species.

3.2 Modelling the absorption and fluorescence of CDOM - the GLEAM model

A spectral model for the absorption and fluorescence of colored dissolved organic matter has been developed which is reported in Appendix A.2 [Göritz and Gege (2018) - submitted for full-paper review]. This section briefly describes the development and features of this Gaussian light emission and absorption model (GLEAM), and discusses its potential for remote sensing algorithms and applications.

Colored dissolved organic matter (CDOM), as explained in Section 2.1, strongly absorbs light in the short visible wavelengths. In many inland waters, it is a major contributor to light absorption and can mask spectral features of other water constituents such as phytoplankton signatures from chlorophylls and carotenoids. It is therefore important to accurately model the spectral characteristics of CDOM when analyzing remote sensing data.

3.2.1 Absorption modelling

In remote sensing retrieval algorithms, the CDOM absorption coefficients are commonly described with an exponential function (see Section 2.1.1). It has been shown that the derived spectral slope parameter of this function varies with the wavelength range in which it is retrieved (Loiselle et al., 2009; Massicotte and Markager, 2016). Therefore, it is only valid in a limited wavelength range.
As alternative Ansatz for modelling the absorption coefficients, Gege (2000) and Schwarz et al. (2002) applied a sum of Gaussian curves to simulate the spectral behavior, which resulted in improved agreement with observed spectral features in samples from lakes and the ocean. Their approach is supported by the theory of Korshin et al. (1997), who suggested that the absorption of CDOM, which contains a mixture of organic compounds, can be approximated as superposition of molecular absorption bands of benzene with transitions located around 180 nm, 203 nm and 253 nm. Gege (2000) modeled CDOM absorption coefficients from lake and river samples with a sum of Gaussians and reported that the band center positions were located at 204.7 $\pm$1.0 nm, 233.4 $\pm$ 5.4 nm and 251.0 $\pm$ 11.4 nm. The position of two of the peaks agreed well the theory reported by Korshin et al. (1997).
Building up on these findings, the absorption coefficient spectra of lake water CDOM samples were modeled with a sum of Gaussians but with a reduction to two components in the wavelength range of 200 nm to 850 nm while considering temperature and background scattering effects. The center position of the first component was set to 203 nm [according to Gege (2000) and Korshin et al. (1997)], while the position of the second peak was fitted together with

remaining free Gaussian parameters. Figure 10 shows a comparison of a CDOM absorption coefficient spectrum with fits of the two-component Gaussian approach and the standard exponential function. Note that temperature effects were not corrected in the latter. The signatures in the UV are only captured by the sum-of-Gaussian-curves approach.

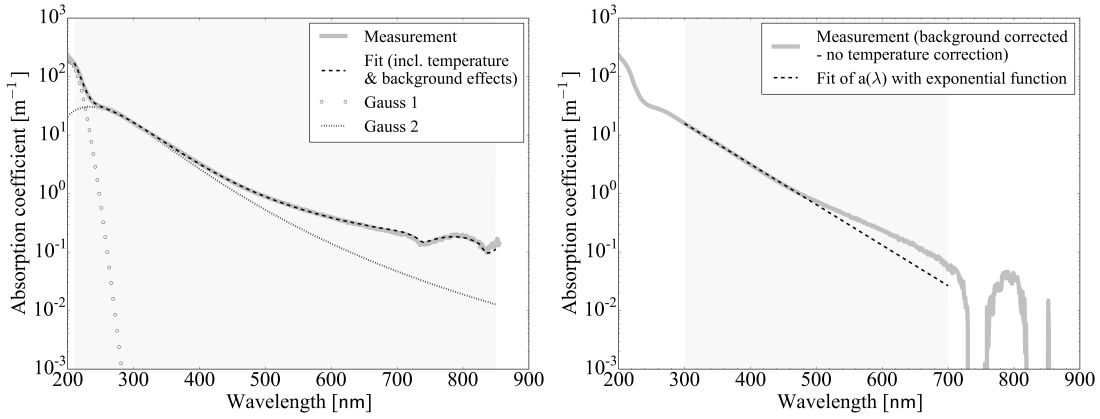

Figure 10: Comparison of measured absorption coefficient of a CDOM lake water sample modeled with (a) a sum of Gaussian curves and (b) an exponential function [Source: (Göritz and Gege, 2018)].

3.2.2 Fluorescence modelling

In addition to spectral absorption characteristics, the fluorescence signatures of CDOM were studied and an approach for modelling these characteristics was proposed. It builds up on fluorescence excitation-emission measurements (EEMs) which are described in detail in the methods section of Appendix A.2. A pre-processing of these EEMs was performed which involved the following steps:

- correction for attenuation of incident light by the sample and for re-absorption of emitted fluorescence light by the sample (inner-filter-effect),
- normalization to the Raman signal of pure water at a reference wavelength (350 nm excitation),
- masking of elastic Rayleigh scattering effects and in elastic Raman scattering of water,
- subtraction of reference spectra (pure water in the case of CDOM), and
- conversion from wavelength to wavenumber scale.

A superposition of peaks with approximately elliptical contours were observed in the processed CDOM EEM spectra. This motivated a modelling of these $f_{CDOM}(\nu_x, \nu_m)$ spectra (with ν for wavenumber and x, m for excitation and emission, respectively) using a multi-component two-dimensional Gaussian approach in the form of:

$$f_{CDOM}(\nu_x, \nu_m) = f_B + \sum_{i=1}^{n} \frac{FA_i}{2\pi\sigma_{x,i}\sigma_{m,i}\sqrt{1-\rho_i^2}} \cdot e^{-\frac{1}{2(1-\rho_i^2)} \cdot \left[\frac{(\nu_x-\nu_{xc,i})^2}{\sigma_{x,i}^2} \frac{2\rho_i(\nu_x-\nu_{xc,i})(\nu_m-\nu_{mc,i})}{\sigma_{x,i}\sigma_{m,i}} + \frac{(\nu_m-\nu_{mc,i})^2}{\sigma_{m,i}^2}\right]}. \tag{3.1}$$

Here, n denotes the number of Gaussian curves, FA_i the amplitudes, ρ_i the correlation coefficients, $\nu_{xc,i}$ and $\nu_{mc,i}$ the center frequencies for excitation and emission, and $\sigma_{x,i}, \sigma_{m,i}$ the standard deviations of the respective Gaussian curves. The term f_B represents a constant offset which accounts for potential background signals.

This approach was applied to a data set of CDOM EEMs from ten German lakes covering various CDOM concentrations. The model (with n=2) proved to be very successful in modelling the dominant spectral features which were observed in the fluorescence EEM data. An example of a modeled spectrum is depicted in Fig. 11(a). Figure 11(b) shows all modelling results for the acquired data set as a section through the EEM at 455 nm emission wavelength, which results in the depicted excitation spectra.

The center excitation wavelength ($\lambda_{xc,1}$) had to be kept fixed at an average value of 255 nm

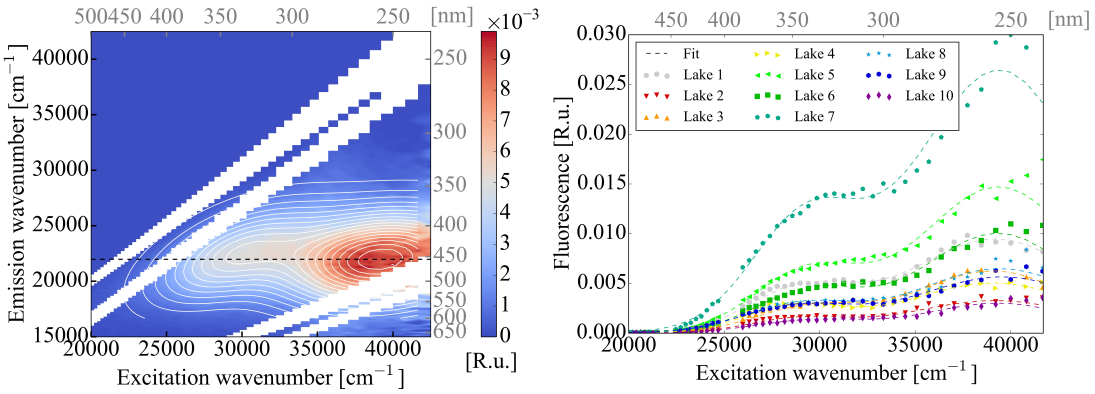

Figure 11: (a) Modeled CDOM fluorescence excitation-emission spectrum ('Lake1'). The black dashed lines denotes an emission wavelength of 455 nm. (b) Excitation spectra of CDOM samples from ten different lakes at 455 nm emission and respective fit results (dashed lines) [Source: (Göritz and Gege, 2018)].

during modelling since prior inclusion in the fit routine had resulted in very high variability. The remaining center wavelengths for the two Gaussian components which were retrieved dur-

ing modelling were found to be quite stable amongst the data: For peak #1, a $\lambda_{xc,1}$ of 461 $\pm$ 5 nm was derived. For peak #2, $\lambda_{xc,2}$ =341 $\pm$7 nm and $\lambda_{mc,2}$ = 450 $\pm$ 13 nm was determined. These center positions agreed well with position of peaks derived by statistical analysis of stacks of excitation-emission measurements as reported in the literature (Coble, 2007).
Moreover, a comparison of derived fluorescence amplitudes FA_1 and FA_2 revealed a linear relation with very high correlation between the two Gaussian components. This relation is illustrated in Fig. 12.

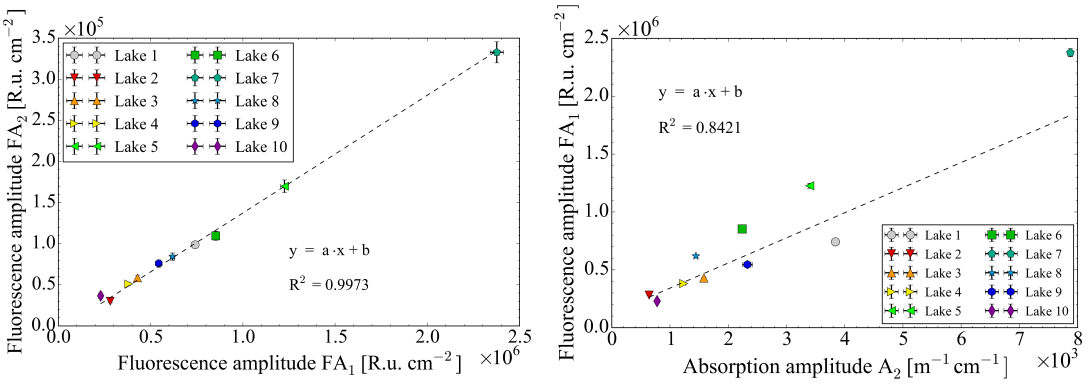

Figure 12: (a) Relation between fluorescence amplitudes retrieved with the two-component Gaussian approach (b) Relation between fluorescence amplitude #2 and absorption amplitude #1 as retrieved with Gaussian modelling of the respective spectra [Source: modified from (Göritz and Gege, 2018)].

In addition, the amplitudes of absorption peak #2 (centered around 253 nm), as retrieved from modelling the absorption coefficients, were compared against the the amplitudes of fluorescence peak #1 (centered around 255 nm excitation wavelength). Again, a correlation was observed [see Fig. 12(b)], which agrees with results of Green and Blough (1994), who found that the integrated fluorescence radiance of CDOM was proportional to the absorption coefficient at the excitation wavelength.
These two findings are important for the following reason: they suggest that a reconstruction of one of these parameters from the others is possible, and thus enable the combined modelling of CDOM absorption and fluorescence.

3.2.3 Quantum yields and spectral quantum efficiency

Integrated quantum yields $\Phi(\lambda_x)$, the ratio of emitted to absorbed photons, integrated over the emission range, were determined for the CDOM data set. For this purpose, a procedure was

followed, in which the fluorescence intensity of the sample of interest is related to the fluorescence intensity of a standard with known quantum yield (Würth et al., 2013). This procedure requires overlapping absorption and emission wavelength ranges of the sample and the reference and is therefore (with a single standard) only applicable in a limited wavelength range. In the case of the standard used in present study (quinine sulfate in perchloric acid), the quantum yield could be determined between 290 nm and 390 nm.

Wavelength dependence of quantum yields for samples from different lakes were remarkably similar but intensities varied strongly resulting in a large standard deviation as depicted Fig. 13(a). A very good agreement of the average value of $\Phi(\lambda_{350}) = 0.010 \pm 0.003$ with results reported by Hawes (1992), who studied marine CDOM samples, was found. The average quantum yield was approximated with a polynomial function of 4th order to enable an analytical modelling of the derived spectrum. Finally, a conversion factor was determined from

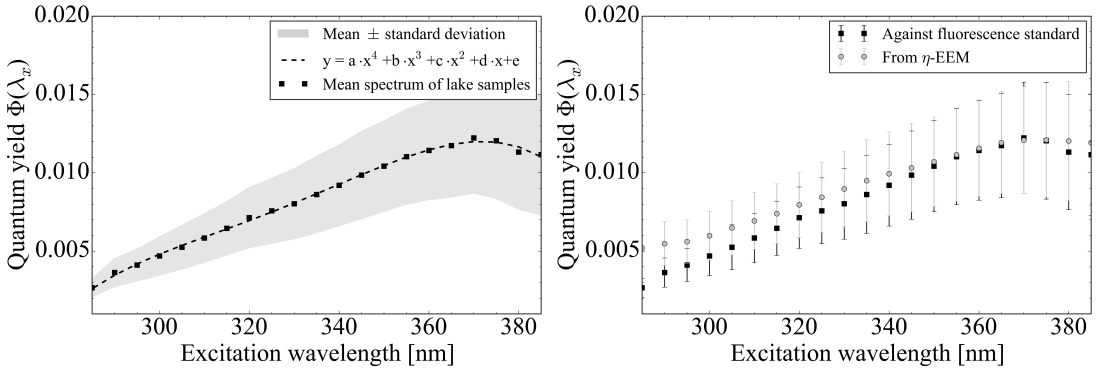

Figure 13: (a) Quantum yields of CDOM samples from different lakes. (b) Average quantum yield of CDOM samples approximated by a polynom of 4th order [Source: modified from (Göritz and Gege, 2018)].

excitation-emission measurements of the quinine sulfate standard which permitted a determination of the spectral quantum efficiencies $\eta(\lambda_x, \lambda_m)$ in the wavelength range in which EEM spectra had been measured. Integrated quantum yields were determined from this η-EEM by summing up over the emission wavelength and compared against results from the direct determination against the fluorescence standard. This is shown in Fig. 13(b) which confirms the correct conversion of the EEM data.

In a last step, the quantum efficiency spectra were modeled with a non-normalized two-dimensional two-component Gaussian curve. This model allowed to derive a parametrization for the η-EEM. Figure 14(a) gives an example of a modeled η-EEM. Corresponding excitation spectra at an emission wavelength of 480 nm are depicted in Fig. 14(b). It is important to note that findings of the present studies suggest that highest fluorescence quantum efficiencies

of CDOM are to be expected in the visible.

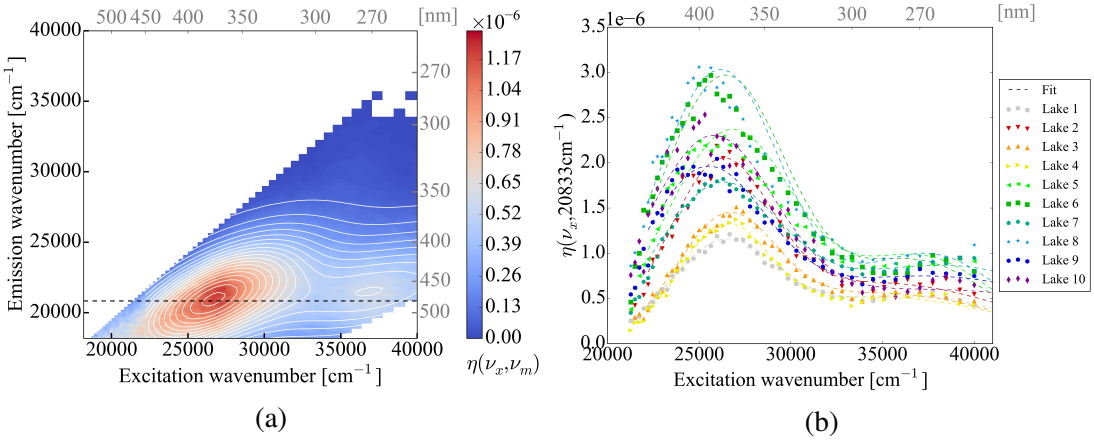

Figure 14: (a) Modeled CDOM spectral quantum efficiency (η) excitation-emission spectrum ('Lake1'). The dashed line denotes an emission wavelength of 455 nm. (b) η-excitation spectra of CDOM samples from ten different lakes at 455 nm emission and respective fit results (dashed lines) [Source: modified from (Göritz and Gege, 2018)].

In summary, a spectral Gaussian Light Emission and Absorption Model (GLEAM) was developed which enables the combined simulation of CDOM absorption and fluorescence in the UV-VIS wavelength range. Moreover, spectral quantum efficiencies of CDOM were derived and modeled. The retrieved parametrization is of high relevance for radiative-transfer simulations. Studies of Grassl et al. (2002) suggest that, despite its low quantum efficiency, fluorescence of dissolved organic matter are relevant for the in-water radiative transfer, especially in water bodies of high CDOM and low Chlorophyll-*a* and low suspended particle concentration. The findings presented here, will help to simulate and investigate the impact of CDOM fluorescence on reflectance signals over water. This is of particular interest for hyperspectral remote sensing applications.

3.3 Water constituent retrieval under mixed skies - the 4C approach

This section addresses the water constituent retrieval under variable cloud cover as reported in publication A.3 (Göritz et al., 2018). The main findings of this study will be summarized here and their relevance for future remote sensing applications will be discussed.

Views on water bodies from optical satellites are often obstructed by clouds, especially in the tropics and temperate zones, which are the cloudiest regions on Earth (NASA-ISCCP, 1996). For a continuous water monitoring with remote sensing in cloudy areas and for time series studies in which high temporal resolution is required, observation capabilities need to be extended beyond space borne approaches. However, variable cloud cover leads to high variability in the illumination conditions. These are difficult to model and challenge current remote sensing algorithms, which are typically developed for blue-sky conditions. Therefore, investigation of the applicability of standard approaches and ways for their adaption to cope with variable illumination conditions are required.

In the present study, hyperspectral in-water irradiance and above water reflectance measure-

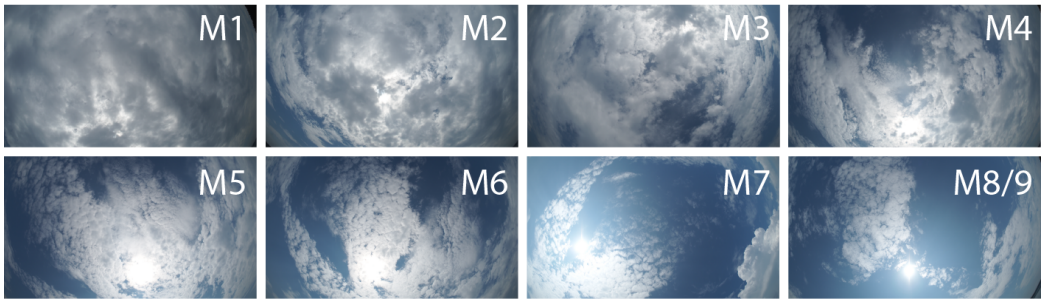

Figure 15: Variable cloud cover during acquition of sets of field measurements (M1-M9) [Source: (Göritz et al., 2018)].

ments were taken during a field campaign under changing cloud cover [see Fig. 15], and used for a feasibility study on water constituent retrieval. The *in situ* measurements were acquired at the deepest point (about 70 m depth) of Lake Stechlin in Brandenburg, North-East Germany using a great variety of sensors and retrieval procedures. The flow chart in Fig. 16 illustrates all measurements that were fed into the analysis and shows the derived parameters and inversion steps involved. For a for a detailed explanation of employed instruments and derived parameters see methods section in (Göritz et al., 2018), Appendix A.3.

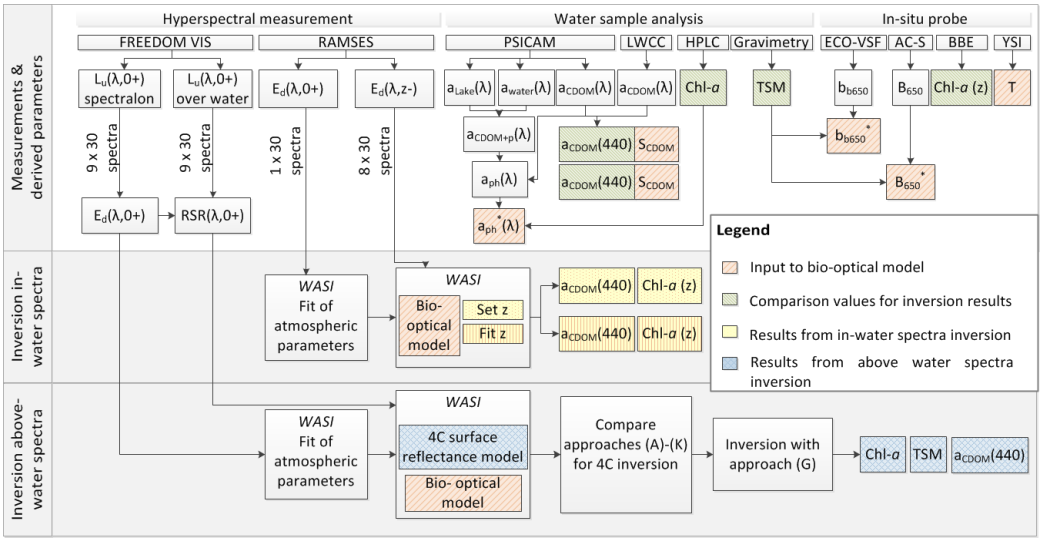

Figure 16: Flow chart of measurements and methodology employed in this study [Source: (Göritz et al., 2018)].

3.3.1 Water constituent retrieval from in-water downwelling irradiance

In the first part of this study, the water constituent retrieval from downwelling in-water irradiance (E_d) measurements with standard inversion procedures was examined. Downwelling irradiance spectra were modeled with WASI using the approach of Gege (2012a), which distinguishes between a direct and two diffuse contributions to the incident light [see Section 2.3.2 and Gregg and Carder (1990)]. Impacts of clouds were simulated as dimming of the direct and the diffuse components of this downwelling irradiance model. Estimates for a set of atmospheric parameters (the scale height of ozone, the scale height of precipitable water in the atmosphere, the Ångström exponent of aerosol scattering and the aerosol optical thickness at 550 nm) were determined by modelling irradiance spectra which were measured above water. These atmosphere parameters were then kept fixed, and in-water irradiance measurements were inverted. For this purpose, the specific absorption spectrum of phytoplankton and the specific backscattering coefficient at 650 nm as derived from separate measurements were used as input to the bio-optical model of water constituents. The first parameter was determined from the absorption coefficients of lake water and CDOM recorded in a PSICAM (Röttgers and Doerffer, 2007) and normalized to HPLC measurements of Chlorophyll-*a* concentration (Zapata et al., 2000). The specific backscattering coefficient was obtained from spectral *in situ*measurements and separate total suspended matter (TSM) analysis.

During inversion, TSM concentration was kept constant, while the Chlorophyll-*a* concentra-

tion and CDOM absorption at 440 nm were retrieved from inversion of irradiance measurements taken at different depths (see Fig. 17(a) for Chlorophyll results). An accurate retrieval was possible with a water layer of about 1.5 m above the sensor which is in accordance with findings of previous studies where a minimum layer (depending on water composition) was required, as well (Gege, 2012b; Linnemann et al., 2013). When the sensor depth was introduced as additional fit parameter to the analysis, an improved agreement between Chlorophyll-*a* concentration and CDOM absorption at 440 nm and *in situ* fluoroprobe measurements as well as water sample analysis was found [see Fig. 17(b)], suggesting the inclusion of the sensor depth as fit parameter in future retrievals.

In summary, it was shown that Chlorophyll-*a* and CDOM absorption at 440 nm below skies

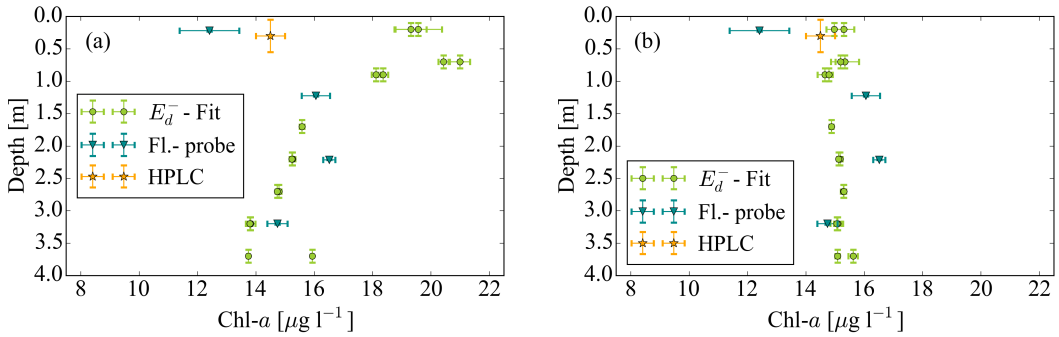

Figure 17: Comparison of Chl-*a* concentration from inversion of in-water irradiance measurements with results from a fluorescence in situ probe (a) with fixed sensor depth, (b) with varied sensor depth. Two dots at given depth represent two measured sets of 30 spectra each [Source: (Göritz et al., 2018)].

with changing cloud cover could be estimated from in-water irradiance with the help of a clear sky model with a deviation from comparison values of about 5 to 20 %. The effect of clouds was simulated by a dimming of the fraction of direct and diffuse irradiance components of the applied model. Since Chl-*a* and CDOM are important water quality parameters, their in-water retrieval may complement observation from above water in which surface reflection may complicate their mapping. Profiling these parameters adds a third dimension to their spatial mapping, which may be of special interest for modelling water constituent dynamics in time series studies as required, e.g., in order to resolve phytoplankton bloom formation and decay.

3.3.2 Water constituent retrieval from above-water radiance reflectance

In the second part of the study, water constituent retrieval from above-water radiance reflectance measurements was investigated. Here, the impact of reflections at the water surface

had to be considered. Figure 18(a) depicts the variability of the radiance reflectance spectra over water.

A recently published spectral glint model simulates surface reflections assuming three different spectral contribution to sky radiance (Gege and Grötsch, 2016; Groetsch et al., 2017). This three component surface reflection model (3C) describes the light reflected at the water surface originating from direct sunlight, from diffuse aerosol scattering and diffuse Rayleigh scattering with different spectral shapes.

As a first order approximation, cloud contribution to surface reflection was assumed to be spectrally neutral and added as a constant offset to the three component model. The resulting four component surface reflection model (4C) was then integrated into the inversion routine in WASI.

Different combinations of fit parameters were compared and the best approach in terms of spectral matching between fit and measurement curves were chosen for the water constituent retrieval. The modeled spectra for one set of measurements (30 spectra) are shown in Figure 18(b), for a certain combination of surface reflection parameters (diffuse Rayleigh scattering and cloud offset) used during inversion routine. Finally, the correction of surface reflection

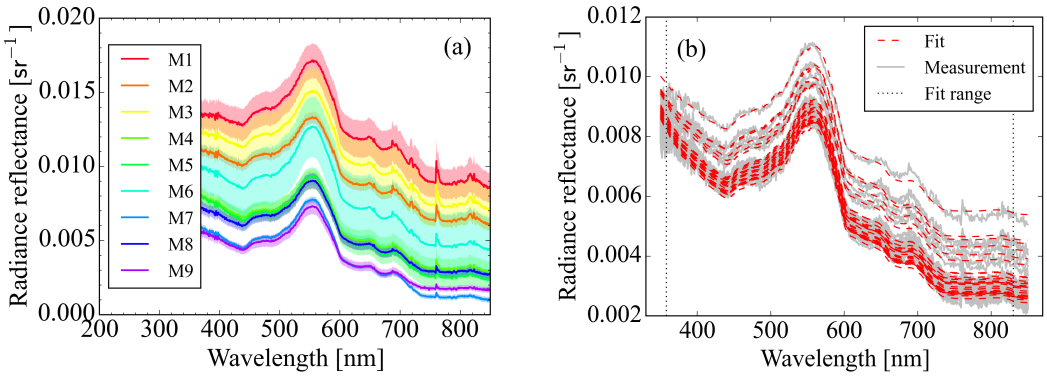

Figure 18: (a) Variability of above water radiance reflectance spectra (solid lines: mean values of measurement series, filled area: mean ± standard deviation). (b) Example of a reflectance series (M4) modeled with variable Rayleigh scattering and cloud surface reflection parameters [Source: (Göritz et al., 2018)].

effects enabled a retrieval of Chlorophyll-*a* and TSM concentration with results that deviated between 27 % and 37 % from *in situ* fluoroprobe and water sample analysis data. For CDOM, a much higher deviation of about 60% was found. Furthermore, some spurious correlation, particularly of CDOM, but also of other constituents with surface reflection parameters was observed which requires further investigation.

In a nutshell, the study revealed that a retrieval of a number of parameters from inversion of in-water irradiance spectra is possible even under highly variable illumination conditions as prevailed here. Moreover, a water constituent retrieval from highly variable radiance reflectance measurements becomes feasible when considering spectral surface reflection effects, but further investigation is required, in order to disentangle the different spectral contributions. Linking in-water and above water measurements may help to complement the retrieval of all water constituents.
In summary, the study presents promising findings with respect to future all-weather remote sensing and motivates further investigations to bridge the gaps in current satellite observations.

4 Conclusion and Outlook

4.1 Conclusion

This thesis has aimed at improving the water constituent discrimination and quantification which is required for a monitoring of water bodies and the identification of constituents such as potentially toxic cyanobacteria with optical remote sensing.
Research results presented report the advancement of water constituent retrieval in optically complex waters on three distinct but interlinked levels: Laboratory measurements and methods, modelling efforts and data retrieval techniques:

Optical remote sensing allows for a monitoring of water bodies, and ultimately relies on the analysis of spectral signatures. The better the spectral characteristics of cyanobacteria and the extend of their variability are known, the more accurate bio-optical models for their monitoring can be developed and better estimates on their reliability can be derived. Due to the high variability in the inherent optical properties (IOPs) of cyanobacteria introduced by variations in the pigment composition, the development of a spectral data basis, as direct input to algorithms or as input for model development, is not straight-forward. Reference spectra of cyanobacteria for such data bases are difficult to obtain. They may have limited representative character when obtained as a mere snapshot from cyanobacteria grown under natural conditions and, even more so, if acquired under artificial conditions. The ENVILAB whose development has been reported in this thesis, enables a systematic characterization of IOPs for tunable environmental conditions such as spectral light composition, light intensity, temperature or nutrient availability. With its link to spectrometric instruments and control software for automated measurements, it represents a versatile stage for accurate and efficient characterization of the absorption, scattering and fluorescence properties of cyanobacteria and phytoplankton in general.

When existing IOP models for the retrieval of cyanobacteria in inland waters are applied, a challenge arises in the large variations of the amount of CDOM in the water, which strongly influence the absorption in the blue wavelength range. In order to improve water constituent retrieval and to better separate the spectral influence of CDOM from targeted constituents such

as cyanobacteria, a novel spectral model for CDOM has been developed in this thesis. The Gaussian Light Emission and Absorption Model (GLEAM) enables the combined modelling of not only the absorption but also the fluorescence properties of CDOM, which have rarely been considered so far. Together with results on the spectral fluorescence quantum efficiency of CDOM presented in this thesis, a modelling of trans-spectral fluorescence processes in a broad wavelength range has become possible. Furthermore, results suggest that highest fluorescence quantum efficiencies of CDOM are to be expected in the visible wavelength range. Thus, the impact of fluorescence on remote sensing signals and its potential as additional or alternative spectral discrimination feature can now be investigated.

Even when algorithms for water constituent retrieval perform reliably, monitoring of water bodies with optical remote sensing is often limited by cloud cover. Aquatic ecosystems exhibit high dynamics (e.g., cyanobacteria blooms can occur and disappear within days or weeks). Thus, a high temporal resolution for water monitoring and a reduction of observation gaps left in satellite data is desired. Current water constituent retrieval algorithms typically presuppose clear skies. Results presented in the third part of this thesis demonstrate the potential of in-water irradiance measurements for a retrieval of absorbing compounds (such as CDOM and phytoplankton) even under variable cloud cover. Furthermore, the relevance of surface reflections under changing illumination conditions to remote sensing signals has been exemplified in field measurements. Approaches to cope with these complications have been proposed and discussed in this thesis, thereby extending existing methods for all-weather remote sensing.

4.2 Future perspectives

Based on the results presented in this thesis, the following lines of future research can be evisioned:

- **Measuring and modelling the optical properties of cyanobacteria**
  An identification of cyanobacteria, especially at low concentrations or mixed with other phytoplankton, is challenging. A sound knowledge of the inherent optical properties of common cyanobacteria helps to improve existing monitoring approaches and to reduce associated uncertainties. With the help of the ENVILAB setup, systematic studies on the absorption, scattering and fluorescence properties of cyanobacteria and their variations can be performed. Combined with pigment extraction and concentration measurements, resulting spectral data can be used for the development of a bio-optical model for remote sensing of cyanobacteria and for the enhancement of current retrieval algorithms. A reasonable selection of conditions and species should represent common types of cyanobacteria, could focus on regionally prevailing environmental conditions or ex-

plore extremes and sudden changes.

- **Phytoplankton fluorescence**
  Methods for modelling CDOM fluorescence, as developed in the GLEAM study, may be transferred to phytoplankton spectral data targeting at a fluorescence model for phytoplankton. Under consideration of spectral, radiometric and spatial resolution, the potential of planned hyperspectral missions for mapping phytoplankton fluorescence could be assessed with such a model. Upcoming missions include: The Environmental Mapping and Analysis Program (ENMAP), the DLR Earth Sensing Imaging Spectrometer (DESIS) on the International Space Station (ISS) or the FLuorescence EXplorer (FLEX) planned by European Space Agency (ESA).

- **Remote Sensing of toxic cyanobacteria**
  Targeting toxic cyanobacteria with remote sensing adds another level of complexity to the identification challenge, since not all strains that are in principle capable of toxin production are actual releasing toxins. Moreover, the species responsible for toxin release may not necessarily be the dominant phytoplankton species. This was the case in a lake that was studied during a doctoral project related to this thesis (Scherer et al., 2017). Nevertheless, certain environmental factors such as temperature have been shown to influence the toxic potential of cyanobacteria (Scherer et al., 2016). Combined studies on toxicity and IOPs would therefore be of high interest. The ENVILAB enables experiments in which spectroscopic investigations can be linked with microbial studies. Such experiments may promote the understanding of the toxicity of cyanobacteria and permit to explore links between triggering factors and changes in the IOPs.

- **CDOM composition changes**
  Colored dissolved organic matter has been shown to change its spectral absorption and fluorescence signatures when exposed to UV and sunlight (Zhang et al., 2009). Even though the ENVILAB was designed for phytoplankton studies, it may even be used to study these spectral changes of CDOM under light exposure in time series measurements. This way, one could learn more about composition changes in CDOM. The latter can be analyzed using the GLEAM model. Findings could be relevant for the understanding of biogeochemical cycles in aquatic ecosystems.

- **Sensitivity analysis on fluorescence signals with GLEAM**
  Integrating the spectral CDOM quantum efficiency matrices or the parametrization derived with GLEAM into radiative transfer calculations permits the simulation of the im-

pact of CDOM fluorescence on remote sensing signals. In the form of sensitivity studies, in which water constituent ranges are varied, the changes in the reflectance spectra due to CDOM fluorescence can be modeled and assessed. This will be of particular importance for hyperspectral remote sensing.

- **All-weather remote sensing**
  The collection of remote sensing data from airborne systems such as unmanned aerial vehicles or from buoys, ships and field measurements permits spatial observations with higher temporal resolution than from satellites. By inclusion of data recorded during cloudy days, temporal resolution can be further increased and observations would no longer be restricted to cloud-free regions. Therefore, combining UAV monitoring with retrieval models adjusted to cope with cloud cover would permit a monitoring of areas which show regular phytoplankton blooms, but in which dynamics of these blooms could not have been investigated yet due to due obstructed skies.

In summary, the contributions presented in this thesis include novel techniques, methods and findings with regards to water constituent discrimination and quantification. In the long term, they will hopefully contribute to the reduction of uncertainties in aquatic remote sensing and improve the water constituent monitoring in optically complex waters with remote sensing.
Picking up on the dictum of the Greek philosopher Anaxagoras [*"Appearances are a glimpse of the unseen."* (Kirk et al., 1983)], this thesis shall help to obtain a better vision of aquatic ecosystems with the help of remote sensing, enabling to expand our knowledge on hidden processes in this complex, dynamic and fascinating habitat of our world.

Bibliography

Albert, A. (2005). *Inversion technique for optical remote sensing in shallow water*. PhD thesis, Universität Hamburg, Hamburg, Germany.

Albert, A. and Gege, P. (2006). Inversion of irradiance and remote sensing reflectance in shallow water between 400 and 800 nm for calculations of water and bottom properties. *Appl. Opt.*, 45(10):2331–2343. https://doi.org/10.1364/AO.45.002331.

Albert, A. and Mobley, C. (2003). An analytical model for subsurface irradiance and remote sensing reflectance in deep and shallow case-2 waters. *Opt. Express*, 11(22):2873–2890. https://doi.org/10.1364/OE.11.002873.

Álvarez, E., Nogueira, E., and López-Urrutia, Á. (2017). In vivo single-cell fluorescence and size scaling of phytoplankton chlorophyll content. *Appl. Environ. Microbiol.*, 83(7). https://doi.org/10.1128/AEM.03317-16.

Asmala, E., Stedmon, C. A., and Thomas, D. N. (2012). Linking CDOM spectral absorption to dissolved organic carbon concentrations and loadings in boreal estuaries. *Estuarine Coastal Shelf Sci.*, 111(Supplement C):107 – 117. https://doi.org/10.1016/j.ecss.2012.06.015.

Babin, M., Morel, A., and Gentili, B. (1996). Remote sensing of sea surface sun-induced chlorophyll fluorescence: Consequences of natural variations in the optical characteristics of phytoplankton and the quantum yield of chlorophyll a fluorescence. *Int. J. Remote Sens.*, 17(12):2417–2448. https://doi.org/10.1080/01431169608948781.

Bieroza, M., Baker, A., and Bridgeman, J. (2009). Relating freshwater organic matter fluorescence to organic carbon removal efficiency in drinking water treatment. *Sci. Total Environ.*, 407(5):1765–1774. https://doi.org/10.1016/j.scitotenv.2008.11.013.

Bracher, A., Bouman, H. A., Brewin, R. J. W., Bricaud, A., Brotas, V., Ciotti, A. M., Clementson, L., Devred, E., Di Cicco, A., Dutkiewicz, S., et al. (2017). Obtaining phytoplankton diversity from ocean color: A scientific roadmap for future development. *Front. Mar. Sci.*, 4:55. https://doi.org/10.3389/fmars.2017.00055.

Bracher, A., Vountas, M., Dinter, T., Burrows, J., Röttgers, R., and Peeken, I. (2009). Quantitative observation of cyanobacteria and diatoms from space using PhytoDOAS on SCIAMACHY data. *Biogeosciences*, 6:751–764. https://doi.org/10.5194/bg-6-751-2009.

Bricaud, A., Morel, A., and Prieur, L. (1981). Absorption by dissolved organic matter of the sea (yellow substance) in the UV and visible domains. *Limnol. Oceanogr.*, 26(1):43–53. https://doi.org/10.4319/lo.1981.26.1.0043.

Bro, R. (1997). PARAFAC. tutorial and applications. *Chemom. Intell. Lab. Syst.*, 38(2):149–171. https://doi.org/10.1016/S0169-7439(97)00032-4.

Bryant, D. A. (1982). Phycoerythrocyanin and phycoerythrin: Properties and occurrence in cyanobacteria. *Microbiology*, 128(4):835–844. https://doi.org/10.1099/00221287-128-4-835.

Carmichael, W. W. (2012). Health effects of toxin-producing cyanobacteria: The CyanoHABs. *Hum. Ecol. Risk Assess.*, 7(5):1393–1407. https://doi.org/10.1080/20018091095087.

Carneiro, R. L., Venăncio dos Santos, M. E., Furlanetto Pacheco, A. B., and Feliciano de Oliveira e Azevedo, S. M. (2009). Effects of light intensity and light quality on growth and circadian rhythm of saxitoxins production in Cylindrospermopsis raciborskii (Cyanobacteria). *J. Plankton Res.*, 31(5):481. https://doi.org/10.1093/plankt/fbp006.

Chorus, I. and Bartram, J. (1999). (Eds.), Toxic cyanobacteria in water: A guide to their public health consequences, monitoring and management. *World Health Organization, Geneva, Switzerland, CRC Press, Taylor & Francis Group, Boca Raton, USA*.

Cipollini, P. and Corsini, G. (1994). The effect of yellow substance on pigment concentration retrieval using 'blue to green' ratio. In *OCEANS '94. Oceans engineering for today's technology and tomorrow's preservation. Proceedings*, volume 1, pages I/772–I/777. https://doi.org/10.1109/OCEANS.1994.363870.

Coble, P. G. (2007). Marine optical biogeochemistry – The chemistry of ocean color. *Chem. Rev.*, 107(2):402–418. https://doi.org/10.1021/cr050350+.

Coble, P. G., Castillo, C. E. D., and Avril, B. (1998). Distribution and optical properties of CDOM in the Arabian Sea during the 1995 Southwest Monsoon. *Deep Sea Res. Part II*, 45(10):2195 – 2223. https://doi.org/10.1016/S0967-0645(98)00068-X.

Cohen, J. E., Small, C., Mellinger, A., Gallup, J., and Sachs, J. (1997). Estimates of coastal populations. *Science*, 278(5341):1209–1213. https://doi.org/10.1126/science.278.5341.1209c.

Cox, C. and Munk, W. (1954). Measurement of the roughness of the sea surface from photographs of the sun's glitter. *J. Opt. Soc. Am.*, 44(11):838–850. https://doi.org/10.1364/JOSA.44.000838.

Cox, C. and Munk, W. (1956). Slopes of the sea surface deduced from photographs of sun glitter. *Bull. Scripps Inst. Oceanogr.*, 6(9):401–488.

Cracknell, A. P. (1999). Remote sensing techniques in estuaries and coastal zones an update. *Int. J. Remote Sens.*, 20(3):485–496. https://doi.org/10.1080/014311699213280.

Dekker, A., Pinnel, N., Gege, P., Briottet, X., Peters, S., Turpie, K., Sterckx, S., Costa, M., Giardino, C., Brando, V., et al. (2017). Feasibility study of an aquatic ecosystem earth observing system. Technical report, CEOS, CSIRO, Canberra, Australia.

Del Vecchio, R. and Subramaniam, A. (2004). Influence of the Amazon River on the surface optical properties of the western tropical north atlantic ocean. *J. Geophys. Res. Oceans*, 109(C11001). https://doi.org/10.1029/2004JC002503.

Diels, H. (1935). *(Ed.), Die Fragmente der Vorskokratiker*, volume 2. Kranz, W. Berlin.

Dierssen, H. M., Zimmerman, R. C., Leathers, R. A., Downes, T. V., and Davis, C. O. (2003). Ocean color remote sensing of seagrass and bathymetry in the Bahamas banks by high-resolution airborne imagery. *Limnol. Oceanogr.*, 48(1, part 2):444–455. https://doi.org/10.4319/lo.2003.48.1_part_2.0444.

Dörnhöfer, K., Göritz, A., Gege, P., Pflug, B., and Oppelt, N. (2016). Water constituents and water depth retrieval from sentinel-2A - A first evaluation in an oligotrophic lake. *Remote Sens.*, 8(11):941. https://doi.org/10.3390/rs8110941.

Dörnhöfer, K. and Oppelt, N. (2016). Remote sensing for lake research and monitoring - Recent advances. *Ecol. Indic.*, 64:105–122. https://doi.org/10.1016/j.ecolind.2015.12.009.

D'Sa, E. J., Steward, R. G., Vodacek, A., Blough, N. V., and Phinney, D. (1999). Determining optical absorption of colored dissolved organic matter in seawater with a liquid capillary waveguide. *Limnol. Oceanogr.*, 44(4):1142–1148. https://doi.org/10.4319/lo.1999.44.4.1142.

Dubelaar, G. B. J., Visser, J. W. M., and Donze, M. (1987). Anomalous behaviour of forward and perpendicular light scattering of a cyanobacterium owing to intracellular gas vacuoles. *Cytometry Part A*, 8(4):405–412. https://doi.org/10.1002/cyto.990080410.

Dudgeon, D., Arthington, A. H., Gessner, M. O., Kawabata, Z.-I., Knowler, D. J., Lévêque, C., Naiman, R. J., Prieur-Richard, A.-H., Soto, D., Stiassny, M. L., et al. (2006). Freshwater biodiversity: Importance, threats, status and conservation challenges. *Biol Rev*, 81(2):163–182. https://doi.org/10.1017/S1464793105006950.

Dutkiewicz, S., Hickman, A. E., Jahn, O., Gregg, W. W., Mouw, C. B., and Follows, M. J. (2015). Capturing optically important constituents and properties in a marine biogeochemical and ecosystem model. *Biogeosciences*, 12(14):4447–4481. https://doi.org/10.5194/bg-12-4447-2015.

Duysens, L. (1956). The flattering of the absorption spectrum of suspensions, as compared to that of solutions. *Biochim. Biophys. Acta*, 19:1–12. https://doi.org/10.1016/0006-3002(56)90380-8.

EOMAP (2018). EOMAP GmbH & Co.KG, Press release for launch of global water quality map on 21st of January 2018. Available online: https://www.eomap.com/launch-unesco-ihp-iiwq-world-water-quality-portal/ (accessed on 29th of June 2018).

ESA (2015). Copernicus Sentinel data (2015). Licensed under CC BY-SA 3.0 IGO. https://creativecommons.org/licenses/by-sa/3.0/igo/. retrieved from: https://www.esa.int/ESA_Multimedia/Images/2015/09/Eye_of_an_algal_storm on 30 june 2018.

Falkowski, P. G. and Raven, J. A. (2007). *Aquatic photosynthesis*. Princeton University Press, Princeton, USA, 2 edition.

Fargion, G. S. and Mueller, J. L. (2000). *Ocean optics protocols for satellite ocean color sensor validation, Revision 2*. (Eds.), National Aeronautics and Space Administration, Goddard Space Flight Center.

Fischer, J. and Kronfeld, U. (1990). Sun-stimulated chlorophyll fluorescence 1: Influence of oceanic properties. *Int. J. Remote Sens.*, 11(12):2125–2147. https://doi.org/10.1080/01431169008955166.

Frank, H. A., Chadwick, B. W., Taremi, S., Kolaczkowski, S., and Bowman, M. (1986). Singlet and triplet absorption spectra of carotenoids bound in the reaction centers of rhodopseudomonas sphaeroides r26. *FEBS Lett.*, 203(2):157–163. https://doi.org/10.1016/0014-5793(86)80734-7.

Gege, P. (1997). Classification of phytoplankton in Lake Constance by modeling the albedo. In *Ocean Optics XIII*, volume 2963, pages 423–429. International Society for Optics and Photonics. https://doi.org/10.1117/12.266478.

Gege, P. (2000). Gaussian model for yellow substance absorption spectra. *Proceedings of Ocean Optics Conference XV, 16th-20th Oct. 2000, Monaco*.

Gege, P. (2004a). Improved method for measuring Gelbstoff absorption spectra. *Proceedings of Ocean Optics Conference XVII, 25th-29th Oct. 2004, Fremantle, Australia*.

Gege, P. (2004b). The water color simulator WASI: An integrating software tool for analysis and simulation of optical in situ spectra. *Comput. Geosci.*, 30(5):523–532. https://doi.org/10.1016/j.cageo.2004.03.005.

Gege, P. (2012a). Analytic model for the direct and diffuse components of downwelling spectral irradiance in water. *Appl. Opt.*, 51(9):1407–1419. https://doi.org/10.1364/AO.51.001407.

Gege, P. (2012b). Estimation of phytoplankton concentration from downwelling irradiance measurements in water. *Isr. J. Plant Sci.*, 60(1-2):193–207.

Gege, P. (2014a). A case study at Starnberger See for hyperspectral bathymetry mapping using inverse modeling. *Proceedings of 6th WHISPERS Conference, 24th - 27th Jul. 2014, Lausanne, Switzerland*, pages 1–4. https://doi.org/10.1109/WHISPERS.2014.8077635.

Gege, P. (2014b). Wasi-2d: A software tool for regionally optimized analysis of imaging spectrometer data from deep and shallow waters. *Comput. Geosci.*, 62:208–215. https://doi.org/10.1016/j.cageo.2013.07.022.

Gege, P. (2016). Software WASI-2D. *Available online:*. http://www.ioccg.org/data/software.html (accessed on 27th of January 2016).

Gege, P. (2017). Radiative transfer theory for inland waters. In Mishra, D., Ogashawara, I., and Gitelson, A., editors, *Bio-optical modeling and remote sensing of inland waters*, chapter 2. Elsevier, Amsterdam-Oxford-Cambridge. https://doi.org/10.1016/B978-0-12-804644-9.00002-1.

Gege, P. and Grötsch, P. (2016). A spectral model for correcting sunglint and skyglint. *Proceedings of Ocean Optics Conference XXIII, 23rd-28th Oct. 2016, Victoria, Canada*, pages 1–10.

Geider, R. J. (1987). Light and temperature dependence of the carbon to Chlorophyll-a ratio in microalgae and cyanobacteria: Implications for physiology and growth of phytoplankton. *New Phytol.*, 106(1):1–34.

Gholizadeh, M. H., Melesse, A. M., and Reddi, L. (2016). A comprehensive review on water quality parameters estimation using remote sensing techniques. *Sensors*, 16(8):1298. https://doi.org/10.3390/s16081298.

Giardino, C., Bresciani, M., Stroppiana, D., Oggioni, A., and Morabito, G. (2013). Optical remote sensing of lakes: An overview on Lake Maggiore. *J. Limnol.*, 73(s1). https://doi.org/10.4081/jlimnol.2014.817.

Gilerson, A., Zhou, J., Hlaing, S., Ioannou, I., Schalles, J., Gross, B., Moshary, F., and Ahmed, S. (2007). Fluorescence component in the reflectance spectra from coastal waters. dependence on water composition. *Opt. Express*, 15(24):15702–15721. https://doi.org/10.1364/OE.15.015702.

Gilerson, A. A. and Huot, Y. (2017). *Bio-optical Modeling and Remote Sensing of Inland Waters*, chapter 7: Bio-optical Modelling of Sun-induced Chlorophyll-a Fluorescence. Elsevier (Amsterdam, Oxford, Cambridge), 1 edition.

Gonçalves-Araujo, R., Stedmon, C. A., Heim, B., Dubinenkov, I., Kraberg, A., Moiseev, D., and Bracher, A. (2015). From fresh to marine waters: Characterization and fate of dissolved organic matter in the Lena River Delta region, Siberia. *Front. Mar. Sci.*, 2:108. https://doi.org/10.3389/fmars.2015.00108.

Gordon, H. R. (1989). Can the Lambert-Beer law be applied to the diffuse attenuation coefficient of ocean water? *Limnol. Oceanogr.*, 34(8):1389–1409. https://doi.org/10.4319/lo.1989.34.8.1389.

Gordon, H. R., Brown, O. B., and Jacobs, M. M. (1975). Computed relationships between the inherent and apparent optical properties of a flat homogeneous ocean. *Appl. Opt.*, 14(2):417–427. https://doi.org/10.1364/AO.14.000417.

Göritz, A., Berger, S. A., Gege, P., Grossart, H.-P., Nejstgaard, J. C., Riedel, S., Röttgers, R., and Utschig, C. (2018). Retrieval of water constituents from hyperspectral in-situ measure-

ments under variable cloud cover—A case study at Lake Stechlin (Germany). *Remote Sens.*, 10(2):181. https://doi.org/10.3390/rs10020181.

Göritz, A. and Gege, P. (2018). GLEAM: A spectral absorption and fluorescence model for dissolved organic matter in the uv-vis. *Submitted for full-paper review*.

Göritz, A., von Hoesslin, S., Hundhausen, F., and Gege, P. (2017). ENVILAB: measuring phytoplankton in-vivo absorption and scattering properties under tunable environmental conditions. *Opt. Express*, 25(21):25267–25277. https://doi.org/10.1364/OE.25.025267.

Grassl, H., Pozdnyakov, D., Lyaskovsky, A., and Pettersson, L. (2002). Numerical modelling of transspectral processes in natural waters: Implications for remote sensing. *Int. J. Remote Sens.*, 23(8):1581–1607. https://doi.org/10.1080/014311601170735.

Green, S. A. and Blough, N. V. (1994). Optical absorption and fluorescence properties of chromophoric dissolved organic matter in natural waters. *Limnol. Oceanogr.*, 39(8):1903–1916. https://doi.org/10.4319/lo.1994.39.8.1903.

Gregg, W. W. and Carder, K. L. (1990). A simple spectral solar irradiance model for cloudless maritime atmospheres. *Limnol. Oceanogr.*, 35(8):1657–1675. https://doi.org/10.4319/lo.1990.35.8.1657.

Groetsch, P. and Gege, P. (2012). Determination of sensor depth from downwelling irradiance measurements. In *Geoscience and Remote Sensing Symposium (IGARSS), 2012 IEEE International*, pages 2860–2863. IEEE. https://doi.org/10.1109/IGARSS.2012.6350835.

Groetsch, P. M. M., Gege, P., Simis, S. G. H., Eleveld, M. A., and Peters, S. W. M. (2017). Validation of a spectral correction procedure for sun and sky reflections in above-water reflectance measurements. *Opt. Express*, 25(16):A742–A761. https://doi.org/10.1364/OE.25.00A742.

Grossman, A. R. (2003). A molecular understanding of complementary chromatic adaptation. *Photosynth. Res.*, 76(1-3):207–215. https://doi.org/10.1023/A:1024907330878.

Hawes, S. K. (1992). Quantum fluorescence efficiencies of marine fulvic and humic acids. Master's thesis, University of South Florida, USA.

Hedley, J. D., Roelfsema, C. M., Chollett, I., Harborne, A. R., Heron, S. F., Weeks, S., Skirving, W. J., Strong, A. E., Eakin, C. M., Christensen, T. R., et al. (2016). Remote sensing of coral reefs for monitoring and management: A review. *Remote Sens.*, 8(2):118. https://doi.org/10.3390/rs8020118.

Hernes, P. J. and Benner, R. (2003). Photochemical and microbial degradation of dissolved lignin phenols: Implications for the fate of terrigenous dissolved organic matter in marine environments. *J. Geophys. Res. Oceans*, 108(C9). https://doi.org/10.1029/2002JC001421.

Hestir, E. L., Brando, V., Campbell, G., Dekker, A., and Malthus, T. (2015a). The relationship between dissolved organic matter absorption and dissolved organic carbon in reservoirs along a temperate to tropical gradient. *Remote Sens. Environ.*, 156(Supplement C):395 – 402. https://doi.org/10.1016/j.rse.2014.09.022.

Hestir, E. L., Brando, V. E., Bresciani, M., Giardino, C., Matta, E., Villa, P., and Dekker, A. G. (2015b). Measuring freshwater aquatic ecosystems: The need for a hyperspectral global mapping satellite mission. *Remote Sens. Environ.*, 167:181 – 195. https://doi.org/10.1016/j.rse.2015.05.023.

Hoge, F. E., Vodacek, A., Swift, R. N., Yungel, J. K., and Blough, N. V. (1995). Inherent optical properties of the ocean: Retrieval of the absorption coefficient of chromophoric dissolved organic matter from airborne laser spectral fluorescence measurements. *Appl. Opt.*, 34(30):7032–7038. https://doi.org/10.1364/AO.34.007032.

Hovis, W. and Leung, K. (1977). Remote sensing of ocean color. *Opt. Eng.*, 16(2):162158. https://doi.org/10.1117/12.7972093.

Huot, Y., Brown, C. A., and Cullen, J. J. (2005). New algorithms for MODIS sun-induced chlorophyll fluorescence and a comparison with present data products. *Limnol. Oceanogr. Methods*, 3(2):108–130. https://doi.org/10.4319/lom.2005.3.108.

IOCCG (2000). *Remote sensing of ocean colour in coastal, and other optically-complex, waters*. Number 3 in Reports of the International Ocean Colour Coordinating Group. IOCCG, Sathyendranath, S. (Ed.), Dartmouth, Canada.

IOCCG (2008). *Why ocean colour? The societal benefits of ocean-colour technology*. Number 7 in Reports of the International Ocean Colour Coordinating Group. IOCCG, Platt, T., Hoepffner, N., Stuart, V. and Brown, C. (Eds.), Dartmouth, Canada.

IOCCG (2010). *Atmospheric correction for remotely-sensed ocean-colour products*. Number 10 in Reports of the International Ocean Colour Coordinating Group. IOCCG, Wang, M. (Ed.), Dartmouth, Canada.

IOCCG (2014). *Phytoplankton functional types from space.* Number 15 in Reports of the International Ocean Colour Coordinating Group. IOCCG , Sathyendranath, S. (Ed.), Dartmouth, Canada.

IPCC (2013). *Climate Change 2013: The Physical Science Basis. Contribution of Working Group I to the Fifth Assessment Report of the Intergovernmental Panel on Climate Change*. Cambridge University Press, Cambridge, United Kingdom and New York, NY, USA. https://doi.org/10.1017/CBO9781107415324.

Jerlov, N. G. (1976). *Marine optics*, volume 14. Elsevier Scientific Publishing Company, Amsterdam, Netherlands.

Johnsen, G., Bricaud, A., Nelson, N., Prézelin, B., and Bidigare, R. (2011). In vivo bio-optical properties of phytoplankton pigments. *Phytoplankton pigments: Characterization, chemotaxonomy and applications in oceanography*, pages 497–537.

Kaebernick, M., Neilan, B. A., Börner, T., and Dittmann, E. (2000). Light and the transcriptional response of the microcystin biosynthesis gene cluster. *Appl. Environ. Microbiol.*, 66(8):3387–3392. https://doi.org/10.1128/AEM.66.8.3387-3392.2000.

Kahru, M. and Elmgren, R. (2014). Multidecadal time series of satellite-detected accumulations of cyanobacteria in the baltic sea. *Biogeosciences*, 11(13):3619. https://doi.org/10.5194/bg-11-3619-2014.

Kalle, K. (1949). Fluoreszenz und Gelbstoff im Bottnischen und Finnischen Meerbusen. *Deutsche Hydrographische Zeitschrift*, 2:117–124. https://doi.org/doi:10.1007/BF02225972.

Kettle, A. and Andreae, M. (2000). Flux of dimethylsulfide from the oceans: A comparison of updated data sets and flux models. *J. Geophys. Res. Atmos.*, 105(D22):26793–26808. https://doi.org/10.1029/2000JD900252.

Kiefer, D. (1973). Chlorophyll a fluorescence in marine centric diatoms: Responses of chloroplasts to light and nutrient stress. *Mar. Biol.*, 23(1):39–46. https://doi.org/10.1007/BF00394110.

Kiefer, D. A. and Cullen, J. J. (1991). Phytoplankton growth and light absorption as regulated by light, temperature, and nutrients. *Polar Res*, 10(1):163–172. https://doi.org/10.3402/polar.v10i1.6735.

Kirk, G. S., Raven, J. E., Schofield, M., et al. (1983). *The presocratic philosophers: A critical history with a selcetion of texts*. Cambridge University Press, Cambridge, UKs.

Kirk, J. (1975a). A theoretical analysis of the contribution of algal cells to the attenuation of light within natural waters i. general treatment of suspensions of pigmented cells. *New Phytol.*, 75(1):11–20. https://doi.org/10.1111/j.1469-8137.1975.tb01366.x.

Kirk, J. (1975b). A theoretical analysis of the contribution of algal cells to the attenuation of light within natural waters ii. Spherical cells. *New Phytol.*, 75(1):21–36. https://doi.org/10.1111/j.1469-8137.1975.tb01367.x.

Kirk, J. (1976). A theoretical analysis of the contribution of algal cells to the attenuation of light within natural waters iii. cylindrical and spheroidal cells. *New Phytologist*, 77(1):341–358. https://doi.org/10.1111/j.1469-8137.1976.tb01524.x.

Kirk, J. T. (2011). *Light and Photosynthesis in Aquatic Ecosystems*. Cambridge University Press, Cambridge and New York, 3 edition.

Korshin, G. V., Li, C.-W., and Benjamin, M. M. (1997). Monitoring the properties of natural organic matter through UV spectroscopy: A consistent theory. *Water Res.*, 31(7):1787 – 1795. https://doi.org/10.1016/S0043-1354(97)00006-7.

Kou, L., Labrie, D., and Chylek, P. (1993). Refractive indices of water and ice in the 0.65- to 2.5-μm spectral range. *Appl. Opt.*, 32(19):3531–3540. https://doi.org/10.1364/AO.32.003531.

Kowalczuk, P., Stoń-Egiert, J., Cooper, W. J., Whitehead, R. F., and Durako, M. J. (2005). Characterization of chromophoric dissolved organic matter (CDOM) in the Baltic Sea by excitation emission matrix fluorescence spectroscopy. *Mar. Chem.*, 96(3-4):273–292. https://doi.org/10.1016/j.marchem.2005.03.002.

Kudela, R. M., Palacios, S. L., Austerberry, D. C., Accorsi, E. K., Guild, L. S., and Torres-Perez, J. (2015). Application of hyperspectral remote sensing to cyanobacterial blooms in inland waters. *Remote Sens. Environ.*, 167:196 – 205. https://doi.org/10.1016/j.rse.2015.01.025.

Kutser, T. (2009). Passive optical remote sensing of cyanobacteria and other intense phytoplankton blooms in coastal and inland waters. *Int. J. Remote Sens.*, 30(17):4401–4425. https://doi.org/10.1080/01431160802562305.

Kutser, T., Koponen, S., Kallio, K. Y., Fincke, T., and Paavel, B. (2017). Bio-optical modeling of colored dissolved organic matter. In Deepak Mishra, Igor Ogashawara, A. G., editor, *Bio-optical modeling and remote sensing of inland waters*, chapter 4, page 106. Elsevier,

Amsterdam-Oxford-Cambridge. https://doi.org/10.1016/B978-0-12-804644-9.00004-5.

Kutser, T., Paavel, B., Verpoorter, C., Ligi, M., Soomets, T., Toming, K., and Casal, G. (2016). Remote sensing of black lakes and using 810 nm reflectance peak for retrieving water quality parameters of optically complex waters. *Remote Sens.*, 8(6):497. https://doi.org/10.3390/rs8060497.

Kutser, T., Verpoorter, C., Paavel, B., and Tranvik, L. J. (2015). Estimating lake carbon fractions from remote sensing data. *Remote Sens. Environ.*, 157(Supplement C):138 – 146. https://doi.org/10.1016/j.rse.2014.05.020.

Lakowicz, J. (2006). *Principles of Fluorescence Spectroscopy*. Springer Science & Business Media, New York.

Lee, Z., Carder, K. L., Mobley, C. D., Steward, R. G., and Patch, J. S. (1998). Hyperspectral remote sensing for shallow waters. i. A semianalytical model. *Appl. Opt.*, 37(27):6329–6338. https://doi.org/10.1364/AO.37.006329.

Lesser, M. and Mobley, C. (2007). Bathymetry, water optical properties, and benthic classification of coral reefs using hyperspectral remote sensing imagery. *Coral Reefs*, 26(4):819–829. https://doi.org/10.1007/s00338-007-0271-5.

Li, L. and Song, K. (2017). Bio-optical modeling of phycocyanin. In Mishra, D. R., Ogashawara, I., and Gitelson, A. A., editors, *Bio-optical modeling and remote sensing of inland waters*, chapter 8, pages 233 – 262. Elsevier, Amsterdam-Oxford-Cambridge. https://doi.org/10.1016/B978-0-12-804644-9.00008-2.

Lillesand, T., Kiefer, R. W., and Chipman, J. (2015). *Remote sensing and image interpretation*. John Wiley & Sons, Hoboken, USA.

Lin, H., Kuzminov, F. I., Park, J., Lee, S., Falkowski, P. G., and Gorbunov, M. Y. (2016). The fate of photons absorbed by phytoplankton in the global ocean. *Science*, 351(6270):264–267. https://doi.org/10.1126/science.aab2213.

Linnemann, K., Gege, P., Rößler, S., Schneider, T., and Melzer, A. (2013). CDOM retrieval using measurements of downwelling irradiance. *Proceedings SPIE Remote Sensing, 23rd-26th of September, Dresden, Germany*. https://doi.org/10.1117/12.2031250.

Loiselle, S. A., Bracchini, L., Dattilo, A. M., Ricci, M., Tognazzi, A., Cózar, A., and Rossi, C. (2009). The optical characterization of chromophoric dissolved organic matter using

wavelength distribution of absorption spectral slopes. *Limnol. Oceanogr.*, 54(2):590–597. https://doi.org/10.4319/lo.2009.54.2.0590.

Longhurst, A., Sathyendranath, S., Platt, T., and Caverhill, C. (1995). An estimate of global primary production in the ocean from satellite radiometer data. *J. Plankton Res.*, 17(6):1245–1271. https://doi.org/10.1093/plankt/17.6.1245.

Lu, Z. (2007). *Optical absorption of pure water in the blue and ultraviolet*. PhD thesis, Texas A&M University.

Lutz, V. A., Sathyendranath, S., Head, E. J. H., and Li, W. K. W. (2001). Changes in the in vivo absorption and fluorescence excitation spectra with growth irradiance in three species of phytoplankton. *J. Plankton Res.*, 23(6):555–569. https://doi.org/10.1093/plankt/23.6.555.

MacCallum, I., Cunningham, A., and McKee, D. (2004). The measurement and modelling of light scattering by phytoplankton cells at narrow forward angles. *J. Opt. A: Pure Appl. Opt.*, 6(7):698. https://doi.org/10.1088/1464-4258/6/7/007.

MacColl, R. (1998). Cyanobacterial phycobilisomes. *J. Struct. Biol.*, 124(2):311 – 334. https://doi.org/10.1006/jsbi.1998.4062.

Malcolm, R. L. (1990). The uniqueness of humic substances in each of soil, stream and marine environments. *Anal. Chim. Acta*, 232:19 – 30. https://doi.org/10.1016/S0003-2670(00)81222-2.

Massicotte, P. and Markager, S. (2016). Using a Gaussian decomposition approach to model absorption spectra of chromophoric dissolved organic matter. *Mar. Chem.*, 180:24–32. https://doi.org/10.1016/j.marchem.2016.01.008.

Matthews, M. and Bernard, S. (2013). Using a two-layered sphere model to investigate the impact of gas vacuoles on the inherent optical properties of M. aeruginosa. *Biogeosciences*, 7:3239–3257. https://doi.org/10.5194/bg-10-8139-2013.

Matthews, M. W. (2017). Bio-optical modelling of phytoplankton chlorophyll-a. In Mishra, D., Ogashawara, I., and Gitelson, A., editors, *Bio-optical modeling and remote sensing of inland waters*, chapter 6. Elsevier, Amsterdam-Oxford-Cambridge. https://doi.org/10.1016/B978-0-12-804644-9.00006-9.

Matthews, M. W., Bernard, S., and Winter, K. (2010). Remote sensing of cyanobacteria-dominant algal blooms and water quality parameters in Zeekoevlei, a small hypertrophic

lake, using MERIS. *Remote Sens. Environ.*, 114(9):2070 – 2087. https://doi.org/10.1016/j.rse.2010.04.013.

McKee, D., Cunningham, A., Wright, D., and Hay, L. (2007). Potential impacts of nonalgal materials on water-leaving sun induced chlorophyll fluorescence signals in coastal waters. *Appl. Opt.*, 46(31):7720–7729. https://doi.org/10.1364/AO.46.007720.

Mobley, C. D. (1994). *Light and water: Radiative transfer in natural waters*. Academic Press, San Diego, USA.

Moses, W. J., Sterckx, S., Montes, M. J., De Keukelaere, L., and Knaeps, E. (2017). Atmospheric correction for inland waters. In Mishra, D. R., Ogashawara, I., and Gitelson, A. A., editors, *Bio-optical modeling and remote sensing of inland waters*, chapter 3, pages 69–100. Elsevier, Amsterdam-Oxford-Cambridge. https://doi.org/10.1016/B978-0-12-804644-9.00003-3.

Moss, B. (2012). Cogs in the endless machine: Lakes, climate change and nutrient cycles: A review. *Sci. Total Environ.*, 434:130 – 142. https://doi.org/10.1016/j.scitotenv.2011.07.069.

Moutier, W., Duforêt-Gaurier, L., Thyssen, M., Loisel, H., Mériaux, X., Courcot, L., Dessailly, D., Rêve, A.-H., Grégori, G., Alvain, S., Barani, A., Brutier, L., and Dugenne, M. (2017). Evolution of the scattering properties of phytoplankton cells from flow cytometry measurements. *PLOS ONE*, 12(7):1–24. https://doi.org/10.1371/journal.pone.0181180.

Muller-Karger, F. E., Hestir, E., Ade, C., Turpie, K., Roberts, D. A., Siegel, D., Miller, R. J., Humm, D., Izenberg, N., Keller, M., et al. (2018). Satellite sensor requirements for monitoring essential biodiversity variables of coastal ecosystems. *Ecol. Appl.*, 28(3):749–760. https://doi.org/10.1002/eap.1682.

Murphy, K. R., Bro, R., and Stedmon, C. A. (2014). Chemometric analysis of organic matter fluorescence. In *Aquatic organic matter fluorescence*, chapter 10, pages 339–375. Cambridge University Press New York, NY.

Murphy, K. R., Stedmon, C. A., Graeber, D., and Bro, R. (2013). Fluorescence spectroscopy and multi-way techniques. PARAFAC. *Anal. Methods*, 5(23):6557–6566. https://doi.org/10.1039/C3AY41160E.

NASA-ISCCP (1996). Science briefs–cloud climatology–global distribution and character of clouds. *National Aeronautics and Space Administration, Goddard Institute for Space Studies*. https://www.giss.nasa.gov/research/briefs/rossow_01/distrib.html.

Nelder, J. A. and Mead, R. (1965). A simplex method for function minimization. *Comput. J.*, 7(4):308–313. https://doi.org/10.1093/comjnl/7.4.308.

Neville, R. and Gower, J. (1977). Passive remote sensing of phytoplankton via chlorophyll a fluorescence. *J. Geophys. Res.*, 82(24):3487–3493. https://doi.org/10.1029/JC082i024p03487.

Ocean Optics Webbook (2018). Ocean optics webbook by Curtis Mobley, Emmanuel Boss, Collin Roesler. Available online: http://www.oceanopticsbook.info/view/introduction/overview (last time accessed on 18th of may 2018).

O'Reilly, C. M., Sharma, S., Gray, D. K., Hampton, S. E., Read, J. S., Rowley, R. J., Schneider, P., Lenters, J. D., McIntyre, P. B., Kraemer, B. M., et al. (2015). Rapid and highly variable warming of lake surface waters around the globe. *Geophys. Res. Lett.*, 42(24):10,773–10,781. https://doi.org/10.1002/2015GL066235.

Osburn, C. L., Del Vecchio, R., and Boyd, T. J. (2014). Physicochemical effects on dissolved organic matter fluorescence in natural waters. In *Aquatic organic matter fluorescence*, chapter 7, pages 233–277. Cambridge University Press New York, NY.

Paerl, H. W. and Huisman, J. (2008). Blooms like it hot. *Science*, 320(5872):57–58. https://doi.org/10.1126/science.1155398.

Paerl, H. W. and Otten, T. G. (2013). Harmful cyanobacterial blooms: Causes, consequences, and controls. *Microb. Ecol.*, 65(4):995–1010. https://doi.org/10.1007/s00248-012-0159-y.

Paerl, H. W. and Paul, V. J. (2012). Climate change: Links to global expansion of harmful cyanobacteria. *Water Res.*, 46(5):1349–1363. https://doi.org/10.1016/j.watres.2011.08.002.

Palmer, S. C., Kutser, T., and Hunter, P. D. (2015). Remote sensing of inland waters: Challenges, progress and future directions. *Remote Sens. Environ.*, 157:1 – 8. https://doi.org/10.1016/j.rse.2014.09.021.

Palmer, S. C., Pelevin, V. V., Goncharenko, I., Kovács, A. W., Zlinszky, A., Présing, M., Horváth, H., Nicolás-Perea, V., Balzter, H., and Tóth, V. R. (2013). Ultraviolet fluorescence LiDAR (UFL) as a measurement tool for water quality parameters in turbid lake conditions. *Remote Sens.*, 5(9):4405–4422. https://doi.org/10.3390/rs5094405.

Parkhill, J.-P., Maillet, G., and Cullen, J. J. (2001). Fluorescence-based maximal quantum yield for PSII as a diagnostic of nutrient stress. *J. Phycol.*, 37(4):517–529. https://doi.org/10.1046/j.1529-8817.2001.037004517.x.

Pettersson, L. H. and Pozdnyakov, D. (2013). *Monitoring of harmful algal bloom*. Springer-Verlag Berlin Heidelberg. https://doi.org/10.1007/978-3-540-68209-7.

Poff, N. L., Brown, C. M., Grantham, T. E., Matthews, J. H., Palmer, M. A., Spence, C. M., Wilby, R. L., Haasnoot, M., Mendoza, G. F., Dominique, K. C., et al. (2016). Sustainable water management under future uncertainty with eco-engineering decision scaling. *Nature Clim. Change*, 6(1):25. https://doi.org/10.1038/nclimate2765.

Pope, R. M. and Fry, E. S. (1997). Absorption spectrum (380–700 nm) of pure water. ii. Integrating cavity measurements. *Appl. Opt.*, 36(33):8710–8723. https://doi.org/10.1364/AO.36.008710.

Poulin, C., Antoine, D., and Huot, Y. (2018). Diurnal variations of the optical properties of phytoplankton in a laboratory experiment and their implication for using inherent optical properties to measure biomass. *Opt. Express*, 26(2):711–729. https://doi.org/10.1364/OE.26.000711.

Preisendorfer, R. (1976). Hydrologic optics. volume 1. introduction. Technical report, Honolulu: US Dept. of Commerce, National Oceanic and Atmospheric Administration, Environmental Research Laboratories, Pacific Marine Environmental Laboratory.

Quickenden, T. and Irvin, J. (1980). The ultraviolet absorption spectrum of liquid water. *J. Chem. Phys.*, 72(8):4416–4428. https://doi.org/10.1063/1.439733.

Riemann, B., Simonsen, P., and Stensgaard, L. (1989). The carbon and chlorophyll content of phytoplankton from various nutrient regimes. *J. Plankton Res.*, 11(5):1037–1045. https://doi.org/10.1093/plankt/11.5.1037.

Röttgers, R. and Doerffer, R. (2007). Measurements of optical absorption by chromophoric dissolved organic matter using a point-source integrating-cavity absorption meter. *Limnol. Oceanogr. Methods*, 5(5):126–135. https://doi.org/10.4319/lom.2007.5.126.

Röttgers, R., McKee, D., and Utschig, C. (2014). Temperature and salinity correction coefficients for light absorption by water in the visible to infrared spectral region. *Opt. Express*, 22(21):25093–25108. https://doi.org/10.1364/OE.22.025093.

Russi, D. Pantzar, M., Kettunen, M., Gitti, G., Mutafoglu, K., Kotulak, M., and ten Brink, P. (2016). Socio-economic benefits of the EU marine protected areas. *Report prepared by the Institute for European Environmental Policy (IEEP) for DG Environment, Institute for European Environmental Policy, London*.

Sanchez, K. J., Chen, C.-L., Russell, L. M., Betha, R., Liu, J., Price, D. J., Massoli, P., Ziemba, L. D., Crosbie, E. C., Moore, R. H., et al. (2018). Substantial seasonal contribution of observed biogenic sulfate particles to cloud condensation nuclei. *Sci. Rep.*, 8(1):3235. https://doi.org/10.1038/s41598-018-21590-9.

Scherer, P. I., Millard, A. D., Miller, A., Schoen, R., Raeder, U., Geist, J., and Zwirglmaier, K. (2017). Temporal dynamics of the microbial community composition with a focus on toxic cyanobacteria and toxin presence during harmful algal blooms in two South German lakes. *Front. Microbiol.*, 8:2387. https://doi.org/10.3389/fmicb.2017.02387.

Scherer, P. I., Raeder, U., Geist, J., and Zwirglmaier, K. (2016). Influence of temperature, mixing, and addition of microcystin-LR on microcystin gene expression in Microcystis aeruginosa. *MicrobiologyOpen*, 6(1). https://doi.org/10.1002/mbo3.393.

Schwarz, J. N., Kowalczuk, P., Kaczmarek, S., Cota, G. F., Mitchell, B. G., Kahru, M., Chavez, F. P., Cunningham, A., McKee, D., Gege, P., et al. (2002). Two models for absorption by coloured dissolved organic matter (CDOM). *Oceanologia*, 44(2).

Sieburth, J. M., Smetacek, V., and Lenz, J. (1978). Pelagic ecosystem structure: Heterotrophic compartments of the plankton and their relationship to plankton size fractions. *Limnol. Oceanogr.*, 23(6):1256–1263. https://doi.org/10.4319/lo.1978.23.6.1256.

Simis, S. G. H., Huot, Y., Babin, M., Seppälä, J., and Metsamaa, L. (2012). Optimization of variable fluorescence measurements of phytoplankton communities with cyanobacteria. *Photosynth. Res.*, 112(1):13–30. https://doi.org/10.1007/s11120-012-9729-6.

Simis, S. G. H., Peters, S. W. M., and Gons, H. J. (2005). Remote sensing of the cyanobacterial pigment phycocyanin in turbid inland water. *Limnol. Oceanogr.*, 50(1):237–245. https://doi.org/10.4319/lo.2005.50.1.0237.

Singh, S., D'Sa, E. J., and Swenson, E. M. (2010). Chromophoric dissolved organic matter (CDOM) variability in Barataria basin using excitation–emission matrix (EEM) fluorescence and parallel factor analysis (PARAFAC). *Sci. Total Environ.*, 408(16):3211–3222. https://doi.org/10.1016/j.scitotenv.2010.03.044.

Sipelgas, L., Arst, H., Kallio, K., Erm, A., Oja, P., and Soomere, T. (2003). Optical properties of dissolved organic matter in Finnish and Estonian lakes. *Hydrol. Res.*, 34(4):361–386. https://doi.org/10.2166/nh.2003.0012.

Stal, L. J. (2015). *Nitrogen fixation in cyanobacteria*, pages 1–9. John Wiley & Sons, Ltd., Chichester. https://doi.org/10.1002/9780470015902.a0021159.pub2.

Stedmon, C. A. and Markager, S. (2005). Tracing the production and degradation of autochthonous fractions of dissolved organic matter by fluorescence analysis. *Limnol. Oceanogr.*, 50(5):1415–1426. https://doi.org/10.4319/lo.2005.50.5.1415.

Stomp, M., Huisman, J., De Jongh, F., Veraart, A. J., Gerla, D., Rijkeboer, M., Ibelings, B. W., Wollenzien, U. I., and Stal, L. J. (2004). Adaptive divergence in pigment composition promotes phytoplankton biodiversity. *Nature*, 432(7013):104–107. https://doi.org/10.1038/nature03044.

Stomp, M., Huisman, J., Vörös, L., Pick, F. R., Laamanen, M., Haverkamp, T., and Stal, L. J. (2007). Colourful coexistence of red and green picocyanobacteria in lakes and seas. *Ecol. Lett.*, 10(4):290–298. https://doi.org/10.1111/j.1461-0248.2007.01026.x.

Stramski, D. and Morel, A. (1990). Optical properties of photosynthetic picoplankton in different physiological states as affected by growth irradiance. *Deep Sea Res. Part I Oceanogr. Res. Pap.*, 37(2):245–266. https://doi.org/10.1016/0198-0149(90)90126-G.

Stramski, D., Sciandra, A., and Claustre, H. (2002). Effects of temperature, nitrogen, and light limitation on the optical properties of the marine diatom Thalassiosira pseudonana. *Limnol. Oceanogr.*, 47(2):392–403. https://doi.org/10.4319/lo.2002.47.2.0392.

Taiz, L. and Zeiger, E. (2006). Plant physiology. 4th edition. *Sinauer Associate, Sunderland, MA*.

Tandeau De Marsac, N. (1977). Occurrence and nature of chromatic adaptation in cyanobacteria. *J. Bacteriol.*, 130(1):82–91. https://doi.org/10.1128/jb.130.1.82-91.1977.

Teo, C. L., Atta, M., Bukhari, A., Taisir, M., Yusuf, A. M., and Idris, A. (2014). Enhancing growth and lipid production of marine microalgae for biodiesel production via the use of different LED wavelengths. *Bioresour. Technol.*, 162:38 – 44. https://doi.org/10.1016/j.biortech.2014.03.113.

Tranvik, L. J., Downing, J. A., Cotner, J. B., Loiselle, S. A., Striegl, R. G., Ballatore, T. J., Dillon, P., Finlay, K., Fortino, K., Knoll, L. B., et al. (2009). Lakes and reservoirs as

regulators of carbon cycling and climate. *Limnol. Oceanogr.*, 54(6, part 2):2298–2314. https://doi.org/10.4319/lo.2009.54.6_part_2.2298.

Turak, E., Dudgeon, D., Harrison, I. J., Freyhof, J., De Wever, A., Revenga, C., Garcia-Moreno, J., Abell, R., Culp, J. M., Lento, J., et al. (2017). Observations of inland water biodiversity: Progress, needs and priorities. In *The GEO handbook on biodiversity observation networks*, pages 165–186. Springer, Cham. https://doi.org/10.1007/978-3-319-27288-7_7.

Turpie, K. (2015). New need to understand changing coastal and inland aquatic ecosystem services. *Decadal Survey for Earth Science and Applications from Space*. https://hyspiri.jpl.nasa.gov/nrc-decadal-survey (accessed on 29th of June 2018).

Turpie, K., Ackleson, S., Bell, T., Dierssen, H., Goodman, J., Green, R., Guild, L., Hochberg, E., Klemas, V. V., Lavender, S., et al. (2017). Spectroscopy for global observation of coastal and inland aquatic habitats. In *Geoscience and Remote Sensing Symposium (IGARSS), 2017 IEEE International*, pages 3051–3054. IEEE. https://doi.org/10.1109/IGARSS.2017.8127642.

UNEP (2012). Global Environmental Outlook (GEO-5). *United Nations Environment Programme -Tech. Rep., Progress Press Ltd., Malta*.

UNESCO (2018). World Water Quality Portal by the International Initiative of Water Quality IIWQ; UNESCO-IHP International Hydrological Programme. Available online: http://www.worldwaterquality.org/ (accessed on 29th of june 2016).

Vaillancourt, R. D., Brown, C. W., Guillard, R. R. L., and Balch, W. M. (2004). Light backscattering properties of marine phytoplankton: relationships to cell size, chemical composition and taxonomy. *J. Plankton Res.*, 26(2):191–212. https://doi.org/10.1093/plankt/fbh012.

van de Hulst, H. C. (1957). *Light scattering by small particles*. John Wiley & Sons, New York.

Vantrepotte, V., Danhiez, F.-P., Loisel, H., Ouillon, S., Mériaux, X., Cauvin, A., and Dessailly, D. (2015). CDOM-DOC relationship in contrasted coastal waters: Implication for doc retrieval from ocean color remote sensing observation. *Opt. Express*, 23(1):33–54. https://doi.org/10.1364/OE.23.000033.

Verpoorter, C., Kutser, T., Seekell, D. A., and Tranvik, L. J. (2014). A global inventory of lakes based on high-resolution satellite imagery. *Geophys. Res. Lett.*, 41(18):6396–6402. https://doi.org/10.1002/2014GL060641.

Vörösmarty, C. J., McIntyre, P. B., Gessner, M. O., Dudgeon, D., Prusevich, A., Green, P., Glidden, S., Bunn, S. E., Sullivan, C. A., Liermann, C. R., et al. (2010). Global threats to human water security and river biodiversity. *Nature*, 467(7315):555. https://doi.org/10.1038/nature09549.

Wang, L. (2008). *Measuring optical absorption coefficient of pure water in UV using the integrating cavity absorption meter.* PhD thesis, Texas A&M University, USA.

Whitton, B. A. and Potts, M. (2007). *The ecology of cyanobacteria: Their diversity in time and space*. Kluwer Academic Publishers, New York-Boston-Drodrecht-London-Moscow.

Williamson, C. E., Dodds, W., Kratz, T. K., and Palmer, M. A. (2008). Lakes and streams as sentinels of environmental change in terrestrial and atmospheric processes. *Front. Ecol. Environ.*, 6(5):247–254. https://doi.org/10.1890/070140.

Wolanin, A., Rozanov, V., Dinter, T., Noël, S., Vountas, M., Burrows, J., and Bracher, A. (2015). Global retrieval of marine and terrestrial chlorophyll fluorescence at its red peak using hyperspectral top of atmosphere radiance measurements: Feasibility study and first results. *Remote Sens. Environ.*, 166:243 – 261. https://doi.org/10.1016/j.rse.2015.05.018.

Wong, P., Losada, I.J., Gattuso, J.-P., Hinkel, J., Khattabi, A., McInnes, K., Saito, Y., and Sallenger, A. (2014). *2014: Coastal systems and low-lying areas. In Climate Change 2014: Impacts, Adaptation, and Vulnerability. Part A: Global and Sectoral Aspects. Contribution of Working Group II to the Fifth Assessment Report of the Intergovernmental Panel on Climate Change*. Cambridge University Press, Cambridge, New York.

Würth, C., Grabolle, M., Pauli, J., Spieles, M., and Resch-Genger, U. (2013). Relative and absolute determination of fluorescence quantum yields of transparent samples. *Nat. Protoc.*, 8(8):1535. https://doi.org/10.1038/nprot.2013.087.

Yamashita, Y., Jaffé, R., Maie, N., and Tanoue, E. (2008). Assessing the dynamics of dissolved organic matter (DOM) in coastal environments by excitation emission matrix fluorescence and parallel factor analysis (EEM-PARAFAC). *Limnol. Oceanogr.*, 53(5):1900–1908. https://doi.org/10.4319/lo.2008.53.5.1900.

Zapata, M., Rodríguez, F., and Garrido, J. L. (2000). Separation of chlorophylls and carotenoids from marine phytoplankton: A new HPLC method using a reversed phase C8 column and pyridine-containing mobile phases. *Mar. Ecol. Prog. Ser.*, 195:29–45. http://dx.doi.org/10.3354/meps195029.

Zhang, Y., Liu, M., Qin, B., and Feng, S. (2009). Photochemical degradation of chromophoric-dissolved organic matter exposed to simulated UV-B and natural solar radiation. *Hydrobiologia*, 627(1):159–168. https://doi.org/10.1007/s10750-009-9722-z.

Zhao, K., Porra, R., and Scheer, H. (2012). Phycobiliproteins. In *Handbook of Porphyrin Science*, chapter 9, pages 375–411. World Scientific Publishing Co. Pte. Ltd., Singapore. https://doi.org/10.1142/9789814397605_0005.

Zhou, W., Wang, G., Sun, Z., Cao, W., Xu, Z., Hu, S., and Zhao, J. (2012). Variations in the optical scattering properties of phytoplankton cultures. *Opt. Express*, 20(10):11189–11206. https://doi.org/10.1364/OE.20.011189.

Ziegmann, M., Abert, M., Müller, M., and Frimmel, F. H. (2010). Use of fluorescence fingerprints for the estimation of bloom formation and toxin production of microcystis aeruginosa. *Water Res.*, 44(1):195 – 204. https://doi.org/10.1016/j.watres.2009.09.035.

Acknowledgements

First, I would like to express my gratitude to my supervisor Prof. Richard Bamler for giving me the chance to conduct this research at the Chair for Remote Sensing Technology at Technical University of Munich (TUM), and for the opportunity to work at the Remote Sensing Technology Institute of the German Aerospace Center (DLR).
Secondly, I would like to thank Dr. Peter Gege who, as my topical supervisor and mentor at DLR, introduced me to the field of aquatic remote sensing. Thank you for all the time that you took for discussions and sharing your enthusiasm about aquatic remote sensing with me - whether in person, over phone or by email, even via the slowest connection from the Polarstern. I am very grateful for all the support.
I would also like to thank Dr. Peter Haschberger who, as head of the department of Experimental Methods at DLR, did not only provide me with an office but also integrated me in his division, supported my work both on organizational and on a mentoring level. Thanks for the motivating discussions and the support.
Furthermore, I would like thank Dr. Katrin Zwirglmaier and Dr. Peter Gege for initiating a truly interdisciplinary project which lured me back into science and brought me to TUM. I very much enjoyed our discussions and joint project meetings in Iffeldorf and at DLR. In this context, I would also like to thank Dr. Uta Raeder and Prof. Jürgen Geist for giving me the chance to conduct parts of my experiments at the limnological station of TUM in Iffeldorf. I enjoyed the friendly and welcoming atmosphere of this particular place. During my stays in Iffeldorf, I gained inside into aquatic sciences from a biological perspective which was brought to me mainly by my colleagues and project partners Joachim Ruber and Pia Scherer, as well as by Franziska Bauer. Thank you for fun and interesting discussions, both over phone and in Iffeldorf, and for your support during my stays. Thanks also to all other colleagues and the staff at the limnological station for your support during campaigns and stays.
It was a pleasure to share my office at DLR with Sebastian Riedel, thanks for all the remote sensing related and non related discussions.
I would also like to thank for the technical and logistic support and contributions by Thomas Schwarzmaier, Jürgen Wörishofer, Erich Bogner and Andreas Wenisch. A particularly big thanks goes to Thomas who supported me not only in campaign preparation and accomplish-

ment but was a big help when moving laboratory equipment and with his amazing technical skills and creativity. He always had a good technical advice for off-the-top-of-my-head ideas.
Additionally, I would like to thank all the students, I had the pleasure to work with, for their contributions: Felix Hundhausen, Stefan von Hößlin, Dimitrios Bellos, Kerstin Schnalzger, Joanna Janas, Runa Römke, Katharina Einberger, Athanasios Kerinis, and Matthias Reif.
Thanks also to all my colleagues at DLR, especially to Andreas Baumgartner, Claas Koehler, Hannes Brachmann, Joep Loos, Karim Lenhard, Martin Israel, Stefan Plattner, and Thomas Schwarzmaier for entertaining discussions and coffee breaks. Thank you to Eva Fahrenschon, Christine Elmauer, Bettina Bierkamp for the support in all administrative affairs.
Furthermore, I am very grateful for the support of the TUM International Graduate School of Science and Engineering (IGSSE) which provided the framework for all studies and the intra-universital and international exchange.
I also enjoyed the collaboration with colleagues from HZG Geesthacht, IGB Berlin, CAU Kiel and different DLR institutes. Thank you to Dr. Rüdiger Röttgers, Christian Utschig, Prof. Hans-Peter Grossart, Dr. Stella Berger, Dr. Jens Nejstgaard, Katja Dörnhöfer, Prof. Natascha Oppelt and Dr. Bringfried Pflug, for joint activities, exchange and collaboration.
A big thanks to Dr. Stefan Simis for hosting me at the Plymouth Marine Laboratory, outings to Dartmoor and for introducing me to both the marine institute community and Plymouth city life. Thank you for a very interesting stay.
I am very grateful to Prof. Astrid Bracher from university of Bremen and the Alfred-Wegener Institute and Prof. Alexander Damm from University of Zürich and the Swiss Federal Institute of Aquatic Science and Technology (EAWAG) who agreed to act as external expert referees for this thesis. Thank you for your interest in this work and for taking the time to review it.
Finally, I would like to thank my parents, family and friends for their wonderful and encouraging support, their patience, love and humor! A special thanks goes to Eli whose daily surprise parcel collection really cheered me up on the finish line. Also a big thanks to Fabian, for his cheerful words and his last minute pdf-to-tex support. Thank you, Kata and Arni, for all the fun activities in and around Munich which always helped to clear my mind.
And last but not least, a huge thanks to Klaus for his wonderful support, his amazing cooking skills and cooking passion, his positive spirit, and for going with me on all the small and big adventures! Looking forward to the next one! :)

This work was supported by the German Research Foundation (DFG) through the TUM International Graduate School of Science and Engineering (IGSSE), the Remote Sensing Technology Institute (IMF) at the German Aerospace Center (DLR) and the TUM Laura Bassi fund. This work was also supported by the German Research Foundation (DFG) and the Technical University of Munich (TUM) within the funding program Open Access Publishing.

A Journal publications that form part of this thesis (full paper peer review)

A.1 Publication I

ENVILAB: Measuring phytoplankton in-vivo absorption and scattering properties under tunable environmental conditions
Göritz A., von Hoesslin S., Hundhausen F., Gege P.
Optics Express 2017, Vol. 25, Issue 21, pp. 25267-25277.

This research article was published in *Optics Express (OSA Publishing)*. The following pages contain a pre-print version. The final version and updates on this article can be accessed via `https://doi.org/10.1364/OE.25.025267`.

ENVILAB: Measuring phytoplankton in-vivo absorption and scattering properties under tunable environmental conditions

ANNA GÖRITZ,[1,2*] STEFAN VON HOESSLIN,[2,3] FELIX HUNDHAUSEN,[2,4] AND PETER GEGE[2]

[1]*Technical University of Munich (TUM), Department of Civil, Geo and Environmental Engineering, Chair of Remote Sensing Technology, Arcisstr. 21, D-80333 München, Germany*
[2]*Remote Sensing Technology Institute, German Aerospace Center (DLR), Münchener Str. 20, Oberpfaffenhofen, D-82234 Weßling, Germany*
[3]*Currently with MTU Aero Engines AG, Dachauer Straße 665, 80995 München, Germany*
[4]*Currently with the Institute for Anthropomatics and Robotics, Karlsruhe Institute of Technology (KIT), Adenauerring 2, D-76131 Karlsruhe, Germany*
*anna.goeritz@tum.de

Abstract: Optical remote sensing of phytoplankton draws on distinctive spectral features which can vary with both species and environmental conditions. Here, we present a set-up (ENVILAB) for growing phytoplankton under well-defined light, temperature and nutrient conditions. The custom-built light source enables creation of light with spectral composition similar to natural aquatic environments. Spectral tuning allows for light quality studies. Attenuation is monitored with a spectrometer in transmission mode. In combination with automated spectrophotometer and fluorimeter measurements, absorption and excitation-emission-fluorescence spectra are recorded. The set-up opens the door for systematic studies on phytoplankton optical properties and physiology.

OCIS codes: (120.0120) Instrumentation, measurement, and metrology; (280.0280) Remote sensing and sensors; (300.0300) Spectroscopy; (170.6280) Spectroscopy, fluorescence and luminescence; (010.0010) Atmospheric and oceanic optics.

References and links

1. P. Falkowski, "Ocean science: The power of plankton," Nature **483**, S17–S20 (2012).
2. P. G. Falkowski, "The role of phytoplankton photosynthesis in global biogeochemical cycles," Photosynth. Res. **39**, 235–258 (1994).
3. S. Sathyendranath, J. Aiken, S. Alvain, R. Barlow, H. Bouman, A. Bracher, R. Brewin, A. Bricaud, C. W. Brown, A. M. Ciotti, L. A. Clementson, S. E. Craig, E. Devred, N. Hardman-Mountford, T. Hirata, C. Hu, T. S. Kostadinov, S. Lavender, H. Loisel, T. S. Moore, J. Morales, C. B. Mouw, A. Nair, D. Raitsos, C. Roesler, J. D. Shutler, H. M. Sosik, I. Soto, V. Stuart, A. Subramaniam, and J. Uitz, *"Phytoplankton functional types from space,"* vol. No. 15 of *Reports of the International Ocean Colour Coordinating Group* (IOCCG, Dartmouth, Canada, 2014).
4. I. Chorus and J. Bertram, eds., *"Toxic cyanobacteria in water: a guide to their public health consequences, monitoring and management,"* (E & FN Spon on behalf of the World Health Organization, 1999).
5. L. H. Pettersson and D. Pozdnyakov, *"Monitoring of Harmful Algal Bloom,"* (Springer Science & Business Media, 2013).
6. H. J. Gons, M. T. Auer, and S. W. Effler, "Meris satellite chlorophyll mapping of oligotrophic and eutrophic waters in the laurentian great lakes," Remote Sens. Environ. **112**, 4098 – 4106 (2008).
7. L. Li and K. Song, "Chapter 8 - Bio-optical modeling of phycocyanin,“ in Bio-optical Modeling and Remote Sensing of Inland Waters, D. R. Mishra, I. Ogashawara, and A. A. Gitelson, eds. (Elsevier, 2017), pp. 233 – 262.
8. M.-F. Racault, C. L. Quéré, E. Buitenhuis, S. Sathyendranath, and T. Platt, "Phytoplankton phenology in the global ocean," Ecol. Indic. **14**, 152 – 163 (2012).
9. A. G. Dekker, "Detection of optical water quality parameters for eutrophic waters by high resolution remote sensing,“Ph.D. thesis (1993).
10. S. G. H. Simis, S. W. M. Peters, and H. J. Gons, "Remote sensing of the cyanobacterial pigment phycocyanin in turbid inland water,“Limnol. Oceanogr. **50**, 237–245 (2005).

11. L. Li, L. Li, and K. Song, "Remote sensing of freshwater cyanobacteria: An extended IOP inversion model of inland waters (IIMIW) for partitioning absorption coefficient and estimating phycocyanin," Remote Sens. Environ. **157**, 9–23 (2015).
12. N. T. D. Marsac, "Occurrence and nature of chromatic adaptation in cyanobacteria," J. Bacteriol. **130**, 82–91 (1977).
13. D. Stramski and A. Morel, "Optical properties of photosynthetic picoplankton in different physiological states as affected by growth irradiance," Deep Sea Research Part A. Oceanographic Research Papers **37**, 245–266 (1990).
14. R. MacColl, "Cyanobacterial phycobilisomes," J. Struct. Biol. **124**, 311 – 334 (1998).
15. V. A. Lutz, S. Sathyendranath, E. J. H. Head, and W. K. W. Li, "Changes in the in vivo absorption and fluorescence excitation spectra with growth irradiance in three species of phytoplankton," J. Plankton Res. **23**, 555–569 (2001).
16. M. Stomp, J. Huisman, F. De Jongh, A. J. Veraart, D. Gerla, M. Rijkeboer, B. W. Ibelings, U. I. Wollenzien, and L. J. Stal, "Adaptive divergence in pigment composition promotes phytoplankton biodiversity," Nature **432**, 104–107 (2004).
17. R. L. Carneiro, M. E. V. dos Santos, A. B. F. Pacheco, and S. M. F. de Oliveira e Azevedo, "Effects of light intensity and light quality on growth and circadian rhythm of saxitoxins production in cylindrospermopsis raciborskii (cyanobacteria)," J. Plankton Res. **31**, 481 (2009).
18. H. Xi, M. Hieronymi, R. Röttgers, H. Krasemann, and Z. Qiu, "Hyperspectral differentiation of phytoplankton taxonomic groups: A comparison between using remote sensing reflectance and absorption spectra," Remote Sensing **7**, 14781–14805 (2015).
19. T. Parkin and T. Brock, "The effects of light quality on the growth of phototrophic bacteria in lakes," Arch. Microbiol. **125**, 19–27 (1980).
20. N. Korbee, F. L. Figueroa, and J. Aguilera, "Effect of light quality on the accumulation of photosynthetic pigments, proteins and mycosporine-like amino acids in the red alga porphyra leucosticta (bangiales, rhodophyta)," J. Photochem. Photobiol., B **80**, 71 – 78 (2005).
21. L. Nedbal, M. Trilek, J. Cerveny, O. Komarek, and H. B. Pakrasi, "A photobioreactor system for precision cultivation of photoautotrophic microorganisms and for high-content analysis of suspension dynamics," Biotechnol Bioeng **100**, 902–910 (2008).
22. C. L. Teo, M. Atta, A. Bukhari, M. Taisir, A. M. Yusuf, and A. Idris, "Enhancing growth and lipid production of marine microalgae for biodiesel production via the use of different led wavelengths," Bioresour. Technol. **162**, 38 – 44 (2014).
23. C.-Y. Chen, K.-L. Yeh, R. Aisyah, D.-J. Lee, and J.-S. Chang, "Cultivation, photobioreactor design and harvesting of microalgae for biodiesel production: A critical review," Bioresour. Technol. **102**, 71 – 81 (2011). Special Issue: Biofuels - II: Algal Biofuels and Microbial Fuel Cells.
24. T. Zavrel, M. A. Sinetova, D. Búzová, P. Literáková, and J. Cervený, "Characterization of a model cyanobacterium synechocystis sp. PCC 6803 autotrophic growth in a flat-panel photobioreactor," Eng. Life Sci. **15**, 122–132 (2015).
25. S. von Hößlin, "Development and validation of an automated photobioreactor system for measuring absorption and fluorescence of phytoplankton" Master's thesis, Technische Universität München (2015).
26. S. Muthu, F. J. P. Schuurmans, and M. D. Pashley, "Red, green, and blue LEDs for white light illumination," IEEE Journal on Selected Topics in Quantum Electronics **8** (2002).
27. G. P. E. Steven W. Brown, Carlos Santana, "Development of a tunable LED-based colorimetric source," J. Res. Nat. Inst. Stand. Technol. **107** (2002).
28. K. Fujiwara and A. Yano, "Controllable spectrum artificial sunlight source system using LEDs with 32 different peak wavelengths of 385 - 910 nm," Bioelectromagnetics **32**, 243–252 (2011).
29. D. Kolberg, F. Schubert, N. Lontke, A. Zwigart, and D. Spinner, "Development of tunable close match LED solar simulator with extended spectral range to UV and IR" Energy Procedia **8**, 100 – 105 (2011). Proceedings of the SiliconPV 2011 Conference (1st International Conference on Crystalline Silicon Photovoltaics).
30. A. M. Bazzi, Z. Klein, M. Sweeney, K. P. Kroeger, P. S. Shenoy, and P. T. Krein, "Solid-state solar simulator," IEEE Transactions on Industry Applications **48**, 1195–1202 (2012).
31. K. J. Linden, W. R. Neal, and H. B. Serreze, "Adjustable spectrum LED solar simulator," (2014).
32. P. Lu, H. Yang, Y. Pei, J. Li, B. Xue, J. Wang, and J. Li, "Generation of solar spectrum by using LED," (2016).
33. G. Zaid, S.-N. Park, S. Park, and D.-H. Lee, "Differential spectral responsivity measurement of photovoltaic detectors with a light-emitting-diode-based integrating sphere source," Appl. Opt. **49**, 6772–6783 (2010).
34. J.-M. Hirvonen, T. Poikonen, A. Vaskuri, P. Kärhä, and E. Ikonen, "Spectrally adjustable quasi-monochromatic radiance source based on LEDs and its application for measuring spectral responsivity of a luminance meter," Measurement Science and Technology **24**, 115201 (2013).
35. Sinus 220 from Wavelabs Solar Metrology Systems GmbH, Freiburg, Germany, http://wavelabs.de/wp-content/uploads/Brochure_Wavelabs.pdf (accessed on 31st of August 2017).
36. Ecocell from Ecoprogetti Srl, Padova, Italy, https://ecoprogetti.com/Catalogue2016.pdf (accessed on 31st of August 2017).
37. LEDSim^{TM} from Aescusoft GmbH, Freiburg, Germany, http://www.aescusoft.com/sites/default/files/public/aes_ledsim_si.pdf (accessed on 31st of August 2017).

38. F. Hundhausen, "Aufbau, Charakterisierung und Ansteuerung eines Beleuchtungs-Moduls zur Simulation variabler Unterwasser-Lichtspektren unter Verwendung von Hochleistungs-Leuchtdioden“ Bachelor thesis, Hochschule Esslingen (2015).
39. P. Gege, "Analytic model for the direct and diffuse components of downwelling spectral irradiance in water,“ Appl. Opt. **51**, 1407–1419 (2012).
40. P. Gege, Software WASI, version 4, http://www.ioccg.org/data/software.html (accessed on 17th of July 2017).
41. Axenic Synechocystis sp. PCC 6803, Pasteur Culture Collection of Cyanobacteria (PCC), Catalogue information available online: https://brclims.pasteur.fr/crbip_catalogue/faces/resultatrecherche.xhtml (accessed on 17th of july 2017), .
42. Y. Yu, L. You, D. Liu, W. Hollinshead, Y. J. Tang, and F. Zhang, "Development of Synechocystis sp. PCC 6803 as a phototrophic cell factory,“ Marine Drugs **11**, 2894–2916 (2013).
43. H. Xu, D. Vavilin, and W. Vermaas, "Chlorophyll b can serve as the major pigment in functional photosystem ii complexes of cyanobacteria,“ Proceedings of the National Academy of Sciences **98**, 14168–14173 (2001).
44. G. Johnsen, A. Bricaud, N. Nelson, B. B. Preélin, and R. R. Bidigare, *Phytoplankton pigments: characterization, chemotaxonomy, and application in oceanography* (Cambridge University, 2011), chap. "In vivo bio-optical properties of phytoplankton pigments,“ p. 525.
45. R. Rippka, J. Deruelles, J. B. Waterbury, M. Herdman, and R. Y. Stanier, "Generic assignments, strain histories and properties of pure cultures of cyanobacteria,“ Microbiology **111**, 1–61 (1979).
46. J. Lakowicz, *"Principles of Fluorescence Spectroscopy"* (Springer US, 2013).
47. C. D. Mobley, *"Light and water: radiative transfer in natural waters"* (Academic, 1994).
48. S. G. H. Simis, Y. Huot, M. Babin, J. Seppälä, and L. Metsamaa, "Optimization of variable fluorescence measurements of phytoplankton communities with cyanobacteria,“ Photosynth. Res. **112**, 13–30 (2012).
49. P. Gege, "Chapter 2 - Radiative Transfer Theory for Inland Waters," in Bio-optical Modeling and Remote Sensing of Inland Waters (Elsevier, 2017).
50. M. Stomp, J. Huisman, L. Vörös, F. R. Pick, M. Laamanen, T. Haverkamp, and L. J. Stal, "Colourful coexistence of red and green picocyanobacteria in lakes and seas,“ Ecology Letters **10**, 290–298 (2007).

1. Introduction

Phytoplankton forms the basis of the aquatic food web and plays a fundamental role in biogeochemical cycles in the ocean [1-3]. Certain phytoplankton species such as *Microcystis* are potential toxin producers and their monitoring is of interest to many stakeholders such as environment agencies, aquaculture or water resource managers [4, 5].

Due to its pigmentation and its specific scattering properties, phytoplankton can be detected in remotely sensed data from satellite, air- and shipborne as well as from ground based measurements. Optical signatures such as absorption and fluorescence by chlorophyll-*a* or specific backscattering properties serve for identification and separation from other water constituents in reflectance signals. These signatures are used to infer phytoplankton concentration and its spatial distribution on both local and global scales, e.g. [6-8]. In case of cyanobacteria, remote sensing algorithms often exploit spectral features originating from additional pigments in light harvesting complexes such as from phycocyanin [9-11]. Several studies on phytoplankton suggest that pigment composition can change not only from species to species but also with environmental conditions [12-16]. For remote sensing modelling, it is crucial to understand this variability in the inherent optical properties (IOPs), since it affects accuracy and sensitivity of retrieval algorithms. Systematic laboratory studies on phytoplankton *in-vivo* absorption and scattering characteristics under controlled environmental conditions are rare. Further, they are usually performed under so called day-light conditions (e.g. [17, 18]). For this purpose, a light source (often a fluorescent tube) is used that provides continuous radiation in the 400 nm to 700 nm wavelengths range (photosynthetically active radiation – PAR). Assuring a certain PAR emission with day-light lamps helps to create stable and reproducible culturing conditions. However, the actual spectral composition (e.g., uneven spectral distribution and high distinctive emission peaks for fluorescent lamps), and how it compares to light that phytoplankton is exposed to in its aquatic environments is usually neglected. A few studies focus on the impact of spectral composition of light on phytoplankton and algae, but for this purpose usually lamps with color filters or a few individual light emitting diodes (LEDs) are chosen [19-21].

Recently, especially in the context of bio-fuel and biotechnology applications, there have been many studies on light influencing growth behavior of bacteria and algae. The motivation for these studies often is to increase growth rates and lipid production. Light sources for culturing are optimized towards yielding highest growth rates, lipid and large-scale production rather than to resemble natural conditions [22-24]. Therefore, culturing assemblies designed for bio-fuel applications usually do not allow for an investigation of phytoplankton growth under natural light conditions.

In the present contribution, a novel set-up for optical studies on phytoplankton is presented. It allows for controlled phytoplankton growth and serves as a stage for experimental investigation of changes in phytoplankton physiology in response to varying light field, nutrient or temperature conditions. With the help of a tunable multispectral light source, phytoplankton can be grown under a broad variety of artificial and natural light conditions with respect to intensity and spectral composition. Automated spectrometric measurements allow to analyze absorption and scattering characteristics.

After an introduction to the set-up design with focus on its individual components and the spectrometric data that is recorded, the functional range is demonstrated by growth and dilution of a cyanobacteria culture.

2. Design and Realization of the ENVILAB Set-up

2.1 System Concept

Phytoplankton is grown in a photo-bioreactor under light that is provided by a custom-built multispectral LED light source tunable in both spectral composition and intensity. Growth is monitored by a spectrometer that measures spectral transmission and thus attenuation of light through the reactor chamber. Via an automated peristaltic pumping system, the growth chamber is linked with a benchtop fluorimeter and spectrophotometer with an integrating sphere for recording high precision fluorescence and absorption spectra. An estimate on scattering properties can be obtained by subtracting absorption from attenuation spectra. Stirring and automated dilution of the culture with nutrient medium allows long term experiments and studies at fixed concentration ranges. Tubes for sample transportation can be cleaned with a cleansing liquid in between or after measurements. Specifically designed software allows for live monitoring of growth parameters such as the optical depth. A sketch of the experimental set-up is depicted in Fig. 1.

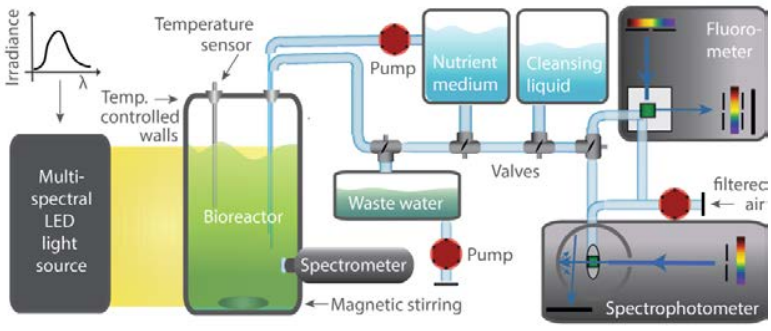

Fig. 1. Schematic sketch of the measurement set-up (modified from [25]).

2.2 Tunable LED-light Source for Spectral Light Field Simulation

Tunable LED-based light simulators, as described in the literature, are realized in a variety of designs for applications such as color rendering [26, 27], solar spectrum simulation [28-32] and

responsivity measurements [33, 34]. The respective light sources differ in number, types and combination of LEDs, as well as in their electronic control and additional optical components. Accordingly, they exhibit different characteristics in terms of spectral matching, illumination area and irradiance intensities. In photovoltaics (PV), commercial set-ups exist that are optimized towards accurate and stable reproduction of solar irradiance for characterization of PV cells [35-37]. For this purpose, assemblies with LEDs of typically around 20 different peak wavelengths are used to provide light in the visible and in parts of the ultraviolet and infrared. Illumination areas are designed to cover standard PV cell sizes. For biological studies, Fujiwara and Yano present a set-up consisting of 547 LEDs with 32 different peak wavelengths [28]. This light source provides high spectral flexibility in the 385 - 910 nm wavelength range illuminating an area of about 7cm^2. Linden et al. report on a tunable solar simulator with modular design for illumination of different sizes and shapes, but with less spectral matching flexibility in the visible (LEDs with 23 different peak wavelengths for cover the 350 to 1100 nm wavelength range) [31].

Here, we present a tunable, multispectral LED light source which is specifically designed for phytoplankton studies in a photobioreactor [38]. Special attention was paid to spectral flexibility and the resemblance of the obtained irradiance spectra to spectra found in aquatic environments. In addition to sun position and metrological conditions, spectral composition of underwater irradiance changes with depth, bottom type and vegetation, and water constituent concentrations. In order to simulate a variety of irradiance scenarios in the photosynthetically active radiation range of 400 nm to 700 nm, multiple LEDs were selected according to their high intensities, spectral peak position and bandwidths: Intensities are high enough to match (in sum) maximum spectral irradiance below the water surface. The latter was simulated using the Water Color Simulator (WASI) software (at a sun zenith angle of 0° and a sensor depth of 0 m) [26, 27]. Actual bandwidths of LEDs span around 13 to 38 nm (FWHM), with the exception of two types of phosphor coated broad band LEDs which were added to fill the gap between 530 nm and 600 nm at which LEDs are difficult to find. Position of emission peaks are chosen to assure both spectral continuity and flexibility which is needed to match target spectra [39, 40].

All LEDs (72 with 24 different peak wavelengths) are placed on Aluminium plates which together are arranged in arrays (see Fig. 2(a)). These arrays are mounted on heat dissipaters in such a way, that individual LED plates remain replaceable. The temperature of the heat sink is monitored; fans attached provide additional cooling in case the temperature rises above a given threshold (typically 25 °C).

In order to assure homogeneity of radiance across the illuminated area, the LED arrays are mounted into a mirror foil covered tube of rectangular shape (see Fig. 2(b)). Reflection at surface walls together with a diffuser plate (*PLEXIGLAS® Satinice)* at the tube's exit, restrict inhomogeneity to less than 10% within the illuminated area of 10 cm × 20 cm.

Spectral characteristics of each LED (mounted in module) were determined at lab conditions with a spectrometer (*CARL ZEISS MCS 500*, 350-1021 nm, 0.8° field-of-view) at LED current intensity of 350 mA. The calibrated spectra are stored in a database. This database forms the spectral library used to determine pulse width modulation (PWM) duties for individual LEDs in designated control software. Via a graphical user interface, target spectra can be loaded. These target spectra are either artificially composed, measured or simulated irradiance spectra that cover the 400-800 nm wavelength region and which are to be reproduced by the light source. PWM duties of the corresponding LEDs are set by the control software using a least-square-fit between the target spectrum and the sum of individual LED spectra. In a cycling mode, user defined target spectra can be varied over time. This way, day and night cycles, spectral shifts or sudden changes in illumination can be simulated. A summary on technical details of the light source can be found in Table 1.

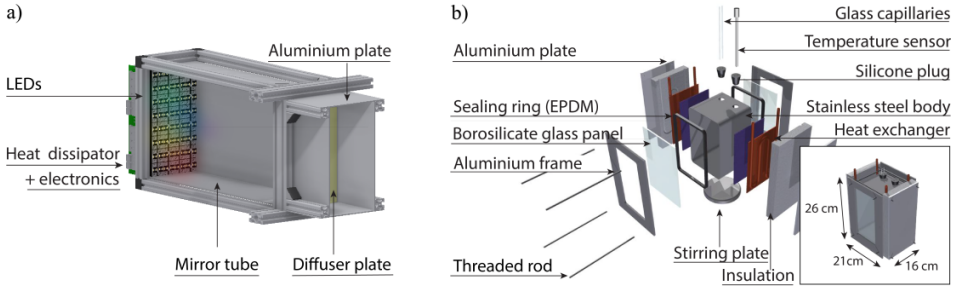

Fig. 2. (a) Schematic sketch of LED light source; (b) Scheme of bioreactor assembly in explosion view; area of glass windows match illumination area of multispectral light source (modified from [25, 38]).

Table 1. Technical specifications of the LED light source.

LEDs (total number)	72 LEDs of 24 different peak wavelengths.
Peak wavelength / FWHM [nm]	403/15, 421/16, 427/17, 433/19, 445/20, 467/25, 470/25, 472/25, 494/29, 506/32, 521/38, 522/37, 561/101, 594/18, 603/80, 621/18, 636/19, 657/20, 676/22, 684/26, 687/23, 705/25, 727/32, white/139.
Max. power/irradiance	~8 W on an area of 10 cm × 20 cm.
Hardware control	Custom designed circuit board with 32 independent PWM-controlled LED drivers (350 mA LED string current); setting of PWM duty via an I2C interface (12 bits resolution, frequencies up to 1526 Hz); temperature monitoring ICs and PWM-controlled fans.

2.3 Photobioreactor

Individual components of the photobioreactor [25] were designed while having both the microbiological and optical requirements in mind: In order to minimize contamination for microbiological studies on phytoplankton samples, all parts can be disassembled, cleaned and sterilized in an autoclave. In addition, electro-polished stainless steel of 2 mm thickness as frame material hinders deposition of phytoplankton on the inner walls. To fulfill optical demands, Borosilicate windows were chosen that provide over 90 % transmission for light in the 390 to 750 nm wavelength range.

Figure 2(b) shows a sketch of the photobioreactor assembly in explosion view. The base area was matched to a magnetic stirrer plate of 12.5 cm diameter. This way, velocity controlled mixing within the reactor is possible by inserting a Polytetrafluorethylene (PTFE) coated stirrer. The reactor's inner dimensions comprise a volume of about 3.5 l of sample liquid which can be inserted and extracted via glass tubes that are connected to flexible tubes. Liquids in the tubing connection are transported with a four-channel peristaltic pump. Fluid pathways are controlled by magnetic pinch valves which open when voltage is applied. These valves are triggered by a microcontroller. Inside the incubation chamber, temperature is monitored with a digital temperature sensor in a steel casing. On the two sides of the chamber's frame, custom-built copper plates provide heat-exchange to a liquid that can be heated or cooled by a thermostat. Insulation of the chamber body from ambient conditions assures additional temperature stability.

Software with Graphical User Interface allows creation of a timeline that includes all relevant pumping and measurement steps. A cycling function can be activated for repetitive

experiments. Once the involved volumes are defined, the software visualizes current liquid levels and allows for live temperature and optical growth monitoring.

2.4 Spectrometric Monitoring

The ENVILAB set-up provides a two-step spectral monitoring making use of a miniaturized spectrometer (*FREEDOM VIS FSV-305*, Ibsen Photonics Inc., Denmark) for transmission measurements, and of two bench-top instruments for recording absorption and fluorescence spectra (*LAMBDA®1050*, PerkinElmer Inc., U.S., and *FLUOROMAX®4*, HORIBA Scientific, Japan). The transmission of light through the sample liquid is measured regularly using the *FREEDOM VIS* spectrometer. This way, the decrease in transmission is monitored and thus, by application of Beer–Lambert's law, the growth rate is recorded. For high precision measurements with minimal scattering influence, samples are pumped into a flow-through quartz cuvette, which is mounted inside of the 150 mm diameter integrating sphere of the double beam spectrophotometer. In parallel, the fluorescence spectrum at a selected excitation wavelength or a full excitation and emission spectrum is recorded. Emitted light is detected under 90 degrees to the excitation light beam. Fluorescence measurements are normalized to excitation light intensities as measured with the instrument's reference detector, and manufacturer's correction factors are applied. After each measurement cycle, the respective cuvettes are automatically emptied into a waste collection flask and both tubes and cuvettes are flushed with a cleansing liquid.

3. Functional Tests and Discussion

3.1 Irradiance Simulation and Temperature Control

Motivation for designing the LED light source was to reproduce both artificial and natural irradiance spectra. Figure 3 illustrates target spectra resembling for three different irradiance scenarios: (a) at water surface, (b) in water rich of colored dissolved organic matter (CDOM) at 1 m depth and (c) at 3 m water depth. All spectra were simulated with WASI (for a sun zenith angle of 40 °, a total suspended matter concentration of 1.5 mg l^{-1}, an absorption of CDOM at 440 nm of 0.2 m^{-1} with a slope of S_{CDOM} = 0.014 nm^{-1} and a phytoplankton concentration of 3 µg l^{-1}). Black lines represent simulated spectra and colored lines individual LEDs, while grey diamonds reflect the total LED irradiance.

In Fig. 3, maximum relative deviation (per nm) from target irradiance of 54% in case (a) and 34-35% in case (b) and (c) can be observed, with an average deviation of 14%, 6% and 8%, respectively. This is caused by spectral overlap of the emission peaks. Especially if lower water depths are to be simulated, higher average deviation from target spectra will be observed. The reason for this is that, in larger depth, more light gets absorbed by the water itself, leading to pronounced spectral features around 600 nm. The coverage of the corresponding wavelength range with broad band LEDs does not allow for proper reproduction of these spectral features in the irradiance spectra. At the time when the light source was built, no suitable LEDs were available to cover the 550 to 600 nm wavelength regions.

Despite these drawbacks, the light source provides much more flexibility in resembling natural irradiance spectra than conventional light sources. No additional filters are necessary to avoid unwanted peaks. In addition, relative intensities of "overshoots" are much smaller compared to fluorescent tubes, where distinctive peaks of chemical compounds affect the emission spectrum.

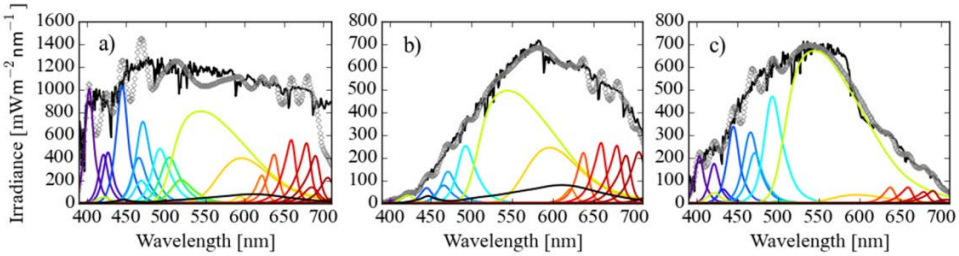

Fig. 3. Calculated (black solid line) and simulated (grey circles) downwelling irradiance spectra for different ambient light scenarios under a sun zenith angle of 40°: (a) at water surface (sensor depth = 0 m), (b) with high CDOM concentration at 1 m depth (a_{CDOM} = 2 m^{-1}) and (c) at 3 m water depth. Colored lines reflect individual LED spectra.

Temperature stability inside the photobioreactor was tested in the laboratory at room temperature. For this purpose, 1.2 l and 3 l of purified water was cooled and heated via the heat exchanger using the thermostat which was to set values in the range of 1 to 40 °C. Tests confirmed stable temperature conditions in the range of 2.6 to 39.1 ± 0.1 °C with maximum deviation of 3°C for most extreme temperatures and depending on the filling level. Tests confirmed that the ENVILAB enables a variety of studies at temperatures typically found in natural water bodies [25].

3.2 Automated Spectral Measurements and Nutrient Control

First phytoplankton growth tests were performed with *Synechocystis sp*. PCC 6803 [41]. This cyanobacterium is widely studied [42], making it an interesting model organism.
For bioreactor functionality validation, the culture was kept under light with fixed spectral composition. In order to produce an intensity similar to previous culturing conditions, the irradiance spectrum (at 2 m water depth; simulated with *WASI* default parameters) was additionally attenuated by a factor of 10. Light was switched on and off in a day-and-night cycle (14 h/10 h). A baseline measurement with pure nutrient medium was performed before adding the culture.

To validate the growth monitoring ability, transmission of a culture of PCC 6803 bacteria was measured with the *FREEDOM VIS* spectrometer during a period of 6.3 days with a series of 10 spectra every 15 minutes. Dark current measurements were recorded directly before start of the growth experiment and during night phases. The corresponding 3540 extinction spectra are shown in Fig. 4(a). They illustrate the continuous growth during day times which result in an increase in attenuation. The attenuation peaks correspond to phytoplankton pigments. The peak around 436 nm and the peak at around 673 nm can be associated with absorption by chlorophyll pigments. The peak around 620 – 630 nm relates to phycocyanin absorption [43, 44].

In order to test automated measurement cycles and nutrient supply, a series of dilution measurements with PCC 6803 (grown under traditional day-light) was recorded. Over 24 hours, a dense culture inside the photobioreactor was stepwise diluted with nutrient medium (BG11 modified from [45]) until noise contribution became too high to acquire meaningful spectra [25]. Figure 4(b) shows the corresponding absorption spectra. The decrease in absorption corresponds to a reduction of cyanobacteria concentration. The absorption decreases linearly over the wavelength range of 300 nm to 700 nm as shown in the inset of Fig. 3(b).

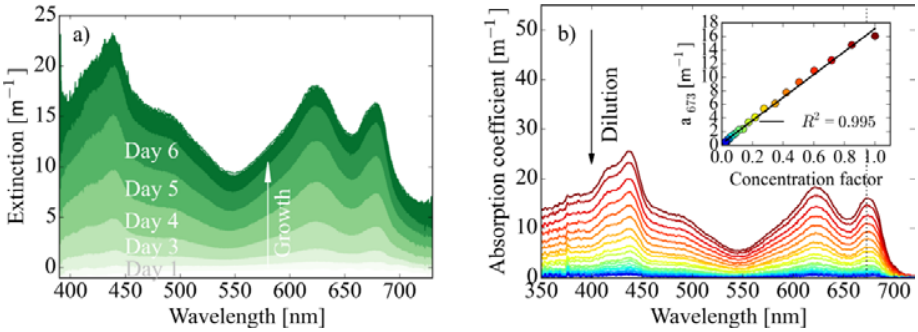

Fig. 4. (a) Growth of *Synechocystis sp*. (PCC 6803) monitored through the reactor windows; transmission was measured ten times during day every 15 minutes over a period of ~ 6.3 days leading to the depicted 3540 spectra. (b) Absorption spectra during automated dilution of a PCC 6803 culture; inset: corresponding concentration factor vs. absorption at 673 nm.

At each dilution step, excitation-emission spectra were recorded. In order to reduce acquisition time, the wavelength range of interest was split in two: a) with an excitation (λ_{ex}) from 200 – 700 nm and an emission (λ_{em}) from 575 – 800 nm, b) with λ_{ex} from 200 – 540 nm and λ_{em} from 250 – 575 nm. The two EEM (excitation-emission matrices) spectra at every dilution step were automatically recorded right after each other (5 nm wavelength steps, 2 nm bandpass front and exit slit, 0.1 s integration time). After adding the spectra to combined EEMs, the pure nutrient EEM was subtracted. Figure 5(a) illustrates an example of such a blank corrected EEM. High intensities at diagonal values ($\lambda_{ex} = \lambda_{em}$) are due to elastic scattering (Rayleigh) and instrument effects. Also second order effects at doubled emission wavelength ($\lambda_{em} = 2\lambda_{ex}$) can be observed. For further analysis, Rayleigh scattering was masked out, leading to blanks in diagonal matrix values which occur as gaps in the excitation spectrum at 680 nm emission as shown in Fig. 5(b).

EEM spectra show that fluorescence emission maxima were shifted towards longer wavelengths as compared to absorption spectra, which is to be expected for this inelastic scattering process. Fluorescence intensity at 620 nm excitation and 680 nm emission ($f_{430/685}$) decreases linearly with dilution (see inset of Fig. 5(b)). This proves that measurements were not impacted by non-linear effects such as the inner filter effect (i.e. reabsorption of fluorescence photons by the sample) [25, 46].

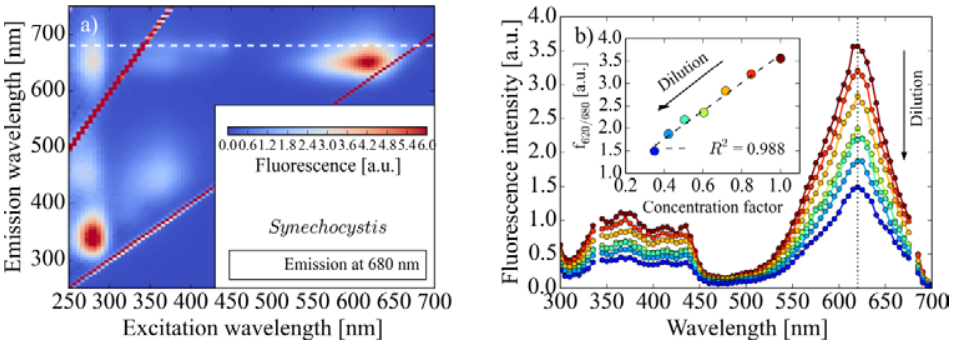

Fig. 5. (a) Excitation-mission spectrum of *Synechocystis sp*. (PCC6803) after blank subtraction. The dashed line indicates the excitation spectrum at 680 nm emission. (b) Excitation spectrum at 680 nm for PCC 6803 at different dilution steps. The inset indicates linear decrease of fluorescence intensity at 620 nm excitation and 680 nm emission with dilution.

4. Conclusion and Outlook

In this paper, a novel automated spectrometric set-up (ENVILAB) was presented, which enables controlled phytoplankton growth and at the same time allows for the characterization of its bulk attenuation, absorption and fluorescence characteristics. The custom-built, tunable, multispectral LED light source permits systematic studies on phytoplankton under varying light conditions. Consisting of 72 LEDs of 24 different peak wavelengths, irradiance intensities and spectral compositions of the light source are tunable in a wavelength range of about 380 to 700 nm. Maximum irradiance matches that of natural sun close to the water surface (with a zenith angle of 0°). The flexibility of the LED light source for natural light field simulation has been demonstrated on three examples at different underwater conditions. Thus, together with under-water irradiance simulation not only artificial but also under-water light scenarios similar to natural conditions (in terms of spectral composition) can be reproduced. In combination with the time line function, both sudden and slow changes in spectral composition and its impact on phytoplankton growth and optical properties can be studied. Further improvement of the light source should address finer reproduction of spectral feature, especially in the 550 to 600 nm wavelength range.

In the photobioreactor of the ENVILAB, cultures of phytoplankton can be grown under controlled environmental conditions. Temperature stabilization is realized via a heat exchanger which in combination with a thermostat assures temperatures in the range of 2.6 to 39.1 ± 0.1 °C. Currently, no gas exchange is included but additional openings in the steel frame of the bioreactor provide access if future implementation (e.g. of a bubbling system) is desired.

For validation of growth monitoring, *Synechocystis sp.* (PCC 6803) was grown in a stirred culture. Monitoring the LED light through the flat transmission windows using an external miniaturized spectrometer has been proven to be suitable for monitoring of changes in the attenuation of the culture.

Nutrient supply and automated measurement procedures were tested by continuously diluting a *Synechocystis* PCC 6803 culture with nutrient medium. With every automated dilution step, samples were programmed to be withdrawn from the bioreactor via the automated peristaltic pumping system, transported into the photometer and fluorimeter and spectra were recorded. This way, *in-vivo* absorption and fluorescence measurements could be performed externally with minimally invasive sample extraction. Absorption was determined inside an integrating sphere of the photometer, while fluorescence was recorded in a compact steady state fluorimeter which allows for excitation-emission measurements. For fixed concentration range studies, current attenuation of the phytoplankton culture inside the photobioreactor can be measured and the corresponding optical depth values are fed into the automated nutrient dilution programming loop. This loop controls concentration by mixing fresh nutrient medium into the bioreactor until the optical density has reached the desired value.

In summary, ENVILAB provides a novel laboratory environment for systematic studies on phytoplankton physiology and optical properties. Next to attenuation measurements, which give insight into scattering properties, absorption and fluorescence measurements on *in-vivo* samples are collected. This spectral information is highly valuable as it builds the basis for water constituent and pigment discrimination in many applications ranging from remote sensing to optical *in-situ* devices [47-49]. Reduction of uncertainties in the IOPs and understanding its natural variability may therefore improve water quality monitoring in the long term [7]. In addition, control and adjustability of environmental factors during phytoplankton growth (such as light and its spectral composition, temperature and nutrient supply), enable experiments in various fields of phytoplankton research such as chromatic adaptation, day-night cycle or niche behavior [13, 50].

Funding

A. Göritz gratefully acknowledges support by the Deutsche Forschungsgemeinschaft (DFG) through the TUM International Graduate School of Science and Engineering (IGSSE) and a TUM Laura-Bassi-Fellowship.

Acknowledgments

The authors would like to thank Christoph Haisch, Michael Seidel and Katrin Zwirglmaier for discussions at an early stage of this project. Further, they want to thank Pia Scherer and Joachim Ruber for support in culture handling and cultivation techniques and Katharina Einberger and Jürgen Wörishofer for technical assistance.

A.2 Publication II

Göritz A., Gege P.

GLEAM: A spectral absorption and fluorescence model for dissolved organic matter in the UV-VIS

(Submitted)

This research article has been submitted for full-paper peer review. In order to avoid potential licensing/copyright conflicts, the following pages contain a draft version of the manuscript.

GLEAM: A spectral absorption and fluorescence model for dissolved organic matter in the UV-VIS

Authors: Anna Göritz[a,b*], Peter Gege[b]

[a] Technical University of Munich (TUM), Department of Civil, Geo and Environmental Engineering, Chair of Remote Sensing Technology, Arcisstr. 21, D-80333 München, Germany

[b] German Aerospace Center (DLR), Remote Sensing Technology Institute, Münchner Str. 20, Oberpfaffenhofen, D-82234 Weßling, Germany

[*]Corresponding author: anna.goeritz@tum.de

Abstract

Colored Dissolved Organic Matter (CDOM) plays a pivotal role in aquatic ecosystems and biogeochemical cycles, and is monitored regularly in the context of water quality assessment. Current remote sensing algorithms exploit the spectral absorption characteristics of CDOM usually in terms of two parameters of an exponential function, i.e., the absorption coefficient and the slope parameter at a reference wavelength (e.g., at 440 nm). Fluorescence properties are rarely considered. We demonstrate that Gaussian functions accurately approximate the optical properties of CDOM, i.e., the absorption coefficient and the fluorescence quantum efficiency, and the Raman-normalized fluorescence radiance over a wide spectral range in the UV-VIS. A parametrization is derived for the spectral characteristics of each of these CDOM properties. The proposed model (GLEAM: Gaussian light emission and absorption model) enables simulation of both absorption and fluorescence properties of CDOM in good correspondence with

measurements from ten German lakes. A spectral quantum efficiency matrix has been derived that can be used for including CDOM fluorescence in radiative transfer models. Finally, we discuss the potential of the proposed model for CDOM composition analysis, radiative transfer modelling and remote sensing.

Key Words: colored dissolved organic matter (CDOM), absorption, fluorescence, quantum yield, quantum efficiency, excitation-emission-matrix, aquatic remote sensing, bio-optical modelling, spectroscopy, lake

1. Introduction

Colored dissolved organic matter (CDOM) strongly influences light availability in water and hence affects aquatic organisms concerning, e.g. photo-protection and shading (Ayoub et al., 2012; Thrane et al., 2014; Williamson et al., 2015). The high concentration of CDOM found in many coastal and inland waters can strongly alter absorption and reflectance of the water body in the short wavelengths and thus mask spectral signatures of other water constituents such as phytoplankton (Gege, 2017). CDOM itself is a common indicator for water quality and its abundance and composition is investigated in numerous studies (Coble, 2007; Fasching et al., 2014; Stedmon et al., 2011). Its relationship to dissolved organic carbon and the overall role in biogeochemical cycles has recently sparked the interest in CDOM, resulting in many investigations and publications (Asmala et al., 2012; Dutkiewicz et al., 2015; Hestir et al., 2015; Kutser et al., 2015; Spencer et al., 2009; Spencer et al., 2012; Vantrepotte et al., 2015).

CDOM is, by definition, the substances that remain in the water after filtering a water sample

through a filter with 0.2 µm pore size. Many of its compounds are produced during the decay of plant material; others originate from microbial sources (Kirk, 2011). The fluorescent part of dissolved organic matter is often referred to as FDOM. Fluorophores found in dissolved organic matter may include amino acids, simple phenols, indoles, phenylpropanes, oxygen ring compounds, lignines, quinines and alkaloids (Aiken, 2017).

For decades now, remote sensing of CDOM has relied mainly on its absorption characteristics which are typically modelled by an exponential function that descends from the blue towards the red wavelengths (Bricaud et al., 1981; Organelli et al., 2014). The exponent of this function is related to the composition of CDOM. Hence, it is used, together with the absorption coefficient at a reference wavelength, to characterize the optical properties of CDOM of a given water type. The slope parameter has been shown to vary not only with CDOM composition but also with the wavelength range in which it is determined (Loiselle et al., 2009; Massicotte and Markager, 2016).

With respect to fluorescence, there have been several studies on LIDAR (light detection and ranging) applications for CDOM retrieval. They exploit the fluorescence emission signal after excitation at a chosen wavelength, e.g. at 355 nm (Hoge et al., 1995; Vodacek et al., 1995; Nieke et al., 1997; Palmer et al., 2013). In passive remote sensing however, dissolved organic matter (DOM) fluorescence is typically neglected, although studies exist that point out the potential impact on radiative transfer inside the water, especially in waters with comparably high DOM, low Chlorophyll-*a* and low suspended particle concentrations (Pozdnyakov et al., 2002). In the field of water spectroscopy and water chemistry, fluorescence techniques in the UV and short visible wavelength range (often 250 to 550 nm) have been proven to provide powerful tools for the analysis of DOM, its composition, its origin, degradation products and the role in

biochemical processes. In this context, multivariate data analysis has become very popular. So called chemo-metric approaches include methods such as principal component analysis (PCA) or multivariate decomposition methods, e.g. parallel factor analysis (PARAFAC) (Murphy et al., 2013; Murphy et al., 2014). These methods are useful for the statistical analysis of excitation-emission data sets, but they don't allow for an analytical description of individual measurements. Further, they are usually applied to monitor spectral composition changes and not for analysis of spectra in absolute fluorescence units.

To the authors' knowledge, only very few approaches for analytical models of CDOM fluorescence exist. These include a simple model with a fixed emission of Gaussian shape (Pozdnyakov et al., 2002) and a model which relates the center wavelengths and widths of a one-dimensional Gaussian function via a linear regression to the excitation wavelengths (Hawes, 1992). The parameters of the latter function were derived from quantum efficiency measurements of marine fulvic and humic substance samples.

Here, we propose a combined model for the absorption and fluorescence properties of dissolved organic matter. It builds up on the approaches by Korshin et al., 1997) and Gege, 2000) for modelling the spectral absorption coefficient of CDOM as a sum of Gaussian distributions. Their approach is extended by a two-dimensional model for spectral fluorescence radiance of dissolved organic matter which makes use of a sum of bivariate normal distributions resulting in the proposed "Gaussian Light Emission and Absorption Model" (GLEAM). The variability of the GLEAM parameters is studied by analyzing spectral measurements of CDOM from ten lakes with varying CDOM concentration. To make GLEAM applicable for quantitative radiative transfer simulations, not only relative spectral features but also absolute values (absorption coefficients and fluorescence quantum yields) are evaluated.

2. Methods

2.1. Sampling

Absorption and fluorescence excitation-emission spectra of CDOM from ten lakes with varying CDOM concentration were measured. These samples were taken from the first half meter below water surface. Sample locations and dates of sampling are summarized in the next section (see Table **2**). After transportation to the laboratory in bottles which were protected against light, samples were filtered through pre-rinsed filters of 0.22 µm pore size (MILLEX®GV, Durapore® PVDF Membrane). Filtrates that could not be analyzed immediately were stored in foil covered bottles in the refrigerator or a cooling box (approx. 4°C and 10°C respectively).

2.2. Absorption measurements

Transmission through the samples in quartz cuvettes (Suprasil, Hellma® Analytics, Germany) was measured from 200 nm to 850 nm in 1 nm steps using a double beam spectrophotometer (LAMBDA®1050, PerkinElmer Inc., U.S.). Measurements were performed with cuvettes of 5 cm path lengths at room temperature (without temperature stabilization). For selected samples, additional scans of transmission through 1 cm and 10 cm cuvettes were collected. All measurements were performed against an empty reference beam. In separate measurements, pure water (Ultrapure H_2O, HPLC grade, Alfa Aesar® GmbH & Co KG, Germany) transmission spectra were recorded using the same set of cuvettes and instrument settings. Transmission spectra of CDOM samples were normalized to transmission of pure water (measured in the same cuvette). The natural logarithm of this ratio, normalized to the negative cuvette length, was used to determine the spectral absorption coefficient according to the Beer-Lambert law. For multi-

component Gaussian modeling, no further correction was applied since potential temperature and background effects were considered at a later step in the analysis (see section 2.3). For the exponential modelling, a background correction was applied following the approach in (Gege, 2004) at a wavelength of 820 nm. The 5 cm cuvette measurements provided insufficient signal at short wavelengths where CDOM absorption strongly increases. Measurements with the 1 cm cuvette, in turn, could not resolve the low absorption of CDOM at long wavelengths. For this reason, data from the 5 cm cuvettes was used for the wavelength range 220 to 850 nm, and data from the 1 cm cuvettes for the wavelength range from 200 to 220 nm.

In a next step, absorption spectra were converted from wavelength to wavenumber scale in order to reveal underlying symmetric structures due to molecular absorption bands which are expected to appear on the energy scale. This was done by applying the following conversion rules:

$$\nu = 10^7 \cdot \frac{1}{\lambda} \ , \tag{1}$$

$$a_{CDOM}(\nu) = a_{CDOM}(\lambda) \cdot 10^7 \cdot \frac{1}{\lambda^2} \ . \tag{2}$$

In these equations, the wavenumber values ν are in units of [cm^{-1}], the wavelength values λ in units of [nm] and the absorption coefficient a_{CDOM} is in units of [m^{-1}].

For the inner-filter-effect correction (see chapter 2.3), absorbance spectra of the samples (CDOM plus water) were determined in two different ways. For measurements, where 5 cm and 10 cm cuvette measurements were available, the absorbance A_{CDOM+W} was calculated as:

$$A_{CDOM+W}(\lambda) = -\frac{1}{0.10-0.05} \cdot \ln\left(\frac{T^{10}_{CDOM+W}(\lambda)}{T^{5}_{CDOM+W}(\lambda)}\right) \cdot \frac{0.01}{\ln 10} . \tag{3}$$

Here, $T^{10/5}_{CDOM+W}(\lambda)$ stands for the transmission of the sample in a 10 cm and 5 cm cuvette, respectively. The last factor in Eq. (3) represents the conversion from absorption to absorbance in

a 1 cm cuvette. The second approach was applied to single cuvette measurements of 5 cm length:

$$A_{CDOM+W}(\lambda) = -\frac{1}{0.05} \cdot \ln\left(\frac{T^5_{CDOM+W}(\lambda)}{T_{cw}(\lambda)}\right) \cdot \frac{0.01}{\ln 10}. \quad (4)$$

This equation requires an estimate for the cuvette window transmission, $T_{cw}(\lambda)$, which was determined in separate measurements following the approach in (Gege, 2004).

2.3. Fluorescence measurements

CDOM fluorescence was measured using 1 cm quartz cuvettes in a fluorometer (FLUOROMAX®4, HORIBA Scientific, Japan) at room temperature (without temperature stabilization). The instrument consists of a xenon light source, two Czerny-Turner monochromators with adjustable slits, a UV-enhanced silicon photodiode as reference detector and a photomultiplier tube for detection of fluorescence light. Fluorescence excitation-emission-matrices (EEM), $f(\lambda_x, \lambda_m)$, were recorded by stepping through a chosen range of excitation wavelengths, and for each step scanning across a certain range of emission wavelengths. In this study, the spectra $f(\lambda_x, \lambda_m)$ were recorded with an excitation and emission step width of 5 nm, a slit width (both excitation and emission) of 2 nm and an integration time of 0.1 s/step. The chosen wavelength ranges differed amongst the samples, but all measurements covered at least the range from 240 nm to 500 nm for excitation and from 240 nm to 600 nm for emission. Measured intensities were normalized to the signals of a reference detector which monitors the intensity changes of the light source. The manufacturer's instrument correction factors, which account for wavelength dependencies of the system components, were applied to both reference and fluorescence detector signals. Following the standardization scheme described in (Goletz et al., 2011), $f(\lambda_x, \lambda_m)$ measurements were corrected for the inner-filter-effect which refers to light attenuation of the excitation and emission light by the sample itself. This was done using

the approach by Lakowicz which considers both the so called first order (attenuation of the incoming light) and second order (attenuation of the emitted fluorescence light) effect (Lakowicz, 2006):

$$f_{ifc}(\lambda_x, \lambda_m) = f(\lambda_x, \lambda_m) \cdot 10^{\frac{A_{CDOM+W}(\lambda_x)+A_{CDOM+W}(\lambda_m)}{2}} , \quad (5)$$

where $f_{ifc}(\lambda_x,\lambda_m)$ is the-inner-filter-effect corrected fluorescence at excitation wavelength λ_x and emission wavelength λ_m. $A_{CDOM+W}(\lambda_x;\lambda_m)$ is the absorbance of the sample at excitation and emission wavelength, respectively. More details on the derivation of this equation can be found in (MacDonald et al., 1997).

After these corrections, which were applied to both samples and blanks, f_{ifc}-EEMs were converted to Raman units [R.u.] (Lawaetz and Stedmon, 2009):

$$f_{R.u.}(\lambda_x, \lambda_m) = \frac{f_{ifc}(\lambda_x,\lambda_m)}{\int_{\lambda_{371}}^{428} f_w(350,\lambda_m)\ d\lambda_m} , \quad (6)$$

with $f_w(350, \lambda_m)$ the Raman signal of a pure water sample measured with same settings as the CDOM measurements. In order to determine the wavelength integrated Raman signal of pure water (Ultrapure H_2O, HPLC grade, Alfa Aesar® GmbH & Co KG, Germany) at an excitation wavelength of λ_x= 350 nm, a Gaussian function was fitted to the respective emission spectrum of each pure water f_{ifc}-EEM. With this function, the 5 nm spaced emission measurements were interpolated in 1 nm steps. The area under this curve from 371 nm to 428 nm was taken as proxy of the integrated Raman signal of pure water. All $f_{ifc}(\lambda_x, \lambda_m)$ measurements were normalized to this value.

Finally, pure water blanks, measured with the same instrument settings and the same cuvette as CDOM measurements, were subtracted from $f_{R.u.}(\lambda_x, \lambda_m)$, and Rayleigh and Raman signals were masked out resulting in $f_{CDOM}(\lambda_x, \lambda_m)$ in [R.u.]:

$$f_{CDOM}(\lambda_x, \lambda_m) = f_{R.u.}^{sample}(\lambda_x, \lambda_m) - f_{R.u,}^{water}(\lambda_x, \lambda_m), \quad (7)$$

The Rayleigh mask sets all $f_{CDOM}(\lambda_x, \lambda_m)$ values with identical excitation and emission wavelengths (corresponding to elastic scattering) equal to zero. The same applies to the adjacent f_{CDOM}-EEM values to account for not perfectly monochromatic light emission and detection. Although most of the Raman signal was eliminated after blank subtraction, an additional mask was applied which covers potentially remaining signatures. This mask was calculated assuming a Stokes shift of 3400 cm^{-1} (Lawaetz and Stedmon, 2009; Faris and Copeland, 1997) and a peak width of 1000 cm^{-1}. For quantum yield and efficiency estimates, values with $\lambda_m < \lambda_x$ and $\lambda_m > 2 * \lambda_x$ were set to zero as well. Whenever obvious emission values were deleted by the mask, their values were reconstructed by linearly interpolating the emission wavelength range above 520 nm and the excitation wavelength range from 290 nm to 400 nm. Prior to any further modelling, the f_{CDOM}-EEM spectra were converted to wavenumber units in analogy to Eqs. (1) and (2).

The fluorescence radiance measurements $f_{CDOM}(\lambda_x, \lambda_m)$ were used to derive two material specific parameters: the spectral quantum efficiency $\eta(\lambda_x, \lambda_m)$ and the quantum yield $\Phi_{CDOM}(\lambda_x)$. $\eta(\lambda_x, \lambda_m)$ is defined as the rate at which photons are emitted with wavelengths between λ_m and $\lambda_m + d\lambda_m$ divided by the rate at which photons with wavelengths between λ_x and $\lambda_x + d\lambda_x$ are absorbed (Gordon, 1979). $\Phi_{CDOM}(\lambda_x)$ is the integral of $\eta(\lambda_x, \lambda_m)$ over all emission wavelengths.

Quantum yield measurements were calibrated using a NIST traceable fluorescence reference standard. It contains a solution of $1.28 \cdot 10^{-6}$ mol/L quinine sulfate in 0.105 mol/L perchloric acid (NIST SRM 936a, Starna Cells Inc., U.S.). The fluorescence intensities of the standard and its blank were determined in the same instrument with the same settings as for the

CDOM measurements. Following the procedure described in (Würth et al., 2013), the quantum yields of CDOM were calculated in the wavelength range where the quinine and CDOM fluorescence signal overlap, according to the following equation:

$$\Phi_{CDOM}(\lambda_x) = \Phi_{QS}(\lambda_x) \cdot \frac{\int f_{CDOM}(\lambda_x,\lambda_m)\lambda_m \, d\lambda_m}{\int f_{QS}(\lambda_x,\lambda_m)\lambda_m \, d\lambda_m} \cdot \frac{1-10^{-A_{QS}(\lambda_x)}}{1-10^{-A_{CDOM}(\lambda_x)}} \cdot \frac{n^2_{CDOM+W}}{n^2_{QSS}} \quad . \qquad (8)$$

Here, the subscript QS stands for quinine sulfate, CDOM for a given CDOM sample, CDOM+W for the sample in water and QSS for the quinine sulfate in solution f *is* the fluorescence signal corrected for instrument effects, *A* the absorbance and *n* the refractive index.

The value of $\Phi_{QS}(\lambda_x)$ at λ_x = 347.5 nm was taken from literature: Φ_{QS} = 0.6 (Velapoldi and Tønnesen, 2004). Since the difference between the refractive index of water and 0.105 mol/L perchloric acid is rather small (Velapoldi and Mielenz, 1980), p.79), the ratio of squared refractive indices in Eq. (8) was approximated to be unity. Fluorescence measurements were performed in 5 nm steps. For calculation of the integrals in Eq. (8), all emission spectra were resampled to a 1 nm spaced grid. Then, the integral was approximated by a sum over all emission wavelengths from 330 nm to 700 nm.

Quantum yield measurements require a fluorescence standard with overlapping absorption and emission ranges. Quinine sulfate absorbs light in the range from about 270 nm to 400 nm and emits light in a wavelength range of about 385 nm to 700 nm (Würth et al., 2013). In order to extend the quantum yield obtained with the NIST standard to wavelengths above 400 nm and below 270 nm, a second approach was taken. Assuming that wavelength dependent instruments effects are correctly accounted for by the manufacturer's instrument calibration, a factor for the conversion of fluorescence from Raman units to fluorescence quantum efficiencies for selected instrument settings was derived. By multiplying the fluorescence intensities $f_{CDOM}(\lambda_x, \lambda_m)$ with

this conversion factor K and the inverse absorbance fraction, the CDOM spectral quantum efficiency $\eta(\lambda_x, \lambda_m)$ was calculated as:

$$\eta(\lambda_x, \lambda_m) \approx K \cdot \frac{f_{CDOM}(\lambda_x,\lambda_m)\cdot\lambda_m}{1-10^{-A_{CDOM}(\lambda_x)}}. \quad (9)$$

This equation is similar to Eq. (4) in (Green and Blough, 1994) but instead of the absorption coefficient, the absorbance is used and no integration is applied.

The conversion factor, K, was calculated from quinine sulfate measurements recorded using the same settings as the CDOM EEMs by

$$K = \frac{\Phi_{QS}(347.5)}{\int f_{QS}(347.5,\lambda_m)\lambda_m \, d\lambda_m} \cdot \left(1 - 10^{-A_{QS}(\lambda_x)}\right). \quad (10)$$

2.4. Absorption models

Following the approach in (Gege, 2000,Gege,), the wavenumber dependent absorption coefficient was modelled using a sum of Gaussians and a temperature and a background term:

$$a_{CDOM}(\nu) = \sum_{i=1}^{n} \frac{A_i}{\sqrt{2\pi}\cdot\sigma_i} e^{-\frac{1}{2}\left(\frac{\nu-\nu_{c,i}}{\sigma_i}\right)^2} + \Delta T \cdot \alpha_W(\nu) + \; B \cdot a_B(\nu). \quad (11)$$

In this equation, n represents the total number of Gaussian curves. Their amplitudes, widths and center wavenumbers are denoted A_i, σ_i, and $\nu_{c,i}$, respectively. ΔT is the temperature difference between the sample and the reference, while α_W stands for the temperature gradient of pure water absorption (Röttgers et al., 2014). The last term $B \cdot a_B(\nu)$ represents a background signal where B stands for the magnitude and $a_B(\nu)$ for the normalized spectral dependency. This background signal, which is frequently observed, may result from instrument effects such as baseline drift or stray light, or from sample artefacts such as scattering of microbubbles or reflection differences between sample and reference cuvette. As usual (Babin et al., 2003; Gonçalves-Araujo et al., 2018), a_B was assumed constant and thus set equal one.

For comparison with the conventional exponential approach, absorption (after correction of background effects) was modelled using the following equation:

$$a_{CDOM}(\lambda) = a_{CDOM}(440) \cdot e^{-S(\lambda-440)}, \quad (12)$$

where the S stands for the slope parameter and 440 nm was chosen as reference wavelength. Eqs. (11) and (12) were fitted to absorption measurements using a least squares fit and a fit range from 200 nm to 850 nm and 300 to 700 nm, respectively.

2.5. Fluorescence model

The fluorescence EEM measurements in Raman units, $f_{CDOM}(\lambda_x, \lambda_m)$, were converted to wavenumber scale, $f_{CDOM}(\nu_x, \nu_m)$, and then modelled by a sum of n' bivariate normal distributions with amplitudes FA'_i, correlation coefficients ρ_i, center frequencies for excitation $\nu_{xc,i}$ and emission $\nu_{mc,i}$, standard deviations $\sigma'_{x,i}$ and $\sigma'_{m,i}$ together with a constant offset f_B:

$$f_{model}(\nu_x, \nu_m) = f_B + \sum_{i=1}^{n'} \frac{FA'_i}{2\pi\sigma'_{x,i}\sigma'_{m,i}\sqrt{1-\rho_i^2}} e^{-\frac{1}{2(1-\rho_i^2)}\left[\frac{(\nu_x-\nu_{xc,i})^2}{\sigma'^2_{x,i}} - \frac{2\rho(\nu_x-\nu_{xc,i})(\nu_m-\nu_{mc,i})}{\sigma'_{x,i}\sigma'_{m,i}} + \frac{(\nu_m-\nu_{mc,i})^2}{\sigma'^2_{m,i}}\right]}. \quad (13)$$

Temperature effects were neglected and a fit range from 240 nm to 500 nm (excitation) and 240 nm to 600 nm (emission) was chosen for the least squares fit of Eq. (13) to $f_{CDOM}(\nu_x, \nu_m)$ measurements.

2.5. Spectral quantum efficiency model

The spectral quantum efficiency measurements $\eta(\lambda_x, \lambda_m)$ obtained from Eq. (9) were converted to wavenumber scale, $\eta(\nu_x, \nu_m)$, and then modelled with a sum of n^* non-normalized bivariate normal distributions with amplitudes ηA_i^*, correlation coefficients ρ_i^*, center frequencies for

excitation $\nu^*_{xc,i}$ and emission $\nu^*_{xc,i}$, standard deviations $\sigma^*_{x,i}$ and $\sigma^*_{m,i}$ and a constant offset f_B:

$$\eta_{model}(\nu_x, \nu_m) = \eta_B + \sum_{i=1}^{n^*} \eta A_i^* \cdot e^{-\frac{1}{2\left(1-\rho_i^{*2}\right)}\left[\frac{\left(\nu_x-\nu^*_{xc,i}\right)^2}{\sigma^{*2}_{x,i}} - \frac{2\rho\left(\nu_x-\nu^*_{xc,i}\right)\left(\nu_m-\nu^*_{mc,i}\right)}{\sigma^*_{x,i}\sigma^*_{m,i}} + \frac{\left(\nu_m-\nu^*_{mc,i}\right)^2}{\sigma^{*2}_{m,i}}\right]}. \quad (14)$$

This equation was fitted to the $\boldsymbol{\eta(\lambda_x, \lambda_m)}$ spectra in wavelength range of as 240 nm to 500 nm (excitation) and 240 nm to 600 nm (emission) using a least-squares fit.

3. Results

3.1 Absorption measurements

Absorption spectra were first modelled by fitting Eq. (11) to the measured spectra. The number of Gaussian curves in the wavelength range of 200 nm to 850 nm was first chosen to be three. This should account for the peak around 203 nm as observed by Korshin et al., 1997) and Gege, 2000). The remaining two peaks were meant to account for two components which were detected in the EEM data (see section 3.2). The first peak detected in fluorescence data was also found in absorption data, but not the second one. Therefore, in the next run, absorption was fitted by considering only two Gaussian components. For this fit, the first peak was assumed to be located at 203 nm. For the second peak, the center wavelength was fitted. Retrieved Gaussian parameters are summarized in Table **1**. The corresponding average temperature difference ΔT between CDOM and water sample was (-1.4 ± 1.3) °C and for the background an average correction of (0.005 ± 0.007) m^{-1} was derived. The average residual, which is the sum of the squared differences between the measured and the modelled absorption spectra, was 0.005 ± 0.007, indicating a well-converged fit.

While the peak width variation of absorption peak #1 was rather small (standard deviation 136 cm^{-1}), the variation of peak #2 was somewhat bigger (standard deviation 1265 cm^{-1}). The amplitudes of both peaks (A_1 and A_2) did not show any correlation.

Tab.1. Parameters (average ± standard deviation) derived from fit of *n* = 10 CDOM absorption measurements with a sum of two Gaussian curves according to Eq. (11).

Peak #	A_i [$m^{-1}cm^{-1}$]	$\lambda_{c,i}$ [nm]	σ_i [cm^{-1}]
1	6092 ± 2968	203 (set)	2854 ± 136
2	2537 ± 2149	253 ± 7	7644 ± 1265

In a second run, all baseline corrected absorption spectra were fitted with the exponential approach (see Eq.(12)). Figure 1 shows an example of a CDOM absorption measurement which was fitted with the sum of two Gaussian curves (a) and an exponential function (b). The Gaussian model fits the measurement reasonably well for the entire wavelength range, while the exponential model approximates the observed line shape accurately only in a narrower range. Not only do the peaks in the UV get lost in the exponential model, it also underestimates CDOM absorption at wavelengths above 500 nm (though temperature effects become relevant here as well).

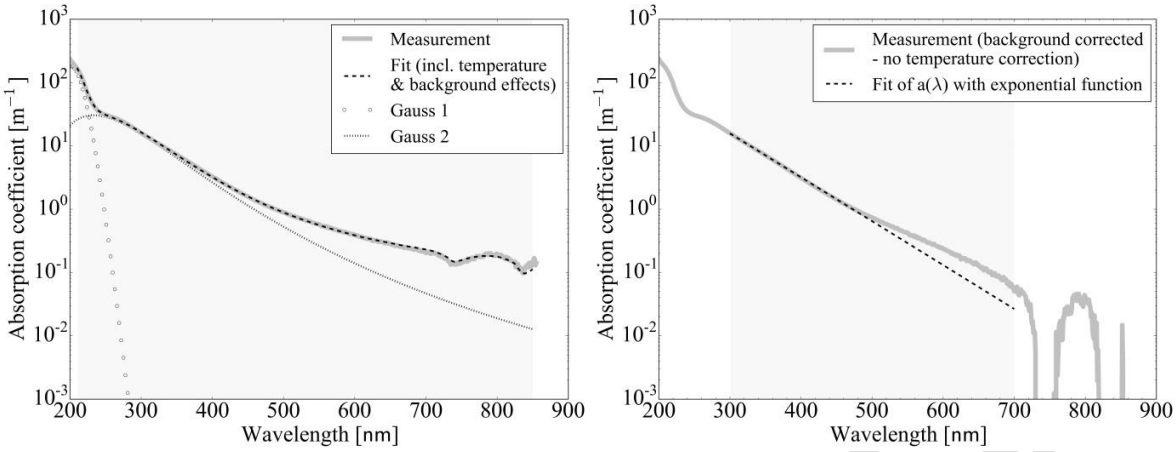

297

298 *(a)* *(b)*

299 Fig.1. *CDOM absorption spectrum (logarithmic scale) of a sample from lake Gröbensee*
300 *modelled (a) with a sum of two Gaussian curves and a temperature and background correction*
301 *term; and (b) with the conventional approach of an exponential curve which is applied after*
302 *background correction to $a_{CDOM}(\lambda)$. The fit range is marked as grey area.*

303 In order to show the range of CDOM concentration covered by the data set, results for
304 exponential fitting are summarized in Table (**2**). Note that the offset that was subtracted
305 according to the background correction at 820 nm (see Section 2.2.) was unusually high for four
306 out of ten spectra (GRS, OSS, LUS and SHS). Therefore, a higher uncertainty for the
307 corresponding $a_{CDOM}(440)$ values than indicated by the fit error has to be assumed in these cases.
308 In further analysis, the background was used as uncertainty for $a_{CDOM}(440)$ for these
309 measurements. It was found that background values retrieved with combined Gaussian,
310 temperature effect and background modeling according to equation Eq. (11) showed a linear
311 relation to the background determined from 820 nm but offset values were about 1-2 orders of
312 magnitude lower.

313

Tab.2. Lakes and their locations, sampling date and CDOM parameters from exponential fit over wavelength range of 300 nm to 700 m after background correction.

Lake (Abbre-viation)	Location [N, E]	Date [dd/mm/yy]	$a_{CDOM}(440)$ [m^{-1}]	S_{CDOM} [m^{-1} nm^{-1}]	Background B [m^{-1}]
Gröbensee (GRS)	47.812028, 1.300028	13/11/15	1.681 ± 0.005	0.016 ± 0.002	0.154
Lustsee (LUS)	47.810000, 11.295056	13/11/15	0.238 ± 0.001	0.019 ± 0.002	0.118
Gr.Ostersee (OSS)	47.790028, 11.301972	13/11/15	0.597 ± 0.004	0.019 ± 0.002	0.249
Schilfhütten-see (SHS)	47.773833, 11.317639	13/11/15	0.927 ± 0.005	0.015 ± 0.002	0.313
Ammersee (AMS)	11.1705320, 47.9915608	14/12/17	0.910 ± 0.002	0.019 ± 0.002	0.011
Pilsensee (PLS)	11.1955689, 48.0232661	14/12/17	0.411 ± 0.002	0.021 ± 0.002	-0.004
Staffelsee (SFS)	11.1794319, 47.6869834	14/12/17	2.582 ± 0.007	0.017 ± 0.002	0.018
Kochelsee (KOC)	11.361754, 47.645756	18/01/18	0.450 ± 0.001	0.019 ± 0.002	0.006
Stechsee	47.803975,	18/01/18	0.745 ±	0.017 ±	0.020

(STC)	11.296841		0.002	0.002	
Walchensee	47.617447,	18/01/18	0.165 ±	0.022 ±	0.022
(WLS)	11.345988		0.001	0.002	

316

317 **3.2 Fluorescence measurements**

318 CDOM fluorescence of each water sample was measured and calibrated as described in
319 Section 2.3. in terms of excitation-emission matrices (EEMs). After correction of the effects
320 introduced by the instrument and the sample geometry (inner-filter-effect), the data were
321 converted to Raman units [R.u.] and transformed from length scale (wavelength) to frequency
322 scale (wavenumbers). These calibrated f_{CDOM}-EEM measurements were analyzed by fitting two-
323 dimensional Gaussian functions to the data (Eq. (13)).

324 For remote sensing applications, the most relevant wavelength range is the visible. In this range,
325 two major peaks appear in all spectra. Therefore, it was analyzed whether two fluorescing
326 components ($n' = 2$) are sufficient to model all measured f_{CDOM}-EEMs. Since the peak in the UV
327 was not completely covered in all measurements, its center position could not be determined
328 with high accuracy and was therefore set to 255 nm (average position of samples where a fit was
329 possible in the first run).

330 The two-component approach matched very well the observed fluorescence spectral intensities
331 of all samples. Figure 2(a) shows an example of an f_{CDOM}-EEM measurement and its fit with Eq.
332 (13). Dashed lines indicate cuts through the f_{CDOM}-EEM at λ_x = 255 nm (emission spectra) and
333 λ_m = 455 nm (emission spectra). Figure 2(b) and 3(b) depict these spectra for all CDOM samples
334 together with the respective fit results. They illustrate the good spectral matching capabilities of

the model. The abbreviations of lake names are explained in Table (**2**). Average values of fit results are summarized in Table (**3**). Here, peak center frequencies were reconverted to wavelength units. The excitation peak center positions, $\lambda_{xc,i}$ and $\lambda_{mc,i}$, showed a low variability (standard deviation of 7 nm). For the correlation coefficients ρ_i, stable values were retrieved for both peaks. The derived widths, $\sigma_{x,i}$ and $\sigma_{m,i}$, were slightly more stable for peak #2 which is almost completely covered by the measurements, while peak #1 was only partly recorded. The retrieved background signal was close to zero and therefore not included in Table (**3**).

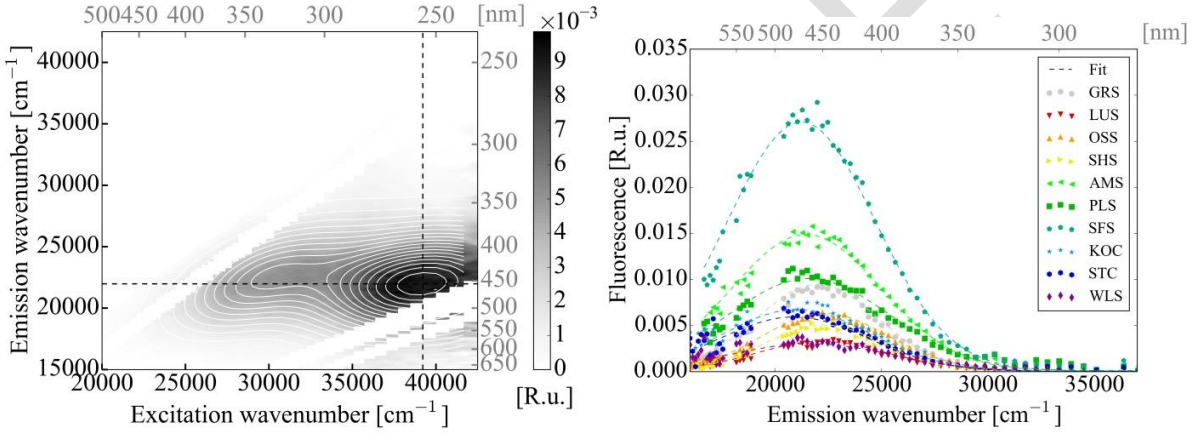

(a) (b)

Fig.2. *(a) EEM surface plot of a $f_{CDOM}(\lambda_x, \lambda_m)$ measurement of a CDOM sample from Gröbensee; the diagonal white lines show the masked areas of Rayleigh and Raman scattering, the contours represent the fit with a sum of bivariate normal distributions and the dashed black lines indicate an excitation/emission of 255/455 nm. (b) Emission spectra at λ_x= 255 nm for all CDOM samples and corresponding fit results (dashed lines).*

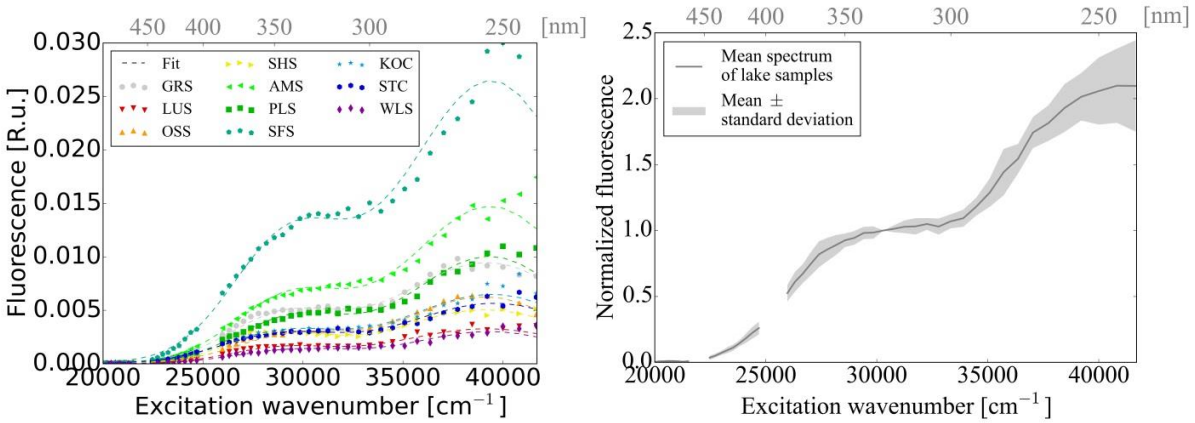

(a) (b)

Fig.3. *(a) Fluorescence excitation spectra at λ_m= 455 nm for all CDOM test samples and respective fit results (dashed lines) (b) Mean fluorescence excitation spectrum at λ_m= 455 nm normalized at 340 nm.*

Tab.3. Parameters (average ± standard deviation) derived from fit of *n* = 10 measurements of fluorescence intensity in Raman units, $f_{CDOM}(\lambda_x, \lambda_m)$, ($R^2$ = 0.96 ± 0.03) with a sum of two bivariate normal distributions according to Eq. (13).

Peak #	ρ_i	$\lambda_{xc,i}$ [nm]	$\lambda_{mc,i}$ [nm]	$\sigma_{x,i}$ [cm^{-1}]	$\sigma_{m,i}$ [cm^{-1}]
1	0.22 ± 0.06	255 (set)	462 ± 11	4211 ± 331	3217 ± 331
2	0.57 ± 0.04	341 ± 7	450 ± 13	2308 ± 147	2148 ± 197

The amplitudes of fluorescence peak #1 (FA_1) and peak #2 (FA_2) correlated linearly (see Fig. (4)). The slope for this linear relation was determined as 0.14 ± 0.01 (R^2 = 0.9973).

Fig.4. *Relation between fluorescence peak amplitudes retrieved with the two component approach.*

3.3. Relation between absorption and fluorescence parameters

The wavelength range of absorption peak #1 is not covered by the fluorescence measurements. When plotting the amplitudes of absorption peak #2 (A_2) against fluorescence peak 1 (FA_1), a linear relation was observed. The corresponding amplitudes and the linear regression with a slope of 217.09 ± 39.01 R.u. cm^{-1} (R^2 = 0.8421) are depicted in Fig. 5(a).

For comparison, the absorption coefficient at 440 nm, as derived with the exponential function, is plotted in Fig. 5(b) against the amplitudes of fluorescence peak #2. Here, the relationship is not as clear as in Fig. 5a (R^2 = 0.497).

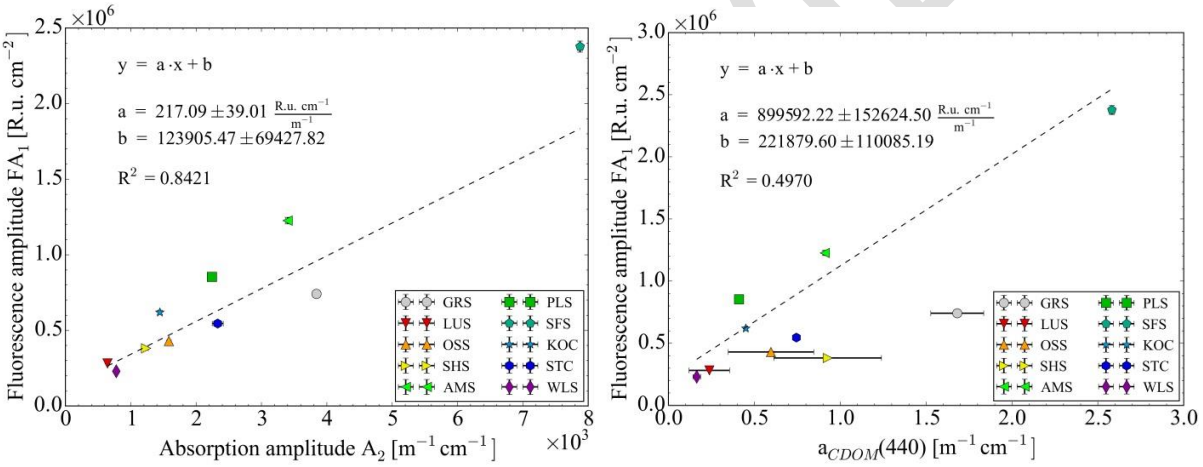

(a) (b)

Fig.5. *(a) Relation between the amplitudes of absorption peak #2 (A_2) and fluorescence peak #1 (FA_1). (b) Relation between the absorption coefficient at 440 nm, $a_{CDOM}(440)$, and the amplitude of fluorescence peak #1 (FA_1).*

3.4. Spectral quantum yield measurements

In order to validate absorbance measurements of the quinine standard, measured values were

compared to the values listed in the NIST certificate (NIST, 1994). The decadic molar absorption (i.e. the negative decadic logarithm of the transmittance normalized to the concentration) at 250 nm, 347.5 nm and 365 nm was compared to values of the certificate. The two latter agree with NIST values within five percent, the value at 250 nm deviates by about seven percent.

For all CDOM samples the quantum yields were calculated using Eq. (8). The quantum yield of quinine sulfate, which is a function of the excitation wavelength, is typically reported for 347.5 nm. For quinine sulfate in sulfuric acid, the variation of the quantum yield for excitation wavelengths between 224 nm and 390 nm is rather small (Velapoldi and Mielenz, 1980), p.51). Here, the quantum yield of the fluorescence standard ($1.28 \cdot 10^{-6}$ mol/L quinine sulfate in 0.105 mol/L perchloric acid) was assumed to be constant at 0.6 between 280 nm and 390 nm excitation wavelength, and corresponding CDOM quantum yields were determined in 5 nm steps in the respective range. While the spectral shape of the quantum yield was found to be similar for all ten samples, the magnitude at maximum (370 nm) varied up to a factor of 2.7. In order to compare the results with values reported in (Zepp and Schlotzhauer, 1981) and in (Hawes, 1992), the average quantum yield at 350 nm, $\Phi_{CDOM}(350)$, was determined as 0.010 ± 0.003. The uncertainty represents the standard deviation over all samples. Fig. 6(a) shows the quantum yield estimates for all CDOM samples as derived from the relative quantum yield measurements. The mean spectrum was modelled with a polynomial function of 4th order ($y = ax^4 + bx^3 + cx^2 + dx + e$). The fit result (dashed line) is shown in Fig. 6(b) (with $a = (-4.11 \pm 0.44) \cdot 10^{-10}$, $b = (5.36 \pm 0.59) \cdot 10^{-7}$, $c = (-2.62 \pm 0.29) \cdot 10^{-4}$, $d = (5.68 \pm 0.64) \cdot 10^{-2}$, and $e = (-4.63 \pm 0.43)$).

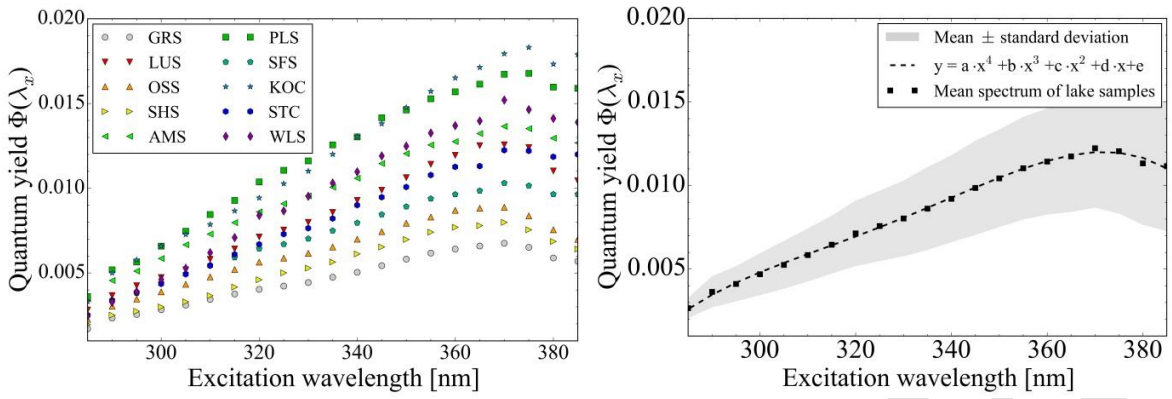

(a) (b)

Fig.6. *(a) Quantum yield of CDOM samples as a function of excitation wavelength as determined in relative quantum yield measurements against quinine sulfate. (b) Mean values of quantum yield normalized at 370 nm (black dots) and mean values ± standard deviation (grey filled area).*

CDOM quantum efficiencies outside the wavelength range of quinine sulfate absorption (270 nm to 400 nm) were determined with Eq. (9) and Eq. (10). The conversion factor from Raman units to quantum efficiencies for our measurement conditions was determined as $K = (3.2 \pm 0.3) \cdot 10^{-8}$ $R.u.^{-1}nm^{-1}$. An example of a resulting spectral quantum efficiency matrix (η-EEM) is shown in Fig. 7(a). The highest efficiency was found to be centered at an excitation wavelength of 393 nm and an emission wavelength of 496 nm. These maxima were determined by fitting Eq. (14) to the spectra (see Fig. 7(b)). The two-dimensional Gaussian model does not approximate the spectral shape of all η-EEMs as accurate as the f_{CDOM}-EEMs, but the correspondence is still reasonable, as can be seen in Fig.9. The average Gaussian parameters of this retrieval are summarized in Table **4**.

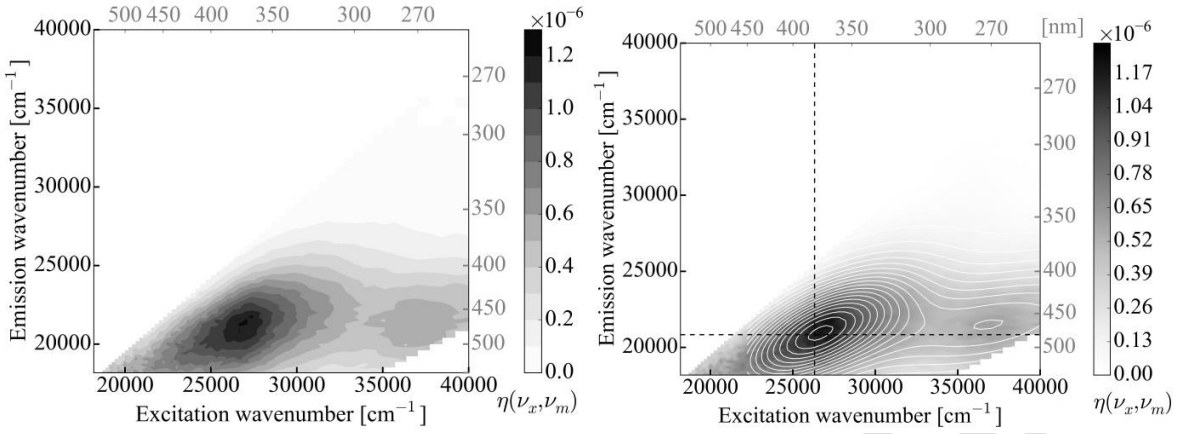

(a) (b)

Fig.7. *(a) Spectral quantum efficiencies $\eta(\lambda_x, \lambda_m)$ of a CDOM sample (Gröbensee) as determined with an instrument specific correction factor. (b) Modelled quantum efficiency spectrum of the same sample; the dashed lines indicate an excitation at 380 nm and an emission at 480 nm.*

The quantum efficiencies of the fluorescence were lower for peak #2 compared to peak #1.

By summing up over the measured emission wavelength range of the η-EEM in wavelength units, which had been resampled to 1 nm intervals, an approximation of the quantum yield $\Phi(\lambda_x)$ was derived for each CDOM sample. The results are shown in Fig. 8(a). The spectral shape in the wavelength range from 290 nm to 390 nm is similar to the results from quantum yield determination using a fluorescence standard. The average spectra are depicted in Fig. 8(b).

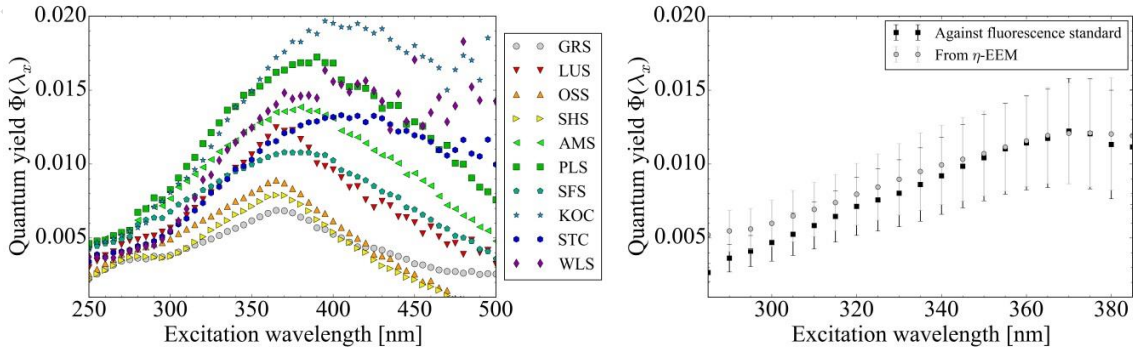

(a) (b)

Fig.8. *(a) Quantum yields as a function of the excitation wavelength as determined from the η-EEM. (b) Comparison of quantum yields calculated relative to a quinine sulfate fluorescence standard and derived from η-EEMs for excitation wavelengths between 290 and 390 nm.*

The dashed lines in Fig. 7(b) indicate an excitation at 380 nm and emission at 480 nm. These spectra are summarized in Fig. 9 representing the ten samples and the modeling results.

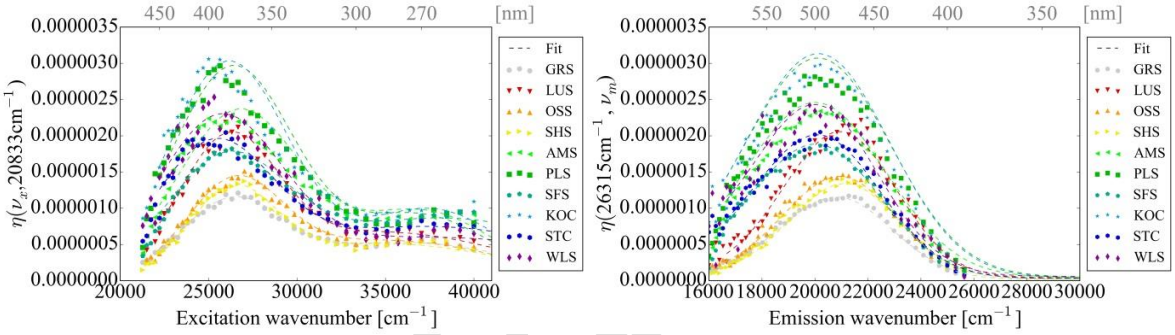

(a) (b)

Fig.9. *(a) Measured and modelled excitation spectra $\eta(\lambda_x, \lambda_m)$ at an emission wavelength of λ_m=480 nm for all CDOM samples. (b) Measured and modelled emission spectra $\eta(\lambda_x, \lambda_m)$ at an excitation wavelength of λ_x=380 nm for all CDOM samples.*

Tab.4. Parameters (average ± standard deviation) derived from fit of *n* = 10 measurements of quantum efficiency, $\eta(\lambda_x, \lambda_m)$, with a sum of two-dimensional Gaussian curves (R^2 = 0.9585 ± 0.0233) according to Eq. (14). The peak amplitude ratio $\eta A_1/\eta A_2$ was 2.7 ± 0.7)

Peak #	ρ_i	$\lambda_{xc,i}$ [nm]	$\lambda_{mc,i}$ [nm]	$\sigma_{x,i}$ [cm^{-1}]	$\sigma_{m,i}$ [cm^{-1}]
1	0.65$^{(*)}$ (set)	393 ± 19	496 ± 24	2365 ± 290	1746 ± 204

2	0.6 ± 0.1	273 ± 6	479 ± 16	5029 ± 479	2113 ± 489

443 *Determined in a pre-fit run.

444

445

446 **4. Discussion**

447 **4.1 Absorption modelling**

448 Identification and differentiation of different compounds in CDOM with optical techniques is
449 difficult due to the fact that it comprises a mixture of different molecules and complexes. Their
450 overlapping optical signatures and broadened spectral bands make a distinction of individual
451 constituents very challenging. Nevertheless, changes in dominant optical active compounds may
452 help to give insight in the underlying chemical composition. Korshin et al., 1997) proposed an
453 approach for modelling the absorption of natural organic matter based on consideration of the
454 electronic structure of benzene as the simplest aromatic molecule. Building up on the energy
455 transitions bands for this molecule, they suggest a superposition of three absorption bands similar
456 to the three bands of benzene centered at around 180 nm, 203 nm and 253 nm. With this and the
457 modelling results described in (Gege, 2000) in mind, CDOM absorption in the range of 200 nm
458 to 850 nm was modelled with a multi component Gaussian model. For the CDOM samples from
459 ten different lakes, two components were found to be sufficient to spectrally model the
460 absorption measurements. Using Gaussian curves for modelling the spectral shape of CDOM
461 absorption has already successfully been demonstrated in (Gege, 2000; Schwarz et al., 2002;
462 Massicotte and Markager, 2016): Gege (2000) fitted absorption spectra from Lake Constance

and Schussen river (Germany) and found dominant components centered at 204.7 ± 1.0 nm, 233.4 ± 5.4 nm and 251.0 ± 11.4 nm. Schwarz and colleagues fitted five bands to absorption measurements of CDOM from the Wisła River (Poland). They found the energy bands (for summer samples) centered at around 172 nm, 188 nm, 194 nm, 200 nm and 226 nm. Massicotte and Markager (2016) decomposed CDOM absorption in the wavelength range of 240 nm to 700 nm from samples which were collected from the open Atlantic Ocean at different depths. They found seven groups centered at 269 nm, 299 nm, 344 nm, 375 nm, 407 nm, 444 nm and 485 nm. In the present study, only two components in the 200-850 nm regions were relevant (see section 3.1). With the first Gaussian's center position set to 203 nm, the second's was fitted and an average position of 253 ± 7 nm was found. This is in agreement with Korshin at al.'s theory and matches the position of the third Gaussian component reported by Gege (2000). The high variability of this peak's width (standard deviation of 1265 cm^{-1}) may indicate a more complex underlying structure which is not captured by the two-component model or result. Nevertheless, this approach proved to be suitable for accurately approximating absorption measurements over a wide spectral range from 200 to 850 nm. It enables a more accurate description than the conventional exponential model, allows physical interpretation and limits the amount of free parameters. Almost all measurements were affected by temperature effects in the spectral range from 700 to 850 nm which could be successfully corrected by the inclusion of the temperature gradient of the absorption coefficient of pure water into modelling. Running various fits with variable peak centers showed that ideally the main peak at 203 nm should be resolved by the absorption measurement in order to accurately capture its position. When measurements do not cover the spectral region below 350 nm, the Gaussian deconvolution can lead to serious mathematical problems if the peak wavelengths and widths are treated as fit parameters (Sipelgas

et al., 2003). The wavelength range of 700 nm to 850 nm proved to be of specific importance for temperature and background effect correction and should therefore always be included in measurements. Since absorption spans various orders of magnitude, the combination of measurements with different cuvette lengths proved to be very successful for optimizing signals in the respective wavelength ranges.

4.2 Fluorescence modelling

The proposed multicomponent two-dimensional Gaussian model of CDOM fluorescence proved to be very successful in modelling the fluorescence spectra of the data set from ten lakes. Peak positions obtained by fitting the fluorescence data agreed well with maxima in CDOM excitation-emission measurements that have been previously reported. Fluorescence peak #1 ($\lambda_{xc,1}$ = 255 nm (set) and $\lambda_{mc,1}$ = 461 ± 5 nm) can be assigned to a peak which is sometimes referred to as peak "α' ", peak "A" or "humic like" with an excitation wavelength between 250 nm and 260 nm and an emission of 380 nm to 480 nm (Parlanti et al., 2000; Coble, 1996). Note that the varying scanning ranges used in different studies may affect the emission wavelength reported in the literature. Coble et al., 1998) for example, found the maximum in their measurements at 260 nm but with an excitation scanning range starting at 260 nm. The peak "A" has been associated with both fulvic acids and humic substances from autochthonous and allochthonous origin respectively and was related to terrestrial sources (Stedmon and Markager, 2005; Stedmon et al., 2003; Coble, 2007). The excitation center wavelength also matches the peak position from absorption "peak 3" at 251.0 ± 11.4 nm as observed by Gege, 2000) and may be related to the benzene-like energy band at around 253 nm as described by Korshin et al., 1997).

508 Position of fluorescence peak #2 ($\lambda_{xc,2}$ = 341 ± 7 nm and $\lambda_{mc,2}$ = 450 ± 13 nm) falls into the range
509 of values reported for a peak referred to as peak "C" or "α". In literature, the peak position was
510 found at an excitation wavelength between 320 nm and 360 nm and an emission wavelength
511 between 420 nm and 460 nm. Sources include terrestrial, anthropogenic and agricultural material
512 (Coble, 2007).
513 The correlation between these two peaks, as observed in the present study, agrees with (Coble
514 et al., 2014) where it is reported that both peaks are always observed together. But the linear
515 relation observed here with an R^2 of 0.9973 opposes the statement that the ratio of the two peaks
516 varies.
517 Attempts of fitting f_{CDOM}-EEMs with a three component bivariate normal distribution (results
518 not shown) also yielded good agreement for all samples. While the two major components were
519 similar to the peaks determined by the two component model, the center position of the third
520 peak with lowest amplitude varied amongst the samples detected. The data set was too small to
521 reliably derive the Gaussian parameters for this third peak.
522 The center excitation wavelength of fluorescence peak #1 could not be reliably determined for all
523 samples and was therefore set to a fixed value of 255 nm. The partial coverage of this peak in the
524 EEM scanning range may be a reason for this. Thus, an extension of the measurement to
525 wavelengths between 220 nm and 250 nm is recommended for further studies. However, this has
526 to be done with caution since wavelength dependent instrument effects may increase and the
527 intensity of the light source and therefore the signal to noise ratio decreases.

528 **4.3. Relation of absorption and fluorescence**

529 A linear relation between the absorption and fluorescence amplitudes of the Gaussian

components was observed. This, together with the linear relation of the two major fluorescence peaks and the fairly stable peak positions and widths, indicate the potential of reconstruction of the fluorescence signature from absorption measurements and vice versa.

(Green and Blough, 1994) showed that the integrated fluorescence radiance is proportional to the absorption coefficient at the excitation wavelength. With the help of the Gaussian model for both absorption and fluorescence, a simulation of the CDOM fluorescence magnitude in a wide range of excitation and emission wavelengths from about 250 nm to 500 nm excitation and 300 nm to 600 nm emission becomes possible.

4.4. Quantum efficiencies

For the data set which was used for testing the proposed model, quantum yields as determined with a quinine sulfate fluorescence standard were in the range of about 0.003 to 0.018 in the wavelength range of 300 to 400 nm. All quantum yields showed similar spectral shapes with a maximum at around 370 nm. This is in agreement with the study by Hawes who determined the quantum yields for seven humic acid (HA) and four fulvic acid (FA) marine samples and found a maximum of $\Phi_{CDOM}(\lambda_x)$ for the FA samples at 370 nm (Hawes, 1992). His HA samples revealed a spectrally quite flat quantum efficiency spectrum with no obvious spectral trend. He determined an average value for $\Phi_{CDOM}(350)$ for marine CDOM of 0.010 which matches the results of 0.010 ± 0.003 obtained in the present study. The uncertainty represents the variability (standard deviation) over the samples. High variability in the magnitude of quantum yields was also observed by Zepp and Schlotzhauer, 1981) for aquatic humic substances who determined values between 0.0005 and 0.012 for samples from different sources (marine and freshwater and

552 soil) but with a lower average for $\Phi_{CDOM}(350)$ of 0.0045 ±0.0038.

553 With the help of a conversion factor, the determination of quantum efficiencies could be
554 extended to a wider spectral range, resulting in so-called η-EEMs. The highest fluorescence
555 quantum efficiencies were observed at emission wavelengths ranging from 460 to 500 nm.
556 Results for quantum yields in the excitation range of 290 to 390 nm derived from the η-EEM
557 agreed well with values derived from the measurements that were calibrated directly using a
558 quinine sulfate fluorescence standard. The authors would like to encourage others to add absolute
559 intensity information to their spectral composition analysis in order to create a more extensive
560 data set for future model validation.

561 A modeling of the η-EEMs in wavenumber units with a two-component and two-dimensional
562 Gaussian function allowed capturing the observed spectral features. This enables an analytical
563 description of the quantum efficiency in absolute terms which, together with the absorption and
564 fluorescence modeling, may be of high interest for modelling of fluorescence effects in aquatic
565 environments and remote sensing applications.

566

567 **5. Conclusions**

568 In the present study, we introduced a multi-component Gaussian model for the analytical
569 description of fluorescence of dissolved organic matter. Together with a Gaussian model for
570 absorption picking up the approaches of Korshin et al., 1997) and Gege, 2000), it enables a
571 simulation of the spectral properties of in the UV-VIS. In order to demonstrate its modelling
572 capabilities it was applied to measurements of absorption and excitation-emission fluorescence
573 of CDOM samples from ten German lakes.

574 For absorption, two Gaussian components proved to be sufficient for reconstructing the major
575 spectral features in the range from 200 nm to 850 nm. The two peaks exhibited fairly stable
576 center wavelengths at 203 nm and 253 ± 7 nm. Both were also found by Gege, 2000) and agree
577 with the theory of Korshin et al., 1997). This two-component model gave a very good spectral
578 approximation to the absorption measurements of CDOM with better spectral matching
579 compared to the conventional exponential approach.
580 The multi-component Gaussian approach was also very successful for modelling excitation-
581 emission fluorescence measurements (scanning range: 240 to 500 nm excitation, 240 to 600 nm
582 emission). Again, only two peaks were required to capture the major spectral signatures for all
583 measurements. Here, the peak maxima were located at $\lambda_{xc,1}$ = 255 nm (set) and $\lambda_{mc,1}$ = 461 ± 11
584 nm with widths of σ_x = 4211± 331 cm^{-1} and σ_m = 3217 ± 331 cm^{-1} for peak 1. The second peak
585 was found at $\lambda_{xc,2}$ = 341 ± 7 nm and $\lambda_{mc,2}$ = 450 ± 13 nm with σ_x = 2308 ± 1147 cm^{-1} and σ_m =
586 2148 ± 197 cm^{-1}.
587 The peak positions retrieved with the multicomponent two-dimensional Gaussian model fall into
588 the range typically observed in CDOM EEM analysis (Coble, 2007). The amplitudes of both
589 fluorescence peaks are highly correlated (R^2 = 0.9973), and also the amplitudes of the peak in
590 absorption and fluorescence correlated with each other (R^2 = 0.8421). This allows the
591 reconstruction of one parameter from the other and makes combined modelling of CDOM
592 absorption and fluorescence possible.
593 The quantum yield of CDOM was determined using two methods. Direct measurements were
594 performed in the spectral range from 290 nm to 390 nm using a calibrated quinine sulfate
595 fluorescence standard. Indirect measurements were made in the spectral range from 240 nm to
596 500 nm by converting Raman-normalized fluorescence measurements to spectral quantum

efficiency and then integrating over the emission wavelengths. The methods provided consistent results in the overlapping spectral region. This demonstrates the validity of the conversion method and hence the reliability of the derived spectral quantum efficiency matrix. The obtained η-EEM is an inherent optical property of CDOM and required for including fluorescence properly in radiative transfer models.

The CDOM quantum yields determined in this study were found quite variable in terms of magnitude, but exhibited a striking consistent spectral shape in the wavelength range from 290 nm to 390 nm with a maximum around 370 nm. The average quantum yield at 350 nm was determined as 0.010± 0.003 and matches very well the result of (Hawes, 1992) who studied marine fulvic and humic acids.

The spectral quantum efficiencies that were determined from η-EEM showed that even though fluorescence intensities are highest in the UV, energy conversion is most pronounced in the visible. Thus, CDOM fluorescence may be of relevance for remote sensing applications even though quantum yields are quite small.

In summary, a multi-component Gaussian light emission and absorption model (GLEAM) for modelling both the absorption and fluorescence signatures as well as the quantum efficiency of CDOM was proposed and successfully demonstrated on absorption and excitation-emission fluorescence measurements from ten German lakes. It allows a decomposition of CDOM spectra into different optically active groups of compounds and enables their spectral analysis. Further, it gives an analytical description of the fluorescence signatures which is of high interest for radiative transfer modelling and remote sensing.

Acknowledgements

We thank Joachim Ruber at the TUM limnologic station in Iffeldorf for collection and provision of parts of the CDOM samples.

Funding

A.G. was supported by the Deutsche Forschungsgemeinschaft (DFG) through the International Graduate School of Science and Engineering (IGSSE) and the TUM Laura-Bassi fund. The author's would also like to thank the Remote Sensing Technology Institute (IMF) at the German Aerospace Center (DLR) in Oberpfaffenhofen for laboratory access and equipment.

Declaration of interests: None

References

Aiken, G., 2017. Chapter 2. Fluorescence and dissolved organic matter: A chemist's perspective. In book: Aquatic organic matter fluorescence. Coble P.G., Lead J. I., Baker A., Reynolds D. M., and Spencer R. G. M. Eds.; publisher: Cambridge university press, 2014.

Asmala, E., Stedmon, C. A., Thomas, D. N., 2012. Linking CDOM spectral absorption to dissolved organic carbon concentrations and loadings in boreal estuaries. Estuarine, Coastal and Shelf Science 111 (Supplement C), 107 – 117. http://www.sciencedirect.com/science/article/pii/S027277141200234X

Ayoub, L. M., Hallock, P., Coble, P. G., Bell, S. S., 2012. MAA-like absorbing substances in Florida keys phytoplankton vary with distance from shore and CDOM: Implications for coral reefs. Journal of Experimental Marine Biology and Ecology 420 (Supplement C), 91 – 98. http://www.sciencedirect.com/-science/article/pii/S0022098112001049

Babin, M., Stramski, D., Ferrari, G. M., Claustre, H., Bricaud, A., Obolensky, G., Hoepffner, N., 2003. Variations in the light absorption coefficients of phytoplankton, nonalgal particles, and dissolved organic

matter in coastal waters around Europe. Journal of Geophysical Research: Oceans 108 (C7). https://-agupubs.onlinelibrary.wiley.com/doi/abs/10.1029/2001JC000882

Bricaud, A., Morel, A., Prieur, L., 1981. Absorption by dissolved organic matter of the sea (yellow substance) in the UV and visible domains. Limnology and Oceanography 26 (1), 43–53. https://-aslopubs.onlinelibrary.wiley.com/doi/abs/10.4319/lo.1981.26.1.0043

Coble, P. G., 1996. Characterization of marine and terrestrial DOM in seawater using excitation-emission matrix spectroscopy. Marine Chemistry 51 (4), 325 – 346. http://www.sciencedirect.com/science/article/-pii/0304420395000623

Coble, P. G., 2007. Marine Optical Biogeochemistry – The Chemistry of Ocean Color. Chemical Reviews 107 (2), 402–418, pMID: 17256912. http://dx.doi.org/10.1021/cr050350+

Coble, P. G., Castillo, C. E. D., Avril, B., 1998. Distribution and optical properties of CDOM in the Arabian Sea during the 1995 Southwest Monsoon. Deep Sea Research Part II: Topical Studies in Oceanography 45 (10), 2195 – 2223. http://www.sciencedirect.com/science/article/pii/-S096706459800068X

Coble, P. G., Lead, J., Baker, A., Reynolds, D. M., Spencer, R. G., 2014. Aquatic organic matter fluorescence. Cambridge University Press.

Dutkiewicz, S., Hickman, A. E., Jahn, O., Gregg, W. W., Mouw, C. B., Follows, M. J., 2015. Capturing optically important constituents and properties in a marine biogeochemical and ecosystem model. Biogeosciences 12 (14), 4447–4481. https://www.biogeosciences.net/12/4447/2015/

Faris, G. W., Copeland, R. A., Apr 1997. Wavelength dependence of the Raman cross section for liquid water. Appl. Opt. 36 (12), 2686–2688. http://ao.osa.org/abstract.cfm?URI=ao-36-12-2686

Fasching, C., Behounek, B., Singer, G. A., Battin, T. J., 2014. Microbial degradation of terrigenous dissolved organic matter and potential consequences for carbon cycling in brown-water streams. Scientific reports 4.

Gege, P., 2000. Gaussian model for yellow substance absorption spectra. Proc. Ocean Optics Conference

669 XV Conference, October 16-20, 2000, Monaco.
670 Gege, P., 2004. Improved method for measuring gelbstoff absorption spectra. Proc. Ocean Optics
671 Conference XVII, 25-29 Oct. 2004, Fremantle, Australia.
672 Gege, P., 2017. Chapter 2: Radiative transfer theory for inland waters. In Book *Bio-optical Modeling and*
673 *Remote Sensing of Inland Waters*, 1st Edition. Elsevier.
674 Goletz, C., Wagner, M., Grübel, A., Schmidt, W., Korf, N., Werner, P., 2011. Standardization of
675 fluorescence excitation–emission–matrices in aquatic milieu. Talanta 85 (1), 650 – 656. http://-
676 www.sciencedirect.com/science/article/pii/S0039914011003596
677 Gonçalves-Araujo, R., Rabe, B., Peeken, I., Bracher, A., 01 2018. High colored dissolved organic matter
678 (CDOM) absorption in surface waters of the central-eastern Arctic Ocean: Implications for
679 biogeochemistry and ocean color algorithms. PLOS ONE 13 (1), 1–27. https://doi.org/10.1371/-
680 journal.pone.0190838
681 Gordon, H. R., 1979. Diffuse reflectance of the ocean: the theory of its augmentation by chlorophyll a
682 fluorescence at 685 nm. Applied Optics 18 (8), 1161–1166.
683 Green, S. A., Blough, N. V., 1994. Optical absorption and fluorescence properties of chromophoric
684 dissolved organic matter in natural waters. Limnology and Oceanography 39 (8), 1903–1916.
685 Hawes, S. K., 1992. Quantum fluorescence efficiencies of marine fulvic and humic acids. Master's thesis,
686 University of South Florida.
687 Hestir, E. L., Brando, V., Campbell, G., Dekker, A., Malthus, T., 2015. The relationship between
688 dissolved organic matter absorption and dissolved organic carbon in reservoirs along a temperate to
689 tropical gradient. Remote Sensing of Environment 156 (Supplement C), 395 – 402. http://-
690 www.sciencedirect.com/science/article/pii/S0034425714003678
691 Hoge, F. E., Vodacek, A., Swift, R. N., Yungel, J. K., Blough, N. V., Oct 1995. Inherent optical
692 properties of the ocean: retrieval of the absorption coefficient of chromophoric dissolved organic matter
693 from airborne laser spectral fluorescence measurements. Appl. Opt. 34 (30), 7032–7038. http://-

694 ao.osa.org/abstract.cfm?URI=ao-34-30-7032
695 Kirk, J. T., 2011. Light and Photosynthesis in Aquatic Ecosystems, 3rd Edition. Cambridge University
696 Press.
697 Korshin, G. V., Li, C.-W., Benjamin, M. M., 1997. Monitoring the properties of natural organic matter
698 through UV spectroscopy: A consistent theory. Water Research 31 (7), 1787 – 1795. http://-
699 www.sciencedirect.com/science/article/pii/S0043135497000067
700 Kutser, T., Verpoorter, C., Paavel, B., Tranvik, L. J., 2015. Estimating lake carbon fractions from remote
701 sensing data. Remote Sensing of Environment 157 (Supplement C), 138 – 146, special Issue: Remote
702 Sensing of Inland Waters. http://www.sciencedirect.com/science/article/pii/S003442571400234X
703 Lakowicz, J. R., 2006. Principles of Fluorescence Spectroscopy, 3rd Edition. Springer.
704 Lawaetz, A. J., Stedmon, C. A., 2009. Fluorescence intensity calibration using the Raman scatter peak of
705 water. Applied spectroscopy 63 (8), 936–940.
706 Loiselle, S. A., Bracchini, L., Dattilo, A. M., Ricci, M., Tognazzi, A., Cózar, A., Rossi, C., 2009. The
707 optical characterization of chromophoric dissolved organic matter using wavelength distribution of
708 absorption spectral slopes. Limnology and Oceanography 54 (2), 590–597. https://-
709 aslopubs.onlinelibrary.wiley.com/doi/abs/10.4319/lo.2009.54.2.0590
710 MacDonald, B. C., Lvin, S. J., Patterson, H., 1997. Correction of fluorescence inner filter effects and the
711 partitioning of pyrene to dissolved organic carbon. Analytica Chimica Acta 338 (1), 155 – 162. http://-
712 www.sciencedirect.com/science/article/pii/S0003267096003066
713 Massicotte, P., Markager, S., 2016. Using a Gaussian decomposition approach to model absorption
714 spectra of chromophoric dissolved organic matter. Marine Chemistry 180, 24–32.
715 Murphy, K. R., Bro, R., Stedmon, C. A., 2014. Chemometric analysis of organic matter fluorescence.
716 Aquatic organic matter fluorescence, 339–375.
717 Murphy, K. R., Stedmon, C. A., Graeber, D., Bro, R., 2013. Fluorescence spectroscopy and multi-way
718 techniques. PARAFAC. Analytical Methods 5 (23), 6557–6566.

719 Nieke, B., Reuter, R., Heuermann, R., Wang, H., Babin, M., Therriault, J., 1997. Light absorption and
720 fluorescence properties of chromophoric dissolved organic matter (CDOM), in the St. Lawrence Estuary
721 (Case 2 waters). Continental Shelf Research 17 (3), 235 – 252. //www.sciencedirect.com/science/article/-
722 pii/S0278434396000349
723 NIST, 1994. Certificate of analysis for standard reference material 936a - quinine sulfate dihydrate. Tech.
724 rep., National Institute of Standards and Technology.
725 Organelli, E., Bricaud, A., Antoine, D., Matsuoka, A., 2014. Seasonal dynamics of light absorption by
726 chromophoric dissolved organic matter (CDOM) in the NW Mediterranean Sea (BOUSSOLE site). Deep
727 Sea Research Part I: Oceanographic Research Papers 91, 72 – 85. http://www.sciencedirect.com/science/-
728 article/pii/S0967063714000764
729 Palmer, S. C., Pelevin, V. V., Goncharenko, I., KovÃ¡cs, A. W., Zlinszky, A., Présing, M., Horváth, H.,
730 Nicolás-Perea, V., Balzter, H., Tóth, V. R., 2013. Ultraviolet fluorescence LiDAR (UFL) as a
731 measurement tool for water quality parameters in turbid lake conditions. Remote Sensing 5 (9), 4405–
732 4422. http://www.mdpi.com/2072-4292/5/9/4405
733 Parlanti, E., Wörz, K., Geoffroy, L., Lamotte, M., 2000. Dissolved organic matter fluorescence
734 spectroscopy as a tool to estimate biological activity in a coastal zone submitted to anthropogenic inputs.
735 Organic Geochemistry 31 (12), 1765 – 1781. http://www.sciencedirect.com/science/article/pii/-
736 S0146638000001248
737 Pozdnyakov, D., Lyaskovsky, A., Pettersson, H. G. L., 2002. Numerical modelling of transspectral
738 processes in natural waters: Implications for remote sensing. International Journal of Remote Sensing
739 23 (8), 1581–1607. https://doi.org/10.1080/014311601170735
740 Röttgers, R., McKee, D., Utschig, C., Oct 2014. Temperature and salinity correction coefficients for light
741 absorption by water in the visible to infrared spectral region. Opt. Express 22 (21), 25093–25108. http://-
742 www.opticsexpress.org/abstract.cfm?URI=oe-22-21-25093
743 Schwarz, J. N., Kowalczuk, P., Kaczmarek, S., Cota, G. F., Mitchell, B. G., Kahru, M., Chavez, F. P.,

744 Cunningham, A., McKee, D., Gege, P., et al., 2002. Two models for absorption by coloured dissolved
745 organic matter (CDOM). Oceanologia 44 (2).
746 Sipelgas, L., Arst, H., Kallio, K., Erm, A., Oja, P., Soomere, T., 2003. Optical properties of dissolved
747 organic matter in Finnish and Estonian lakes. Hydrology Research 34 (4), 361–386.
748 Spencer, R. G. M., Aiken, G. R., Butler, K. D., Dornblaser, M. M., Striegl, R. G., Hernes, P. J., 2009.
749 Utilizing chromophoric dissolved organic matter measurements to derive export and reactivity of
750 dissolved organic carbon exported to the Arctic Ocean: A case study of the Yukon River, Alaska.
751 Geophysical Research Letters 36 (6), n/a–n/a, l06401. http://dx.doi.org/10.1029/2008GL036831
752 Spencer, R. G. M., Butler, K. D., Aiken, G. R., 2012. Dissolved organic carbon and chromophoric
753 dissolved organic matter properties of rivers in the USA. Journal of Geophysical Research:
754 Biogeosciences 117 (G3), n/a–n/a, g03001. http://dx.doi.org/10.1029/2011JG001928
755 Stedmon, C. A., Markager, S., 2005. Tracing the production and degradation of autochthonous fractions
756 of dissolved organic matter by fluorescence analysis. Limnology and Oceanography 50 (5), 1415–1426.
757 http://dx.doi.org/10.4319/lo.2005.50.5.1415
758 Stedmon, C. A., Markager, S., Bro, R., 2003. Tracing dissolved organic matter in aquatic environments
759 using a new approach to fluorescence spectroscopy. Marine Chemistry 82 (3), 239 – 254. http://-
760 www.sciencedirect.com/science/article/pii/S0304420303000720
761 Stedmon, C. A., Seredynska-Sobecka, B., Boe-Hansen, R., Tallec, N. L., Waul, C. K., Arvin, E., 2011. A
762 potential approach for monitoring drinking water quality from groundwater systems using organic matter
763 fluorescence as an early warning for contamination events. Water Research 45 (18), 6030 – 6038. http://-
764 www.sciencedirect.com/science/article/pii/S0043135411005203
765 Thrane, J.-E., Hessen, D. O., Andersen, T., Sep 2014. The absorption of light in lakes: Negative impact of
766 dissolved organic carbon on primary productivity. Ecosystems 17 (6), 1040–1052. https://doi.org/-
767 10.1007/s10021-014-9776-2
768 Vantrepotte, V., Danhiez, F.-P., Loisel, H., Ouillon, S., Mériaux, X., Cauvin, A., Dessailly, D., Jan 2015.

769 CDOM-DOC relationship in contrasted coastal waters: implication for DOC retrieval from ocean color
770 remote sensing observation. Opt. Express 23 (1), 33–54. http://www.opticsexpress.org/-
771 abstract.cfm?URI=oe-23-1-33
772 Velapoldi, R. A., Mielenz, K. D., 1980. A fluorescence standard reference material: quinine sulfate
773 dihydrate. Vol. 260. Department of Commerce, National Bureau of Standards.
774 Velapoldi, R. A., Tønnesen, H. H., 2004. Corrected emission spectra and quantum yields for a series of
775 fluorescent compounds in the visible spectral region. Journal of fluorescence 14 (4), 465–472.
776 Vodacek, A., Hogel, F. E., Swift, R. N., Yungel, J. K., Peltzer, E. T., Blough, N. V., 1995. The use of in
777 situ and airborne fluorescence measurements to determine UV absorption coefficients and DOC
778 concentrations in surface waters. Limnology and Oceanography 40 (2), 411–415. https://-
779 aslopubs.onlinelibrary.wiley.com/doi/abs/10.4319/lo.1995.40.2.0411
780 Williamson, C. E., Overholt, E. P., Pilla, R. M., Leach, T. H., Brentrup, J. A., Knoll, L. B., Mette, E. M.,
781 Moeller, R. E., 2015. Ecological consequences of long-term browning in lakes. Scientific reports 5,
782 18666.
783 Würth, C., Grabolle, M., Pauli, J., Spieles, M., Resch-Genger, U., 2013. Relative and absolute
784 determination of fluorescence quantum yields of transparent samples. Nature protocols 8 (8), 1535.
785 Zepp, R. G., Schlotzhauer, P. F., 1981. Comparison of photochemical behavior of various humic
786 substances in water: III. Spectroscopic properties of humic substances. Chemosphere 10 (5), 479 – 486.
787 http://www.sciencedirect.com/science/article/pii/004565358190148X
788

A.3 Publication III

Göritz A., Berger S.A., Gege P., Grossart H.P., Nejstgaard J.C., Riedel S., Röttgers R., Utschig C.
Retrieval of Water Constituents from Hyperspectral In-Situ Measurements under Variable Cloud Cover – A Case Study at Lake Stechlin (Germany)
Remote Sensing 2018, Vol. 10, Issue 2, 181.

This research article was published in *Remote Sensing (MDPI)*. For the final version and updates, please refer to `https://doi.org/10.3390/rs10020181`.

remote sensing

MDPI

Article

Retrieval of Water Constituents from Hyperspectral In-Situ Measurements under Variable Cloud Cover—A Case Study at Lake Stechlin (Germany)

Anna Göritz [1,2,*], Stella A. Berger [3], Peter Gege [2], Hans-Peter Grossart [3,4], Jens C. Nejstgaard [3], Sebastian Riedel [2,5], Rüdiger Röttgers [6] and Christian Utschig [6]

1 Department of Civil, Geo and Environmental Engineering, Remote Sensing Technology, Technical University of Munich (TUM), Arcisstr. 21, D-80333 München, Germany
2 German Aerospace Center, Remote Sensing Technology Institute, Münchner Str. 20, Oberpfaffenhofen, D-82234 Weßling, Germany; peter.gege@dlr.de (P.G.); Riedel@geographie.uni-kiel.de (S.R.)
3 Department of Experimental Limnology, Leibniz-Institute of Freshwater Ecology and Inland Fisheries, Alte Fischerhütte 2, D-16775 Stechlin, Germany; berger@igb-berlin.de (S.A.B.); hgrossart@igb-berlin.de (H.-P.G.); nejstgaard@igb-berlin.de (J.C.N.)
4 Institute of Biochemistry and Biology, Potsdam University, Maulbeerallee 2, D-14476 Potsdam, Germany
5 Earth Observation and Modelling, Department of Geography, Kiel University, Ludewig-Meyn-Str. 14, D-24098 Kiel, Germany
6 Helmholtz-Zentrum Geesthacht, Center for Materials and Coastal Research, Institute for Coastal Research, Max Planck Str. 1, D-21502 Geesthacht, Germany; rroettgers@hzg.de (R.R.); christian.utschig@kws.com (C.U.)
* Correspondence: anna.goeritz@tum.de; Tel.: +49-8153-28-1594

Received: 6 November 2017; Accepted: 19 January 2018; Published: 26 January 2018

Abstract: Remote sensing and field spectroscopy of natural waters is typically performed under clear skies, low wind speeds and low solar zenith angles. Such measurements can also be made, in principle, under clouds and mixed skies using airborne or in-situ measurements; however, variable illumination conditions pose a challenge to data analysis. In the present case study, we evaluated the inversion of hyperspectral in-situ measurements for water constituent retrieval acquired under variable cloud cover. First, we studied the retrieval of Chlorophyll-*a* (Chl-*a*) concentration and colored dissolved organic matter (CDOM) absorption from in-water irradiance measurements. Then, we evaluated the errors in the retrievals of the concentration of total suspended matter (TSM), Chl-*a* and the absorption coefficient of CDOM from above-water reflectance measurements due to highly variable reflections at the water surface. In order to approximate cloud reflections, we extended a recent three-component surface reflectance model for cloudless atmospheres by a constant offset and compared different surface reflectance correction procedures. Our findings suggest that in-water irradiance measurements may be used for the analysis of absorbing compounds even under highly variable weather conditions. The extended surface reflectance model proved to contribute to the analysis of above-water reflectance measurements with respect to Chl-*a* and TSM. Results indicate the potential of this approach for all-weather monitoring.

Keywords: remote sensing; inland water; hyperspectral measurements; in-situ; cloud; surface reflection; inversion; bio-optical modeling

1. Introduction

Recent advances in sensor technology and progress in algorithm development open new perspectives for inland water remote sensing. Along with an increasing need for water quality monitoring and holistic views on globally distributed inland water ecosystems, remote sensing

applications are becoming an important complementary approach to classic monitoring routines [1–4]. Recent publications cover lake and coastal water observations on a wide spectrum of platforms, ranging from space- and airborne to above-water measurements [4–8]. Major advantages of satellite monitoring are the broad coverage and high repetition rates (e.g., 5 days revisit time for recently launched Sentinel-2 twin satellite mission), which allow for time series studies on a global scale. Automated measurement systems, in turn, which are mounted on jetties, fixed platforms, buoys or ships can provide valuable information about short-term or local changes of water quality parameters and can serve for the calibration and validation of satellite and airborne remote sensing data [9–12].

While spaceborne optical remote sensing requires mostly clear sky conditions, airborne and in-situ (above- and in-water) measurements can, in principle, be performed on cloudy days as well. A major challenge for this kind of application is that retrieval algorithms need to account for the variability in the illumination conditions. Changes in illumination can lead to intense and highly variable water surface reflections, which depend on several factors such as viewing geometry, sun position, angular distribution of the sky radiance (L_{sky}), and on the slope distribution of the surface (waves) [13]. Since reflections of direct sunlight (sun glint) and clouds can easily be an order of magnitude higher than the water leaving radiance itself [14,15], their effect needs to be minimized during data acquisition or corrected very accurately during data analysis.

Minimization of sun glint is possible, for instance, when choosing an observation geometry that reduces the probability of specular reflection of the sun disk by accounting for the slope distribution of waves [16], or by combining the usage of a polarizer and an optimized viewing geometry [17]. However, such minimization is not always feasible (e.g., due to a fixed viewing geometry on a satellite/aircraft), nor always desirable, (e.g., increased path length in shallow waters for bottom substrate classification or anisotropy effects for calibration/validation of remote sensing data [18]). With respect to clouds, measurement protocols for reflection minimization do not exist and suitable procedures are difficult to design.

Recently, a physically based spectral model (3C) was published, which enables correction of remote sensing data and field measurements with respect to surface reflectance at clear sky conditions [19]. It does not require accompanying L_{sky} measurements and builds on a simple model for cloudless maritime atmospheres that separates the downwelling irradiance into three spectrally different components [20]. The 3C model has been successfully applied for sun glint correction in airborne and satellite imagery [21,22], and it has been proven to enable accurate compensation of errors that remain after correction of reflectance with L_{sky} measurements, even for mixed and overcast sky conditions [15].

In the present case study, we investigated the potential of water constituent retrieval from hyperspectral in-situ measurements acquired under variable cloud cover without additional L_{sky} measurements.

First, in-water downwelling irradiance measurements were analyzed with a focus on the determination of Chlorophyll-*a* (Chl-*a*) concentration and colored dissolved organic matter (CDOM) absorption. Here, the 3C model was applied to handle the so-called wave focusing effect [23,24], i.e., the variability of direct and diffuse components induced by the waves [25]. Since the impact of clouds on downwelling irradiance is spectrally approximately neutral in the visible [26,27], it was simulated by dimming the direct and diffuse components of irradiance. The parameters of the 3C model account for this dimming. Thus, clouds were not treated separately in this part of the analysis.

For above-water measurements, clouds are of particular relevance as they can induce a very large offset in the reflectance. Therefore, in the second part of this study, the impact of reflections at the water surface on the retrieval of Chl-*a* concentration, CDOM absorption at 440 nm and total suspended matter (TSM) concentration from above-water reflectance measurements was examined. To enable separate modeling of cloud reflections, the 3C model was extended by a constant offset. We examined which of the parameters of the resulting four component (4C) model need to be treated as fit parameters during inversion in order to mimic the surface reflectance. Water constituents were

determined by coupling the 4C model with a bio-optical model of the water body [28,29] and fitting the relevant unknown parameters of both models together. Results were compared against data from laboratory analysis of water samples and from a submersible spectrofluorometer.

2. Materials and Methods

2.1. Overview of Measurements and Methodology in This Study

The aim of this study was to evaluate water constituent retrieval from hyperspectral above-water radiance reflectance and in-water irradiance measurements under highly variable illumination conditions. Figure 1 gives an overview of all measurements and derived parameters (first row). They are explained in more detail in the following Sections 2.3 and 2.4. The second row of Figure 1 summarizes the analysis of in-water irradiance spectra which were recorded at different depths (z) and analyzed in two approaches for the determination of CDOM absorption at 440 nm, and Chl-*a* concentration (see Sections 2.6.1 and 3.2). The third row in Figure 1 illustrates the retrieval of CDOM absorption at 440 nm and Chl-*a* and TSM concentration from above-water radiance reflectance measurements. Here, different surface reflectance correction procedures (A)-(K) were tested and the best performing approach was selected for water constituent retrieval (see Sections 2.6.2 and 3.3). The inversion retrieval results were compared to results from water sample analysis. Models applied during the inversion analysis are described in Section 2.5.

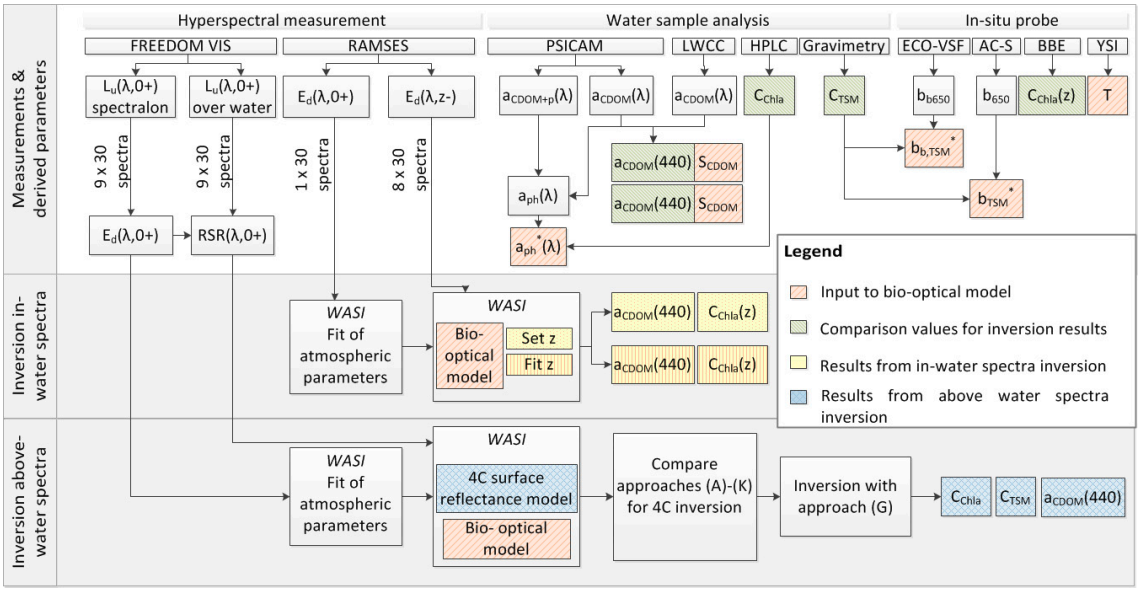

Figure 1. Flow chart illustrating the set of measurements and methodology applied in this study. All abbreviations and acronyms are defined in Sections 2.3–2.6, and are listed at the end of the paper.

2.2. Test Site and Measurement Conditions

During a field campaign on 31 May 2016, an extensive data set of in-situ measurements (above-water and in-water hyperspectral measurements as well as water samples for laboratory analysis) was collected at the deepest point of Lake Stechlin (shortest distance to shore is about 400 m). The lake is located in the federal state of Brandenburg, North-East Germany (53°10′N, 13°02′E) at approximately 60 m above sea level [30]. It is weakly connected to Lake Nehmitz via two channels, which earlier served as in- and outflow channels in a cooling circuit for a nuclear power plant (KKW Rheinsberg—active from 1961 to 1990). Lake Stechlin is surrounded by beech and pine forests and has an area of approximately 4.12 km^2. It is almost exclusively ground water fed and has a maximum

depth of 69.5 m. Lake Stechlin is a hard water lake and has a meso-oligotrophic status. Physical, chemical and biological factors have been intensively studied since the 1960s [31].

Sky conditions were highly variable during the period of hyperspectral measurements (Figure 2): continuous cloud layers of variable thickness covered the sky while the first spectra were recorded. These layers diminished until sun began to break through the clouds. During the subsequent measurements, more direct sunlight fell through gaps between clouds, until conditions right above the test site were mostly sunny (for more details, see Section 3.3).

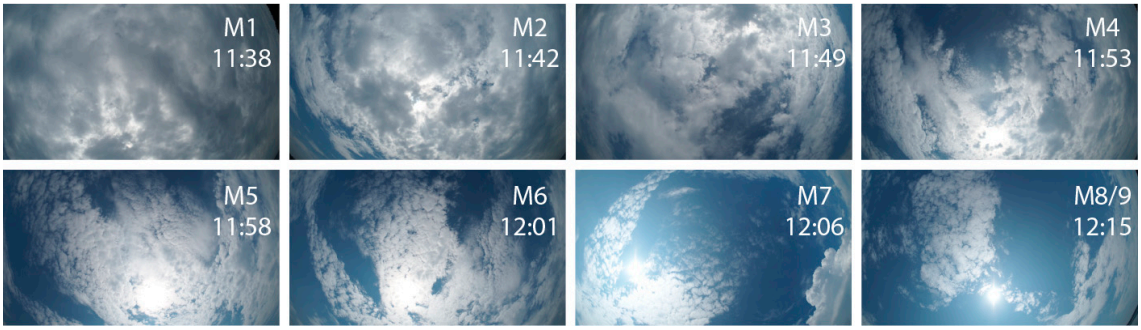

Figure 2. Photographs taken in the direction of the sun illustrating the sky conditions during the times when hyperspectral sets of measurements (M1–M9) were recorded.

2.3. Water Constituents and Vertical Profiles

Water samples were taken in parallel to hyperspectral measurements from below the water surface. The spectral light absorption coefficient (360–700 nm, in 2-nm steps) of the sample including dissolved and particulate matter without the contribution of pure water, $a_{CDOM+p}(\lambda)$, was determined from triplicate measurements with a point-source integrating-cavity absorption meter (PSICAM) [32]. The PSICAM was calibrated before sample measurements using a colored dye solution; temperature effects from pure water absorption were corrected [33]. In order to determine the absorption coefficient of colored dissolved organic matter, $a_{CDOM}(\lambda)$, the sample water was filtered through a 0.2-µm membrane filter (GSWP, Millipore) and measured both in the PSICAM and with a 2-m path length liquid waveguide capillary cell (LWCC; WPI Inc., Sarasota, FL, USA) setup [34]. Spectral absorbance values were converted to absorption coefficients according to Beer's law. Then, the CDOM spectral slope parameter S_{CDOM} (nm^{-1}) was derived from an exponential fit to the absorption coefficient spectrum in a wavelength range of 360–520 nm (symmetric around 440 nm):

$$a_{CDOM}(\lambda) = a_{CDOM}(440) \cdot e^{-S_{CDOM}(\lambda - 440)}. \quad (1)$$

In addition to absorption, total suspended matter concentration, C_{TSM}, was determined in four sets of four filters following the approach of Röttgers et al. [35] by filtering different volumes (0.5, 1, 1.5 and 2 l) of lake water through pre-combusted and weighted GF/F filters (Whatman). After drying the filters at 65 °C (1 set of filters) and 105 °C (3 set of filters), their dry weight was measured and filter weights of the empty filters were subtracted. The final TSM concentration was derived from linear regression of the masses versus the respective volumes.

Beam attenuation was measured using an in-situ spectrophotometer (Wetlabs AC-S), additionally allowing to determine the total scattering coefficient at 650 nm, $b(650)$. The backscattering coefficient, $b_b(650)$, was recorded using an in-situ backscatter meter (Wetlabs ECO-VSF). The specific backscattering coefficient of TSM $b_b^*(650)$ was calculated by normalization to the total suspended matter concentration:

$$b_{b,TSM}^* = \frac{1}{C_{TSM}} \cdot b_b(650). \quad (2)$$

Analogously, the specific scattering coefficient b^*_{TSM} was calculated by normalization of $b(650)$ to the total suspended matter concentration.

For determination of Chl-*a* concentration, C_{Chla}, 1 L of lake water was filtered under low ambient room light onto GF/F filters (Whatman) and stored in liquid nitrogen (in the dark). After transportation to a different laboratory, pigments were extracted from filters (triplicates) in 5 mL of 90% acetone (24 h) and the extract was subsequently analyzed by high performance liquid chromatography (HPLC) [36].

Particulate absorption ($a_p(\lambda)$) was calculated as the difference of $a_{CDOM+p}(\lambda)$ and $a_{CDOM}(\lambda)$ as measured with PSICAM. Due to high phytoplankton biomass in the lake water, this absorption spectrum derived from water sample measurements exhibited spectral features similar to pure phytoplankton culture absorption. Therefore, the spectrum was normalized to the Chl-*a* concentration in (mg m^{-3}):

$$a^*_{ph}(\lambda) = \frac{1}{C_{Chla}} \cdot a_p(\lambda), \quad (3)$$

and was added to the spectral library of the inversion software as a specific phytoplankton absorption spectrum $a^*_{ph}(\lambda)$ (m^2 mg^{-1}) for further chlorophyll retrieval.

To determine the phytoplankton community composition, untreated (live) water samples taken from about 0.5 m depth were analyzed in a digital imaging flow-cytometer for particle analysis (FlowCam, Model VS, Fluid Imaging Technologies, Scarborough, ME, USA), immediately after returning to the shore-side lab (within 30 min after sampling). For this purpose, 4× and 10× objectives were used in combination with a 300 µm and 100 µm flow-cell, respectively, with the instrument in automatic imaging mode [37], to account for all particle sizes from 3–300 µm. Image collages were post-analyzed to separate the dominant taxonomic phytoplankton groups and to calculate their biomasses.

Abiotic and biotic parameters were measured at 0.5-m intervals from the surface to the deepest point of the lake. Abiotic variables were measured with a calibrated multi-parameter probe YSI 6600 (YSI Inc., Yellow Springs, OH, USA), that included sensors for temperature (sensor YSI6560), conductivity (YSI6560), pH (YSI6579), and dissolved oxygen concentration (YSI6150). Biotic variables such as phytoplankton biomass were estimated with a submersible spectrofluorometer (FluoroProbe; bbe Moldaenke; Schwentinental, Germany). Here, total Chl-*a* concentration was calculated as the sum of four algal pigment groups (cyanobacteria, chlorophytes, cryptophytes and "diatoms", the latter including all brown pigmented groups of diatoms, chrysophytes, haptophytes and dinoflagellates), measured by the FluoroProbe. The total Chl-*a* concentration served as comparison values for Chl-*a* concentration retrieval from in-water downwelling irradiance spectra (see Sections 3.2 and 3.3).

2.4. Hyperspectral Measurements

Downwelling irradiance $E_d(\lambda)$, under water was recorded with a hyperspectral radiometer (RAMSES ACC-VIS, TriOS GmbH, Rastede, Germany; spectral sampling interval 3.3 nm at 320–950 nm) [38]. Spectra were resampled on a 1 nm spaced grid by cubic interpolation. In order to estimate sensor response, both rectangular- and Gaussian-shaped resampling with varying Full Width Half Maximum (FWHM) was applied to modeled $E_d(\lambda)$, in order to simulate data retrieved with the RAMSES sensor. Best matches to spectral signatures in measured irradiance spectra were achieved with a Gaussian-shaped resampling of 8 nm FWHM.

The actual depth of the sensor's light collector was determined with a measuring tape and a step counter. Although the step counter, in principle, allows to measure length quite accurately (~±2 cm at calm conditions), leveling of the counter had to be estimated. Therefore, a systematic uncertainty of the measured depth in the order of 5–10 cm is assumed. In-water hyperspectral measurements were performed at eight different depths within the first 4 m below water surface.

For above-water measurements, a FREEDOM VIS FSV-305 spectrometer (Ibsen Photonics Inc., Farum, Denmark; 0.5 nm spectral sampling interval at 360–830 nm, field-of-view with optic ~4.5°) and a 10% reflectance standard (Labsphere Inc., North Sutton, NH, USA) were used [39,40]. In nine sets of

measurements, first upwelling radiance above the reflectance target (30 spectra each), and subsequently upwelling radiance above water (30 spectra each) was measured in nadir geometry. Raw data was converted to radiance after dark current subtraction by applying sensor response and nonlinearity correction as measured in the laboratory. Downwelling irradiance was calculated by multiplying radiance spectra recorded over the reflectance target with a factor of π and considering the spectral calibration factors of the 10% standard. For simplification, the two types of field spectrometric setups are referred to as RAMSES and FREEDOM VIS instruments. In the following, the symbols plus (+) and minus (−) are used as superscripts to distinguish between above- and in-water measurements, respectively.

Radiance reflectance above water (sometimes also referred to as Remote Sensing Ratio (RSR) [41]) was calculated from FREEDOM VIS spectra according to:

$$RSR^{+}(\lambda) = \frac{L_u^{+}(\lambda)}{E_d^{+}(\lambda)}. \quad (4)$$

It should be noted that upwelling radiance, L_u, contains both water leaving radiance and sky radiance due to reflection on the lake surface. For each measurement series, the sun zenith angle was calculated using the *Python PyEphem* library [42].

2.5. Models for Hyperspectral Data Analysis

2.5.1. Downwelling Irradiance above Water

Downwelling irradiance above water, $E_d^{+}(\lambda)$, was modeled using the model of Gege [25], which builds on the approach of Gregg and Carder and Bird and Riordan [20,25,43] for clear sky conditions [20,25,43]. It distinguishes between the direct component of downwelling irradiance (E_{dd}), and two diffuse components arising from Rayleigh scattering at molecules (E_{dsr}), and from Mie scattering at aerosols (E_{dsa}). The model expresses E_{dd}, E_{dsr} and E_{dsa} as products of the extraterrestrial solar irradiance and a number of transmission functions with the scale height of ozone, H_{oz}, the Ångström exponent of aerosol scattering, α, the turbidity coefficient β (aerosol optical thickness at 550 nm), and the scale height of precipitable water in the atmosphere, WV, as the most relevant parameters that are frequently unknown. Shadowing effects, as might be introduced by clouds or obstacles, are accounted for by scaling each component with a weight which represents the actual intensity relative to clear and unobscured sky:

$$E_d^{+}(\lambda) = f_{dd} \cdot E_{dd}(\lambda) + f_{dsr} \cdot E_{dsr}(\lambda) + f_{dsa} \cdot E_{dsa}(\lambda). \quad (5)$$

f_{dd} is the relative intensity of E_{dd}, f_{dsr} that of E_{dsr}, and f_{dsa} that of E_{dsa}. All fs are wavelength independent; they are unity for clear and unobscured sky. The fs allow all changes of $E_d^{+}(\lambda)$ to be modeled that are induced by spectrally neutral modifications of E_{dd}, E_{dsr} or E_{dsa} by transmission, scattering or reflection at 'white' targets such as clouds. During inverse modeling, the fs are treated as fit parameters, while the spectra $E_i(\lambda)$ are modeled using the parameterization of Gregg and Carder [20], and the spectral database of atmospheric components of Gege [44].

2.5.2. Downwelling Irradiance in Water

The downwelling irradiance in water, $E_d^{-}(\lambda, z)$, was modeled using the model of Gege [25]. It assumes that the downwelling irradiance just below the water surface (at depth $z = 0$) can be described by Equation (5) with a common factor f_{ds} for the two diffuse components ($f_{ds} = f_{dsr} = f_{dsa}$) that allows to combine these as $E_{ds}(\lambda) = E_{dsr}(\lambda) + E_{dsa}(\lambda)$. Values for the f_{dd} and f_{ds} parameters are usually highly variable for an undulated water surface [45], and not known in practice. At depth z, $E_{dd}(\lambda)$ is attenuated by $\exp\{-[a(\lambda) + b_b(\lambda)] \cdot z / cos\theta'_{sun}\}$ and $E_{ds}(\lambda)$ is attenuated by $\exp\{-[a(\lambda) + b_b(\lambda)] \cdot z \cdot l_{ds}\}$, with θ'_{sun} the sun zenith angle in water and $l_{ds} = 1.1156 + 0.5504 \cdot (1 - \cos\theta'_{sun})$

the average path length of diffuse radiation relative to sensor depth. The absorption and backscattering coefficients were parameterized in this study as follows:

$$a(\lambda) = a_w(\lambda) + C_{Chla} \cdot a^*_{ph}(\lambda) + a_{CDOM}(440) \cdot e^{-S_{CDOM} \cdot (\lambda - 440)}, \quad (6)$$

$$b_b(\lambda) = b_{b,w}(\lambda) + C_{TSM} \cdot b^*_{b,TSM}(\lambda). \quad (7)$$

In these equations, $a_w(\lambda)$ and $b_{b,w}(\lambda)$ are the absorption and backscattering coefficients of pure water, respectively. Absorption of phytoplankton is expressed as a product of the Chl-*a* concentration, C_{Chla}, and the specific phytoplankton absorption coefficient, $a^*_{ph}(\lambda)$. CDOM absorption is approximated as an exponential function, as usual (see studies by Bricaud et al. and Carder et al. [46,47]). In this description, the slope S_{CDOM} is related to the composition, and the absorption coefficient at 440 nm, $a_{CDOM}(440)$, is taken as a proxy for the concentration. Backscattering of total suspended matter (including phytoplankton) is treated as a product of TSM concentration, C_{TSM}, and a specific backscattering coefficient, $b^*_{b,TSM}(\lambda)$. Since $b^*_{b,TSM}(\lambda)$ is weakly dependent on wavelength in coastal and inland waters [48,49], and no information about its wavelength dependency was available for Lake Stechlin, a constant value derived from in-situ measurements was used (see Section 3.1).

It was shown by Gege [25] that this separate treatment of direct and diffuse components allows the diffuse attenuation coefficient, $K_d(\lambda)$, which is an apparent optical property describing the depth change of $E_d^-(\lambda, z)$, to be replaced with the inherent optical property $[a(\lambda) + b_b(\lambda)]$. The model has been validated against Hydrolight and field measurements. It has been implemented into the public domain software *Water Colour Simulator* (WASI) [50], which was used for hyperspectral data analysis in this study. In contrast to Hydrolight, WASI can be used for inversion. To the authors' best knowledge, this is the only model that can handle the high variability of $E_d^-(\lambda, z)$ measurements induced by wave focusing. Inverse modeling allows the derivation of the sensor depth z, the concentration of phytoplankton and the absorption coefficient of CDOM if f_{dd} and f_{ds} are treated as fit parameters together with z, C_{Chla} and $a_{CDOM}(440)$ [44,51].

2.5.3. Reflections at the Water Surface

For clear sky conditions, light reflected at the water surface originates from direct sunlight and diffuse sky light. The spectral radiance of these components can be described well by the three components (3C) $E_{dd}(\lambda)$, $E_{dsr}(\lambda)$ and $E_{dsa}(\lambda)$ of Equation (5). If g_{dd}, g_{dsr} and g_{dsa} denote the respective reflection factors, the sky radiance reflected from the water surface towards a sensor can be written similar to Equation (5) as [19]:

$$L_{sky}(\lambda) = g_{dd} \cdot E_{dd}(\lambda) + g_{dsr} \cdot E_{dsr}(\lambda) + g_{dsa} \cdot E_{dsa}(\lambda). \quad (8)$$

For the hypothetical case of a uniform sky, a plane water surface and a viewing direction which avoids specular reflection of the sun disk, $g_{dd} = 0$ and $g_{dsr} = g_{dsa} = 1/\pi = 0.32\ \mathrm{sr}^{-1}$. A changing water surface can cause rapid variation of the g_i while the $E_i(\lambda)$ remain constant. The resulting variability of the g_i can be accounted for during inverse modeling by treating them as fit parameters, while the spectra $E_i(\lambda)$ are modeled as described in Section 2.5.1. It was shown that the 3C model is well-suited for correcting field measurements for sun and sky reflections [15].

For overcast sky, the reflected clouds induce an offset to reflectance measurements which is spectrally almost neutral in the visible wavelength range [27]. Reflections at the water surface are thus parameterized by the following four component (4C) surface reflectance model:

$$R_{surf}(\lambda) = \frac{L_{sky}(\lambda)}{E_d(\lambda)} + d_r, \quad (9)$$

with d_r denoting a spectrally constant cloud offset.

2.5.4. Remote Sensing Reflectance

For measurements above water, the water leaving radiance, $L_w(\lambda)$, bears all information about the water body. The ratio of water leaving radiance to downwelling irradiance is called remote sensing reflectance, $R_{rs}(\lambda)$. It is related to subsurface reflectance $r_{rs}^-(\lambda)$ as follows [52,53]:

$$R_{rs}(\lambda) = \frac{\zeta \cdot r_{rs}^-(\lambda)}{1 - \Gamma \cdot r_{rs}^-(\lambda)}, \tag{10}$$

where ζ is the water-to-air radiance divergence factor ($\approx$0.52), and the denominator with $\Gamma \approx 1.6$ accounts for the effects of internal reflection from water to air. In our study, the parameters ζ and Γ are parameterized as described by Albert and Gege [54]. $r_{rs}^-(\lambda)$ was calculated using the bio-optical model of Albert [28,29], which has been derived using Hydrolight simulations. In this semi-analytical model, the absorption and backscattering coefficients of the water body are parameterized using Equations (6) and (7). A similar $r_{rs}^-(\lambda)$ model has been developed by Lee et al. [53,55], but Albert's model additionally accounts for the sun zenith angle and the viewing angle, and it covers a wider range of environmental parameters, including most of the high concentrations of water constituents as observed in inland waters. More details on the applied models and a comparison with the models and parameter ranges of Lee et al. [53,55] can be found in Gege [56].

2.6. Water Constituent Retrieval

2.6.1. Water Constituent Retrieval from In-Water Irradiance

Inverse modeling of downwelling in-water irradiance measurements was realized with the *Water Colour Simulator* software (WASI) [50]. First, downwelling irradiance measurements above water were fitted using the $E_d^+(\lambda)$ model described in Section 2.5.1, in order to derive the atmospheric parameters α, β, H_{oz} and WV [20,25,43]. These parameters were then kept constant for further in-water irradiance modeling. For water-constituent retrieval, in-water irradiance measurements were analyzed using the $E_d^-(\lambda, z)$ model described in Section 2.5.2. In the fit procedure, identical start values of fit parameters within each measurement series were selected. As parameters of the bio-optical model, S_{CDOM}, C_{TSM}, and $b_{b,TSM}^*(\lambda)$, (compare Equations (6) and (7)), were kept constant to values derived from laboratory analysis of water samples. Phytoplankton was modeled using $a_{ph}^*(\lambda)$ derived from PSICAM measurements (see Section 2.3). Water temperature, T, was set to measured values for each depth.

Two inversion approaches were compared: First, only C_{Chla}, $a_{CDOM}(440)$, f_{dd} and f_{ds} were chosen as fit parameters (start parameters were taken from water samples analysis). In the second run, sensor depth z was added to the set of fit parameters.

2.6.2. Water Constituent Retrieval from above-Water Radiance Reflectance

For inversion of above-water radiance reflectance measurements $RSR^+(\lambda)$, a combined model for the contributions from the water body, $R_{rs}(\lambda)$, and the water surface, $R_{surf}(\lambda)$, was used:

$$RSR^+(\lambda) = R_{rs}(\lambda) + R_{surf}(\lambda). \tag{11}$$

$R_{rs}(\lambda)$ was calculated as described in Section 2.5.4 based on the bio-optical model of Albert for optically deep water [28,29]. Similar to the analysis of in-water measurements, $b_{b,TSM}^*$ and S_{CDOM} were treated as constant and set to values derived from in-situ measurements and laboratory analysis. Also, the $a_{ph}^*(\lambda)$ spectrum as derived from PSICAM measurements was used (see Section 2.3). C_{Chla}, C_{TSM} and $a_{CDOM}(440)$ were treated as fit parameters during inverse modeling.

The light reflected at the water surface is the most critical component for measurements under variable cloud cover. Its reflectance $R_{surf}(\lambda)$ was parameterized using the 4C model (Equation (9)). Different combinations of the clear sky parameters g_{dd}, g_{dsr} and g_{dsa} and the cloud offset d_r were tested to minimize the number of fit parameters for reflections at the water surface.

After retrieval of atmospheric parameters from the respective $E_d^+(\lambda)$-spectra (analogue to Section 2.6.1), $RSR^+(\lambda)$ was fitted to the measured radiance reflectance spectra using a least-squares-fit. In order to identify the best-suited set of fit parameters, inversion was performed in various approaches representing different sets of variables for modeling the surface reflectance $R_{surf}(\lambda)$ (see Section 3.3). Start parameters per measurement series were determined by pre-fitting the first spectrum of the corresponding series. The average residuum of the least-squares-fit was normalized to the maximum reflectance of the series and taken as an indicator for spectral matching of the respective approach. Finally, the best approach in terms of smallest number of fit parameters, spectral matching and lowest variance in retrieved water constituents was determined, and retrieved water constituents were compared against results from water sample analysis.

3. Results and Discussion

3.1. Water Constituents and Phytoplankton Community

Results from water analytics served as a comparison to values retrieved from hyperspectral data and are summarized in Table 1. Exponential fits to spectral absorption of CDOM, measured both with the PSICAM and LWCC setup, resulted in slope values S_{CDOM} of 0.017 ± 0.002 nm^{-1}. The corresponding absorption values (at 440 nm) are 0.21 ± 0.01 m^{-1} for PSICAM and 0.25 ± 0.01 m^{-1} for LWCC measurements. CDOM slope results are comparable to values reported for lakes in the literature, though retrieved over different wavelength ranges [57,58]. For total suspended matter (*TSM*), the largest volume was omitted as measurements and results indicated an underestimation of the masses for these filters. Gravimetrically derived values were averaged, resulting in a concentration of 2.05 ± 0.17 mg L^{-1}. Chl-*a* concentration from HPLC analysis was 14.4 ± 0.5 µg L^{-1} which is a rather high concentration for Lake Stechlin in the upper layer, where typical values range between 0.7–9.5 (mean: 2.3) µg L^{-1} [59].

Table 1. Results from water sample and in-situ probe data analysis.

S_{CDOM} (nm^{-1})	$a_{CDOM}(440)$ (m^{-1})	C_{Chla} ($\mu g\ L^{-1}$)	C_{TSM} ($mg\ L^{-1}$)	$b_{b,TSM}$ (m^{-1})	b_{TSM} (m^{-1})
0.017 ± 0.002 [1]	0.21 ± 0.01 [1]	14.4 ± 0.5 [3]	2.05 ± 0.17	0.026 ± 0.01	2.14 ± 0.09
0.017 ± 0.002 [2]	0.25 ± 0.01 [2]	12.4 ± 1.0 [4]			

[1] PSICAM; [2] LWCC; [3] HPLC; [4] *bbe*-fluoroprobe (at 0.2 m).

Specific backscattering and specific scattering coefficients were derived from in-situ data of a spectrophotometer and a backscattering meter by normalization to the TSM concentration. The resulting coefficients are $b^*_{b,TSM}$ = 0.0128 $m^2\ g^{-1}$ and b^*_{TSM} = 1.04 $m^2\ g^{-1}$.

Vertical temperature and oxygen saturation profiles, as measured with the YSI probe, revealed a stratification of the water body with a thermocline (steepest temperature gradient) between 4.5 and 4.6 m. Temperature in the upper mixed layer of the water column (epilimnion), where in-water irradiance spectra were recorded, ranged between 18 and 19 °C. Analysis of *bbe*-fluoroprobe data showed that the total Chl-*a* concentration, as measured in-situ, was 12.4 ± 1.0 µg L^{-1} below the surface with similar values in the upper mixed layer (0–5 m).

According to the FlowCam analysis, the surface water was dominated (in terms of abundance) by *cyanobacteria* followed by *chrysophytes*, which showed up as "*diatoms*" in the *bbe*-fluoroprobe (because the fluoroprobe cannot distinguish the brown-pigmented algal groups such as *diatoms*, *chrysophytes*, *haptophytes*, and *dinoflagellates*). Retrieved abundances and cell sizes of the phytoplankton groups were converted to carbon-biomass using the equations presented in Menden-Deuer et al. [60]. This post-analysis of the image collages from FlowCam measurements revealed that the water samples (in terms of biomass) were dominated by two large phytoplankton taxa: filamentous *cyanobacteria* mainly represented by *Dolichospermum zinserlingii* (Kossinskaja) Wacklin, Hoffmann and Komárek, and

by colonial chrysophytes mainly represented by *Dinobryon sociale* (Ehrenberg) Ehrenberg. These findings agree with spectral signatures as observed in the $a^*_{ph}(\lambda)$ spectrum which, in addition to signatures of Chl-*a*, showed a maximum at around 630 nm which indicates the presence of phycobilin-containing phytoplankton such as cyanobacteria.

3.2. Water Constituent Retrieval from Downwelling Irradiance Spectra under Water

In order to test the applicability of the clear sky inversion model, above-water downwelling irradiance was modeled, as explained in Section 2.6.1. When fitting the irradiance model to E_d^+ measurements, a strong deviation in the 700–900 nm range was observed. The upwards shift of the red and near infrared parts of the measured spectrum compared to the modeled spectrum occurred in a wavelength range where vegetation has a high reflectance. This increase was observed with both the FREEDOM VIS and the RAMSES instrument. It may indicate adjacency effects caused by surrounding vegetation [61]. To minimize its impact on modeling, the fit range for deriving atmospheric parameters was limited to 350–700 nm, which was also kept for in-water hyperspectral data analysis.

Atmospheric parameters that described illumination conditions best (lowest residuum of the least-square fit), were averaged over the 30 spectra, which resulted in $\alpha = 3.00$, $\beta = 0.26$, $H_{oz} = 0.49\ cm^{-1}$, $WV = 3.35\ cm^{-1}$. Some of these parameters may not represent real physical values (e.g., typical values for α—albeit in different environments—range between 0 and 2 [62,63]). Thus, this step should be seen as a pragmatic approach to constrain the variability of downwelling irradiance that helps to reduce the number of free parameters in the subsequent step. In that step, which is fitting of underwater irradiance spectra (E_d^-), these parameters were kept constant. In addition, C_{TSM} was set to the measured mean value of 2.05 mg L^{-1} since pre-studies demonstrated a low sensitivity of the irradiance model to TSM. Also, S_{CDOM}, $b^*_{b,TSM}$ and b^*_{TSM} were kept fixed to measured values (0.017 nm^{-1}, 0.0128 $m^2\ g^{-1}$ and 1.04 $m^2\ g^{-1}$, respectively). Then, two different approaches were chosen: in the first approach, the sensor depth z was set to the actual measured depth, while in the second approach z was added to the set of fit parameters and varied during modeling. For each depth, a series of 30 individual spectra was inverted.

In the case of fixed sensor depth z, Chl-*a* concentration below the surface deviated from water sample analysis by about 35%, and from in-situ spectrofluoreometric measurements by about 56% in the first meter of water depth, but became comparable to results from water analytics at greater depths (see Figure 3a). This is in accordance with previous studies which showed that, for accurate Chl-*a* concentration retrieval, a layer of water above the sensor of at least 1 m (depending on overall water constituent concentration ranges) was required [44,51]. $a_{CDOM}(440)$, compared to results from water analytics, showed a deviation of about 57% from PSICAM and 32% from LWCC measurements. Error bars of the WASI fit-results represent the variability within the 30 spectra series.

In the case of a varied sensor depth z, an improved agreement between retrieved concentration from downwelling irradiance measurements below the water surface and results from water sample analysis was achieved (Figure 3b). Chl-*a* concentration at 40 cm water depth deviated from water sample analysis by only 5% and from in-situ spectrofluorometric measurements by 22%. CDOM absorption at 440 nm differed from PSICAM measurements by about 19% and matched the value derived from LWCC measurements. The respective values for z showed a linear correlation with measured depths, but with a deviation from the expected 1:1 relationship. The regression line (not shown) exhibited a slope of 0.88 and an offset of 0.26 m, suggesting that the sensor depth was systematically overestimated by the fit. One possible interpretation is that, under the cloudy weather conditions, more light may have entered the water body at a flat angle compared to clear sky conditions. This would result in longer absorption path lengths at a given depth. The inverse modeling may compensate this by an increased sensor depth.

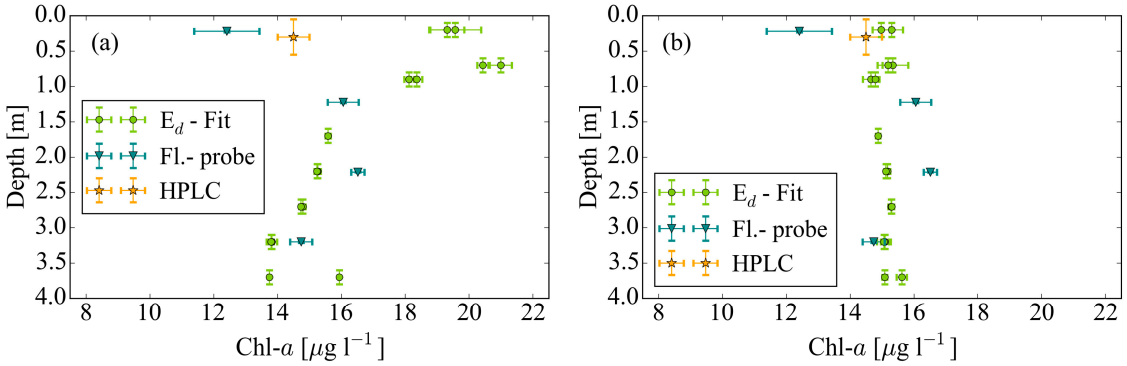

Figure 3. (**a**) Comparison of Chl-*a* concentration from in-water irradiance measurements (Ramses setup) with results from *bbe* probe scans with fixed sensor depth. (**b**) Retrieval results with varied sensor depth *z*. Two dots at a given depth represent two measured sets of 30 spectra each.

3.3. Water Constituent Retrieval from Radiance Reflectance Spectra above Water

As described in Section 2.2, the fraction of cloud cover, cloud thickness and the resulting illumination conditions were highly variable during the period of hyperspectral measurements. The irradiance spectra measured with the FREEDOM VIS spectrometer reflect this variability as can be seen in Figure 4. The plot on the left-hand side (Figure 4a) compares the spectral irradiances when the sun is obscured by clouds (M3) and when the sun is visible (M8). The changes in the magnitude of irradiance during all measurement series are illustrated in Figure 4b. The magnitude varied roughly by a factor of 3. Note that in measurement M7, instrument saturation effects were observed for a number of spectra. Therefore, 25 spectra had to be removed, which led to a reduced number for the average $E_d^+(\lambda)$ spectrum. Figure 4c depicts the relative standard deviation of irradiance spectra for all measurements (grey line) and for measurements where the sun was mostly obscured by thick clouds (M1–M3 black line). From a comparison of Figure 4b,c it can be concluded that the clouds covering the sun in measurements M1–M3 did mainly affect the magnitude of irradiance but its spectral shape remained approximately constant in the visible wavelength range.

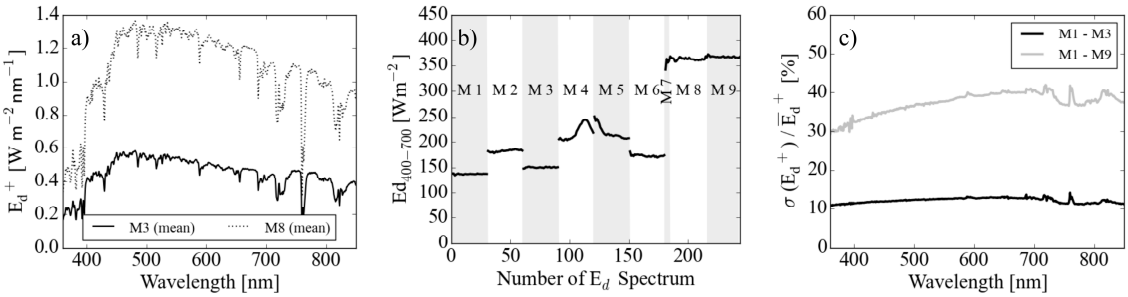

Figure 4. (**a**) Comparison of average $E_d^+(\lambda)$ spectra for different shares of clouds (M3: sun behind clouds, M8: sun visible). (**b**) Changes in the magnitude of irradiance (integrated over 400 to 700 nm) illustrating the variability in the illumination conditions. (**c**) standard deviation of $E_d^+(\lambda)$ normalized to average $E_d^+(\lambda)$ for "cloudy" measurements M1–M3 (black line) and all sets of measurements (grey line).

Radiance reflectance above water measured with the FREEDOM VIS instrument was highly variable as shown in Figure 5a. Within and between the measurement series (M1–M9) an offset-like shift in the intensities was observed. For inversion, the wavelength range was set to 360–830 nm, in order to cover the wavelength region above 700 nm that is often used to correct for sun glint [14].

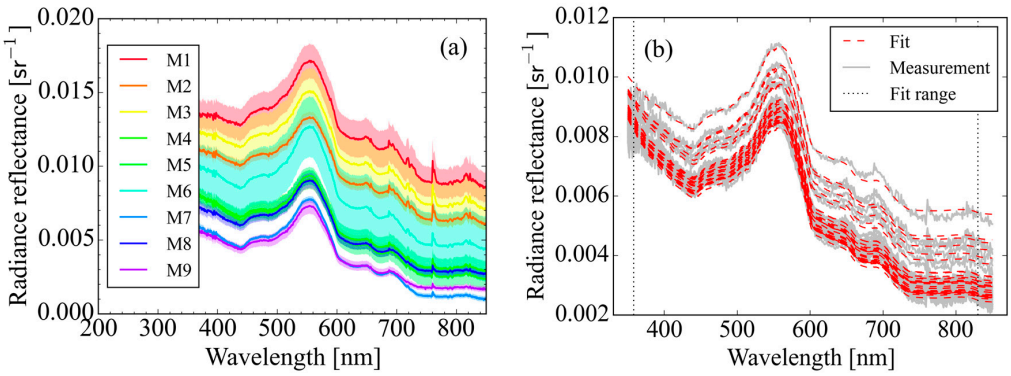

Figure 5. (**a**) Variability of radiance reflectance spectra over water; solid lines represent the mean values of the corresponding measurement series and the filled area represents the respective standard deviation per series. (**b**) Example of a reflectance series (M4) modeled with variable g_{dsr} and d_r parameters (approach G).

Fitting the individual radiance reflectance spectra without surface reflection effects (approach (K)), or a model that only varies direct and diffuse components of downwelling spectral irradiance (approach (A)) [44], were both unsuccessful (Table 2): Either the batch processing of the measurement series in WASI failed (in terms of spectral matching), or in cases where spectral matching was achieved, the inversion led to vanishing values for CDOM absorption. Therefore, variable surface reflectance components as described in Section 2.6.2 were introduced in subsequent inversion runs. Here, additional glint components were successively added to the set of fit parameters in order to determine best spectral matching with a minimal number of fit parameters. Each set of spectra (M1–M9) was fitted with the resulting approaches (B–J), respectively. Table 2 summarizes all approaches and their choice of free and fixed surface reflectance parameters during determination of Chl-*a*, TSM concentration and $a_{CDOM}(440)$. It also gives an overview of the spectral matching that was achieved.

Table 2. Spectral matching of fitted and measured radiance reflectance (series M1–M9) for different inversion approaches (A–J), where (+) and (−) indicate the quality of the spectral matching between fit and measurement curves. The (+) stands for least-squares-fit residual (normalized to max. reflectance) smaller than the average residuum by at least a factor of 2.

Fixed Surface Parameters	Varied Parameters		M1	M2	M3	M4	M5	M6	M7	M8	M9
$g_{dsr}, g_{dsa} = 0.32$ $g_{dd} = 0.02 \mid d_r = 0$	f_{dd}, f_{ds}	**A**	−	−	−	+	+	−	−	+	+
$f_{dd}, f_{ds} = 1 \mid g_{dsa}, g_{dsr}, g_{dd} = 0$	d_r	**B**	+	+	+	−	−	+	−	−	+
$f_{dd}, f_{ds} = 1 \mid g_{dsa}, g_{dsr} = 0 \mid d_r = 0$	g_{dd}	**C**	−	−	−	−	−	−	−	−	−
$f_{dd}, f_{ds} = 1 \mid g_{dsa}, g_{dd} = 0 \mid d_r = 0$	g_{dsr}	**D**	−	−	−	−	−	−	−	−	−
$f_{dd}, f_{ds} = 1 \mid g_{dsr}, g_{dd} = 0 \mid d_r = 0$	g_{dsa}	**E**	−	−	−	−	−	−	−	+	−
$f_{dd}, f_{ds} = 1 \mid g_{dsa} = 0$	g_{dsr}, g_{dd}	**F**	+	+	+	+	+	+	+	+	+
$f_{dd}, f_{ds} = 1 \mid g_{dsa} = 0$	g_{dsr}, d_r	**G**	+	+	+	+	+	+	+	+	+
$f_{dd}, f_{ds} = 1 \mid g_{dsa} = 0$	g_{dd}, g_{dsr}, d_r	**H**	+	+	+	+	+	+	+	+	+
$f_{dd}, f_{ds} = 1 \mid d_r = 0$	g_{dd}, g_{dsa}, g_{dsr}	**I**	+	+	+	+	+	+	+	+	+
$f_{dd}, f_{ds} = 1$	$g_{dd}, g_{dsa}, g_{dsr}, d_r$	**J**	+	+	+	+	+	+	+	+	+
No surface reflections	-	**K**	−	−	−	−	−	−	−	−	−

Best spectral matching with just one variable surface reflectance component was achieved with approach (B). However, this approach induced a high variability in the Chl-*a* retrieval and an unrealistically high correlation between retrieved Chl-*a* and TSM values (see Table 3). Furthermore, it resulted in vanishing CDOM absorption (similar to approach (A)), which is inconsistent with the in-situ measurements. The Chl-*a* and TSM correlation decreased with the addition of more surface

reflectance parameters (see Table 3). Approaches (F–J) all resulted in good spectral agreement between fit and measurement curves for all series of measurements. Figure 5b shows an example of such a fit result for an individual measurements series (M4) that was fitted with approach (G). The lowest variability of retrieved inversion parameters was achieved with approach (F), but here a very strong correlation of $a_{CDOM}(440)$ and g_{dsr} was observed (r = 0.84). Correlation between these parameters can be understood since both CDOM absorption and Rayleigh scattering show a continuously decaying spectral behavior towards larger wavelengths. As a compromise in the number of free fit parameters, the variability of the retrieved water constituents and the correlation with other water constituents and surface parameters, approach (G) proved to be the most successful in correcting surface reflectance in the present case study.

Table 3. Comparison of the variability (standard deviation σ) and the correlation (Spearman's rank correlation coefficient r) of water constituents retrieved from 260 above-water measurements for the surface reflectance correction approaches (B and F–J). These were the approaches that showed a reasonable spectral matching during inversion (compare Table 2).

	B	**F**	**G**	**H**	**I**	**J**
# surface parameters	1	2	2	3	3	4
Average residua	1.57×10^{-5}	1.06×10^{-5}	9.56×10^{-6}	9.47×10^{-6}	8.78×10^{-6}	9.28×10^{-6}
σ (C_{Chla} (µg L^{-1}))	1.21	0.60	0.66	0.79	1.10	0.82
σ (C_{TSM} (mg L^{-1}))	0.23	0.21	0.20	0.21	0.21	0.19
$a_{CDOM}(440)$ (m^{-1})	0.00 ± 0.00	0.11 ± 0.03	0.09 ± 0.04	0.09 ± 0.03	0.08 ± 0.03	0.10 ± 0.05
r (C_{Chla} | C_{TSM})	0.77	0.22	0.44	0.53	0.55	0.34
r (C_{Chla} | $C_{CDOM}(440)$)	−0.02	−0.36	−0.12	−0.17	−0.55	−0.44
r (C_{CDOM} | C_{TSM})	0.55	0.61	0.47	0.41	0.10	−0.42
r (C_{Chla} | surf)°	0.57 (d_r)	−0.29 (g_{dd})	−0.50 (g_{dsr})	−0.52 (g_{dsr})	0.67 (g_{dsa})	−0.46 (g_{dsr})
r (C_{TSM} | surf)°	0.55 (d_r)	0.71 (g_{dsr})	0.65 (d_r)	0.61 (d_r)	0.66 (g_{dsa})	0.44 (g_{dsa})
r ($a_{CDOM}(440)$ | surf)°	0.67 (d_r)	0.84 (g_{dsr})	0.69 (d_r)	0.64 (d_r)	0.51 (g_{dsr})	0.79 (g_{dsr})

° highest correlation of retrieved water constituent parameter with a surface parameters (which).

Water constituents retrieved with approach (G) were compared against results from water sample analysis and in-situ probe data (see Table 4). Chl-*a* concentration retrieved from above-water hyperspectral measurements differed by 37% from results from water sample analysis and by 27% from subsurface fluoroprobe data. The deviation of TSM from water sample analysis was about 33%. $a_{CDOM}(440)$ retrieved with inversion turned out to be roughly 60% (57% and 62%, respectively) smaller than results from LWCC and PSICAM measurements. The spurious correlation of retrieved water constituents with surface reflectance parameters needs to be further investigated in future studies. An extended measurement wavelength range towards the infrared, where water absorption increases, may help to further disentangle, e.g., the effect of TSM and the cloud parameter d_r on the reflectance signal.

Table 4. Water constituents as retrieved from above-water reflectance under variable cloud cover with correction of cloud reflection and surface reflection originating from Rayleigh scattered light (Errors represent the variability of the fit results)—Results from water sample analysis and in-situ probe data.

	C_{Chla} (µg L^{-1})	C_{TSM} (mg L^{-1})	$a_{CDOM}(440)$ (m^{-1})
Reflectance inversion approach (G)	9.1 ± 0.7	1.4 ± 0.2	0.09 ± 0.04
Water sample	14.4 ± 0.5	2.1 ± 0.1	$0.21/0.25 \pm 0.01/0.01$ *
Fluorescence probe	12.4 ± 1.0	-	-

* PSICAM/LWCC.

4. Conclusions

During a field campaign at Lake Stechlin in May 2016, a set of hyperspectral measurements under variable sky conditions was collected both in and above water. These spectra were complemented by a comprehensive set of water sample and in-situ probe data. The aim of this study was to evaluate the potential of water constituent retrieval from hyperspectral in-situ measurements acquired under variable cloud cover.

First, Chl-*a* concentration and $a_{CDOM}(440)$ were retrieved from in-water downwelling irradiance spectra at different depths using a clear sky model. Clouds were simulated by a dimming of the fraction of direct and diffuse irradiance as parameters of the 3C model. When varying the sensor depth along with targeted water constituents, a reasonable agreement between retrieved water constituent concentrations and the results from water sample analysis was achieved. CDOM absorption at 440 nm differed by about 19% from PSICAM measurements and coincided with LWCC measurements. The simultaneously derived phytoplankton concentration showed a deviation of 22% from in-situ probe data and a 5% deviation from HPLC measurements. The sensitivity of the E_d^--model to the sensor depth z and the improved retrieval results suggest a fitting of sensor depth for water constituent retrieval from in-water irradiance measurements.

In addition to in-water downwelling irradiance measurements, above-water radiance reflectance measurements were analyzed. In order to account for cloud effects, the 3C model was extended by a variable offset d_r resulting in the 4C spectral model for the description of surface reflectance. A common goal in analytical inversion modeling is to reduce parameters in order to minimize spectral ambiguity. Therefore, the introduction of additional fit parameters should be handled with caution. In the present study, the best set of parameters for describing surface reflectance was determined in eleven test configurations. The best results in terms of minimum number of fit parameters, lowest correlation of retrieved water constituents and surface reflectance components were achieved when treating d_r and g_{dsr} as fit parameters. The retrieved Chl-*a* concentration differed from HPLC results by about 37% and from subsurface active probe data by 27%. TSM retrieved from hyperspectral measurements deviated from gravimetrically determined values by 33%. The most critical parameter was $a_{CDOM}(440)$, which correlated with g_{dsr} and the offset d_r. Derived CDOM absorption values showed a deviation of 57% from LWCC and 62% from PSICAM measurements. Future studies should address the disentanglement of spectral surface reflection signatures from CDOM as well as from TSM signals.

The study has shown that a number of water constituents can be derived from in-water irradiance and above-water radiance reflectance measurements that were recorded under variable cloud cover. To the authors' knowledge, in-water hyperspectral irradiance measurements under varying cloud cover are rarely analyzed. The present study suggests that, even under mixed skies, in-water irradiance data may help to retrieve information on in-water substances with respect to absorbing compounds while above-water measurements allow for additional insight into the scattering compounds. Further studies are required to validate the extended 4C surface reflectance model but present results indicate its benefit for surface reflection corrections as required in all-weather remote sensing.

Lakes are very dynamic systems. They are subject to biogeochemical processes and influenced by hydrology, weather conditions and human activities such as agriculture in the catchment area and recreational use. In order to capture and to better understand these dynamics, it is crucial to minimize observation gaps. Abandoning the restriction to clear sky conditions would represent a big step forward towards regular monitoring schemes and open the door to more continuous time series of remote sensing data, e.g., from airplanes, unmanned aerial vehicles or ground-based measurements. This study demonstrates the potential of hyperspectral in-situ monitoring under weather conditions that usually constrict remote sensing.

Acknowledgments: The authors would like to thank the campaign organizers Erik Borg (DLR Neustrelitz) and Natascha Oppelt (Kiel University(CAU)), and support by Brockmann Consult GmbH, EOMAP GmbH & Co. KG, Helmholtz-Zentrum für Umwelt (UFZ), Deutsches Zentrum für Luft- und Raumfahrt (DLR), Leibniz-Institut

für Gewässerforschung- und Binnenfischerei (IGB), Kiel University (CAU) and Technical University of Munich (TUM). They are grateful for support during the campaign and measurements by Joanna Janas and Kerstin Schnalzger. Further, they would like to acknowledge Katja Dörnhöfer, Christine Fritz and Kerstin Heymann for support in campaign preparation and water sample analysis. The authors would like to thank four anonymous reviewers for their feedback which helped to improve the manuscript. A.G. was supported by the Deutsche Forschungsgemeinschaft (DFG) through the TUM International Graduate School of Science and Engineering (IGSSE) and a TUM Laura-Bassi-Fellowship. S.R. was supported by the Federal Ministry for Economic Affairs and Energy, Germany (grant no: 50EE1020). H.P.G. was supported by DFG (GR1540/21-1 and 29-1).

Author Contributions: A.G. and P.G. conceived and designed the study and wrote the paper. A.G. and S.R. performed and processed hyperspectral measurements. A.G. prepared the figures and performed inversion analysis. P.G. modified the inversion model. R.R. and C.U. performed and analyzed water sample measurements. S.A.B., J.C.N. and H.-P.G. conducted vertical profile measurements and phytoplankton composition analysis. All authors contributed to the revision and finalization of the manuscript.

Conflicts of Interest: The authors declare no conflict of interest.

List of Acronyms and Symbols (Alphabetical Order)

a_{CDOM}	Absorption coefficient of CDOM
a_{CDOM+p}	Absorption coefficient by colored dissolved and particulate matter
α	Ångström exponent of aerosol scattering
AOT	Aerosol optical thickness
${a_{ph}}^{(*)}$	(specific) Absorption coefficient of phytoplankton
${b_{TSM}}^{(*)}$	(specific) Scattering coefficient of TSM
${b_{b,TSM}}^{(*)}$	(specific) Backscattering coefficient of TSM
β	Turbidity coefficient
C_{Chla}	Concentration of Chl-*a*
C_{TSM}	Concentration of TSM
CDOM	Colored dissolved organic matter
Chl-*a*	Chlorophyll-*a*
d_r	Cloud offset to surface reflectance
E_d	Downwelling irradiance
E_{dd}	Downwelling irradiance component from direct sunlight
E_{dsa}	Downwelling irradiance component from light scattered by aerosols (Mie scattering)
E_{dsr}	Downwelling irradiance component from light scattered by molecules (Rayleigh scattering)
f_{dd}	Relative intensity of direct component of downwelling irradiance
f_{dd}	Relative intensity of diffuse component downwelling irradiance
f_{dsa}	Relative intensity of aerosol component of downwelling irradiance
f_{dsr}	Relative intensity of Rayleigh component of downwelling irradiance
FWHM	Full width at half maximum
g_{dd}	Reflection factor for direct component of downwelling irradiance
g_{dsa}	Reflection factor for aerosol component of downwelling irradiance
g_{dsr}	Reflection factor for contribution of Rayleigh component of downwelling irradiance
H_{oz}	Scale height of ozone
HPLC	High performance liquid chromatography
λ	Wavelength
L_{sky}	Sky radiance
L_u	Upwelling radiance
LWCC	Liquid waveguide capillary cell
PSICAM	Point-source integrating cavity absorption meter
r	Spearman's correlation coefficient
R_{rs}	Remote sensing reflectance
R_{surf}	Surface reflectance

RSR	Remote sensing ratio
S_{CDOM}	Spectral slope parameter of CDOM absorption
σ	Standard deviation
T	Temperature
TSM	Total suspended matter
VIS	Visible wavelength range
WASI	Inversion software "water color simulator"
WV	Scale height of precipitable water in the atmosphere
z	Sensor depth
−	Reference to measurement in water
+	Reference to measurement above water
3C	Three component surface reflectance model
4C	Four component surface reflectance model

References

1. Platt, T.; Hoepffner, N.; Stuart, V.; Brown, C. (Eds.) *Why Ocean Colour? The Societal Benefits of Ocean-Colour Technology*; Vol. No. 7, Reports of the International Ocean Colour Coordinating Group; IOCCG: Dartmouth, NS, Canada, 2008.
2. Vörösmarty, C.J.; Hoekstra, A.Y.; Bunn, S.E.; Conway, D.; Gupta, J. Fresh water goes global. *Science* **2015**, *349*, 478–479. [CrossRef] [PubMed]
3. Hestir, E.L.; Brando, V.E.; Bresciani, M.; Giardino, C.; Matta, E.; Villa, P.; Dekker, A.G. Measuring freshwater aquatic ecosystems: The need for a hyperspectral global mapping satellite mission. *Remote Sens. Environ.* **2015**, *167*, 181–195. [CrossRef]
4. Dörnhöfer, K.; Oppelt, N. Remote sensing for lake research and monitoring—Recent advances. *Ecol. Indic.* **2016**, *64*, 105–122. [CrossRef]
5. Martinez-Vicente, V.; Simis, S.; Alegre, R.; Land, P.; Groom, S. Above-water reflectance for the evaluation of adjacency effects in Earth observation data: Initial results and methods comparison for near-coastal waters in the Western Channel, UK. *J. Eur. Opt. Soc. Rapid Publ.* **2013**, *8*. [CrossRef]
6. Giardino, C.; Bresciani, M.; Valentini, E.; Gasperini, L.; Bolpagni, R.; Brando, V.E. Airborne hyperspectral data to assess suspended particulate matter and aquatic vegetation in a shallow and turbid lake. *Remote Sens. Environ.* **2015**, *157*, 48–57. [CrossRef]
7. Kutser, T.; Paavel, B.; Verpoorter, C.; Ligi, M.; Soomets, T.; Toming, K.; Casal, G. Remote Sensing of Black Lakes and Using 810 nm Reflectance Peak for Retrieving Water Quality Parameters of Optically Complex Waters. *Remote Sens.* **2016**, *8*, 497. [CrossRef]
8. Shang, S.; Lee, Z.; Lin, G.; Hu, C.; Shi, L.; Zhang, Y.; Li, X.; Wu, J.; Yan, J. Sensing an intense phytoplankton bloom in the western Taiwan Strait from radiometric measurements on a UAV. *Remote Sens. Environ.* **2017**, *198*, 85–94. [CrossRef]
9. Simis, S.G.; Olsson, J. Unattended processing of shipborne hyperspectral reflectance measurements. *Remote Sens. Environ.* **2013**, *135*, 202–212. [CrossRef]
10. Wernand, M. Guidelines for (ship-borne) auto-monitoring of coastal and ocean colour. In Proceedings of the Ocean Optics XVI, Santa Fe, NM, USA, 18–22 November 2002; Volume 13.
11. Zibordi, G.; Strömbeck, N.; Mélin, F.; Berthon, J.F. Tower-based radiometric observations at a coastal site in the Baltic Proper. *Estuar. Coast. Shelf Sci.* **2006**, *69*, 649–654. [CrossRef]
12. Brando, V.; Keen, R.; Daniel, P.; Baumeister, A.; Nethery, M.; Baumeister, H.; Hawdon, A.; Swan, G.; Mitchell, R.; Campbell, S.; et al. The Lucinda Jetty Coastal Observatory's role in satellite ocean colour calibration and validation for Great Barrier Reef coastal waters. In Proceedings of the OCEANS 2010 IEEE, Sydney, Australia, 24–27 May 2010; pp. 1–8.
13. Cox, C.; Munk, W. *Slopes of the Sea Surface Deduced from Photographs of Sun Glitter*; Bulletin of the Scripps Institution of Oceanography; University of California Press: San Diego, CA, USA, 1956.
14. Kay, S.; Hedley, J.D.; Lavender, S. Sun Glint Correction of High and Low Spatial Resolution Images of Aquatic Scenes: A Review of Methods for Visible and Near-Infrared Wavelengths. *Remote Sens.* **2009**, *1*, 697–730. [CrossRef]

15. Groetsch, P.M.M.; Gege, P.; Simis, S.G.H.; Eleveld, M.A.; Peters, S.W.M. Validation of a spectral correction procedure for sun and sky reflections in above-water reflectance measurements. *Opt. Express* **2017**, *25*, A742–A761. [CrossRef] [PubMed]
16. Mobley, C.D. Estimation of the remote-sensing reflectance from above-surface measurements. *Appl. Opt.* **1999**, *38*, 7442–7455. [CrossRef] [PubMed]
17. Fougnie, B.; Frouin, R.; Lecomte, P.; Deschamps, P.Y. Reduction of skylight reflection effects in the above-water measurement of diffuse marine reflectance. *Appl. Opt.* **1999**, *38*, 3844–3856. [CrossRef] [PubMed]
18. Hirata, T.; Hardman-Mountford, N.; Aiken, J.; Fishwick, J. Relationship between the distribution function of ocean nadir radiance and inherent optical properties for oceanic waters. *Appl. Opt.* **2009**, *48*, 3129–3138. [CrossRef] [PubMed]
19. Gege, P.; Grötsch, P. A spectral model for correcting sunglint and skyglint. In Proceedings of the Ocean Optics XXIII, Victoria, BC, Canada, 23–28 October 2016; pp. 1–10.
20. Gregg, W.W.; Carder, K.L. A simple spectral solar irradiance model for cloudless maritime atmospheres. *Limnol. Oceanogr.* **1990**, *35*, 1657–1675. [CrossRef]
21. Dörnhöfer, K.; Göritz, A.; Gege, P.; Pflug, B.; Oppelt, N. Water Constituents and Water Depth Retrieval from Sentinel-2A—A First Evaluation in an Oligotrophic Lake. *Remote Sens.* **2016**, *8*, 941. [CrossRef]
22. Gege, P. A case study at Starnberger See for hyperspectral bathymetry mapping using inverse modeling. In Proceedings of the WHISPERS 2014, Lausanne, Switzerland, 25–27 June 2014; pp. 1–4.
23. Schenck, H. On the Focusing of Sunlight by Ocean Waves. *J. Opt. Soc. Am.* **1957**, *47*, 653–657. [CrossRef]
24. Zaneveld, J.R.V.; Boss, E.; Barnard, A. Influence of surface waves on measured and modeled irradiance profiles. *Appl. Opt.* **2001**, *40*, 1442–1449. [CrossRef] [PubMed]
25. Gege, P. Analytic model for the direct and diffuse components of downwelling spectral irradiance in water. *Appl. Opt.* **2012**, *51*, 1407–1419. [CrossRef] [PubMed]
26. Kim, H.C.; Hofmann, E.E. Evaluation and derivation of cloud-cover algorithms for calculation of surface irradiance in sub-Antarctic and Antarctic environments. *Antarct. Sci.* **2005**, *17*, 135–150. [CrossRef]
27. Toole, D.A.; Siegel, D.A.; Menzies, D.W.; Neumann, M.J.; Smith, R.C. Remote-sensing reflectance determinations in the coastal ocean environment: Impact of instrumental characteristics and environmental variability. *Appl. Opt.* **2000**, *39*, 456–469. [CrossRef] [PubMed]
28. Albert, A.; Mobley, C. An analytical model for subsurface irradiance and remote sensing reflectance in deep and shallow case-2 waters. *Opt. Express* **2003**, *11*, 2873–2890. [CrossRef] [PubMed]
29. Albert, A. Inversion Technique for Optical Remote Sensing in Shallow Water. Ph.D. Thesis, Universität Hamburg, Hamburg, Germany, 2005.
30. Richter, D.; Koschel, R. Hydrometeorology of the Lake Stechlin area. In *Lake Stechlin: A Temperate Oligotropihic Lake*; Casper, S.J., Ed.; Springer: Dordrecht, The Netherlands, 1985; pp. 41–86.
31. Casper, S.J. (Ed.) *Lake Stechlin: A Temperate Oligotrophic Lake*; Springer Science & Business Media: Berlin/Heidelberg, Germany, 2012; Volume 58.
32. Röttgers, R.; Häse, C.; Doerffer, R. Determination of the particulate absorption of microalgae using a point-source integrating-cavity absorption meter: Verification with a photometric technique, improvements for pigment bleaching, and correction for chlorophyll fluorescence. *Limnol. Oceanogr. Methods* **2007**, *5*, 1–12. [CrossRef]
33. Röttgers, R.; Doerffer, R. Measurements of optical absorption by chromophoric dissolved organic matter using a point-source integrating-cavity absorption meter. *Limnol. Oceanogr. Methods* **2007**, *5*, 126–135. [CrossRef]
34. Miller, R.L.; Belz, M.; Castillo, C.D.; Trzaska, R. Determining CDOM absorption spectra in diverse coastal environments using a multiple pathlength, liquid core waveguide system. *Cont. Shelf Res.* **2002**, *22*, 1301–1310. [CrossRef]
35. Röttgers, R.; Heymann, K.; Krasemann, H. Suspended matter concentrations in coastal waters: Methodological improvements to quantify individual measurement uncertainty. *Estuar. Coast. Shelf Sci.* **2014**, *151*, 148–155. [CrossRef]
36. Zapata, M.; Rodríguez, F.; Garrido, J.L. Separation of chlorophylls and carotenoids from marine phytoplankton: A new HPLC method using a reversed phase C8 column and pyridine-containing mobile phases. *Mar. Ecol. Prog. Ser.* **2000**, *195*, 29–45. [CrossRef]

37. Jakobsen, H.H.; Carstensen, J. FlowCAM: Sizing cells and understanding the impact of size distributions on biovolume of planktonic community structure. *Aquat. Microb. Ecol.* **2011**, *65*, 75–87. [CrossRef]
38. TriOS GmbH, G. RAMSES ACC-VIS and ARC-VIS Radiometer. Available online: http://www.trios.de/en/products/sensors/ramses.html (accessed on 25 January 2017).
39. Ibsen Photonics Inc. FREEDOM VIS FSV-305. Available online: http://ibsen.com/products/oem-spectrometers/freedom-spectrometers/freedom-vis/ (accessed on 25 January 2017).
40. Labsphere. Spectralon, Diffuse Reflectance Targets. 10% Nominal Reflectance Value. SRT 10-050. Available online: https://www.labsphere.com/site/assets/files/1828/spectralon_targets.pdf (accessed on 25 January 2017).
41. Mobley, C. Ocean Color Webbook: Normalized Reflectances. 2016. Available online: http://www.oceanopticsbook.info/view/atmospheric_correction/normalized_reflectances (accessed on 8 September 2017).
42. PyEphem. Available online: http://rhodesmill.org/pyephem/index.html (accessed on 6 February 2017).
43. Bird, R.E.; Riordan, C. Simple Solar Spectral Model for Direct and Diffuse Irradiance on Horizontal and Tilted Planes at the Earth's Surface for Cloudless Atmospheres. *J. Clim. Appl. Meteorol.* **1986**, *25*, 87–97. [CrossRef]
44. Gege, P. Estimation of phytoplankton concentration from downwelling irradiance measurements in water. *Isr. J. Plant Sci.* **2012**, *60*, 193–207. [CrossRef]
45. Gege, P.; Pinnel, N. Sources of variance of downwelling irradiance in water. *Appl. Opt.* **2011**, *50*, 2192–2203. [CrossRef] [PubMed]
46. Bricaud, A.; Morel, A.; Prieur, L. Absorption by dissolved organic matter of the sea (yellow substance) in the UV and visible domains1. *Limnol. Oceanogr.* **1981**, *26*, 43–53. [CrossRef]
47. Carder, K.L.; Steward, R.G.; Harvey, G.R.; Ortner, P.B. Marine humic and fulvic acids: Their effects on remote sensing of ocean chlorophyll. *Limnol. Oceanogr.* **1989**, *34*, 68–81. [CrossRef]
48. Chami, M.; Shybanov, E.B.; Churilova, T.Y.; Khomenko, G.A.; Lee, M.E.G.; Martynov, O.V.; Berseneva, G.A.; Korotaev, G.K. Optical properties of the particles in the Crimea coastal waters (Black Sea). *J. Geophys. Res. Oceans* **2005**, *110*, C11020. [CrossRef]
49. Babin, M.; Morel, A.; Fournier-Sicre, V.; Fell, F.; Stramski, D. Light scattering properties of marine particles in coastal and open ocean waters as related to the particle mass concentration. *Limnol. Oceanogr.* **2003**, *48*, 843–859. [CrossRef]
50. Gege, P. Software WASI-2D. Available online: http://www.ioccg.org/data/software.html (accessed on 27 January 2016).
51. Linnemann, K.; Gege, P.; Rößler, S.; Schneider, T.; Melzer, A. CDOM retrieval using measurements of downwelling irradiance. In Proceedings of the SPIE Remote Sensing 2013, Dresden, Germany, 23–26 September 2013.
52. Mobley, C.D. *Light and Water*; Academic Press: San Diego, CA, USA, 1994.
53. Lee, Z.; Carder, K.L.; Mobley, C.D.; Steward, R.G.; Patch, J.S. Hyperspectral remote sensing for shallow waters. I. A semianalytical model. *Appl. Opt.* **1998**, *37*, 6329–6338. [CrossRef] [PubMed]
54. Albert, A.; Gege, P. Inversion of irradiance and remote sensing reflectance in shallow water between 400 and 800 nm for calculations of water and bottom properties. *Appl. Opt.* **2006**, *45*, 2331–2343. [CrossRef] [PubMed]
55. Lee, Z.; Carder, K.L.; Mobley, C.D.; Steward, R.G.; Patch, J.S. Hyperspectral remote sensing for shallow waters: 2. Deriving bottom depths and water properties by optimization. *Appl. Opt.* **1999**, *38*, 3831–3843. [CrossRef] [PubMed]
56. Gege, P. Chapter 2: Radiative transfer theory for inland waters. In *Bio-Optical Modeling and Remote Sensing of Inland Waters*, 1st ed.; Mishra, D., Ogashawara, I., Gitelson, A., Eds.; Elsevier: Amsterdam, The Netherlands, 2017; pp. 154–196.
57. Ylöstalo, P.; Kallio, K.; Seppälä, J. Absorption properties of in-water constituents and their variation among various lake types in the boreal region. *Remote Sens. Environ.* **2014**, *148*, 190–205. [CrossRef]
58. Kutser, T.; Koponen, S.; Kallio, K.Y.; Fincke, T.; Paavel, B. Chapter 4: Bio-optical Modeling of Colored Dissolved Organic Matter. In *Bio-Optical Modeling and Remote Sensing of Inland Waters*, 1st ed.; Mishra, D., Ogashawara, I., Gitelson, A., Eds.; Elsevier: Amsterdam, The Netherlands, 2017; p. 106.
59. Kasprzak, P.; Padisák, J.; Koschel, R.; Krienitz, L.; Gervais, F. Chlorophyll a concentration across a trophic gradient of lakes: An estimator of phytoplankton biomass? *Limnologica* **2008**, *38*, 327–338. [CrossRef]

60. Menden-Deuer, S.; Lessard, E.J. Carbon to volume relationships for dinoflagellates, diatoms, and other protist plankton. *Limnol. Oceanogr.* **2000**, *45*, 569–579. [CrossRef]
61. Groetsch, P.M.M.; Gege, P.; Simis, S.G.H.; Eleveld, M.A.; Peters, S.W.M. Variability of adjacency effects in sky reflectance measurements. *Opt. Lett.* **2017**, *42*, 3359–3362. [CrossRef] [PubMed]
62. Russell, P.B.; Bergstrom, R.W.; Shinozuka, Y.; Clarke, A.D.; DeCarlo, P.F.; Jimenez, J.L.; Livingston, J.M.; Redemann, J.; Dubovik, O.; Strawa, A. Absorption Angstrom Exponent in AERONET and related data as an indicator of aerosol composition. *Atmos. Chem. Phys.* **2010**, *10*, 1155–1169. [CrossRef]
63. Ran, L.; Deng, Z.; Wang, P.; Xia, X. Black carbon and wavelength-dependent aerosol absorption in the North China Plain based on two-year aethalometer measurements. *Atmos. Environ.* **2016**, *142*, 132–144. [CrossRef]

B Journal publications related to this thesis (full paper peer review)

B.1 Publication IV

Dörnhöfer K., Göritz A., Gege P., Pflug B., Oppelt N.
Water Constituents and Water Depth Retrieval from Sentinel-2A – A First Evaluation in an Oligotrophic Lake
Remote Sensing 2016, Vol. 8, Issue 11, 941.

This publication is part of the doctoral project of and mainly authored by Katja Dörnhöfer (Christian-Albrechts-Universität, Kiel). It does therefore not form part of the present thesis. It can be accessed at: `https://doi.org/10.3390/rs8110941`.

C Presentations related to this thesis

C.1 Selected oral presentations

- Göritz A., Identification and Monitoring of Toxic Cyanobacteria - the IMOTOX project, Student introduction (short oral) during the IOCCG summer lecture series (July 2014), Villefranche, France.
- Göritz A., Lab spectroscopy experiments for optical remote sensing of water bodies, Seminar at the Chair of Remote Sensing Technology (September 2014), Technical University Munich, Germany.
- Göritz A., Gege P., Absorption and fluorescence characteristics of colored dissolved organic matter: A case study in pre-alpine lakes, International Workshop on Organic Matter Spectroscopy (September 2015), Sopot, Poland.
- Göritz A., Remote Sensing activities within the IMOTOX project, FA Water Midterm Meeting (presented by Gege P. in April 2016), Freising, Germany.
- Göritz A., Monitoring of phytoplankton and CDOM linking hyperspectral reflectance with in-situ measurements: A case study at lake Stechlin, Workshop Inland Water Remote Sensing (September 2016), Helmholtz Zentrum Geesthacht, Germany.
- Göritz A., Modelling the optical properties of cyanobacteria, Doctoral days at the Institute of Remote Sensing Technology (September 2016), Oberpfaffenhofen, Germany.
- Scherer P. & Göritz A., Von der Mikrobiologie zur Fernerkundung: Cyanobakterien in Inlandgewässern, Umweltbundesamt (May 2017), Dessau-Roßlau, Germany. (*invited talk*)
- Göritz A., Phytoplankton classification using remote sensing techniques, Seminar at the Department of Experimental Methods (January 2018), German Aerospace Center, Oberpfaffenhofen, Germany.

C.2 Selected poster presentations

- Ruber J., Scherer P., Kar A., Göritz A., Zwirglmaier K., Geist J., Gege P., Bamler R., IMOTOX - Identification and monitoring of toxic cyanobacteria (Water 01), 8th IGSSE Forum Raitenhaslach (July 2014), Burghausen, Germany.
- Göritz A., Gege P., Analysis of CDOM absorption and fluorescence spectra to explore storage degradation effects, Ocean Optics XXII (October 2014), Portland USA.
- Göritz A., Gege P., Towards an identification and monitoring of Harmful Algae Blooms (HABs) using optical remote sensing techniques, TUM/DLR summer school (June 2015), Obergurgl, Austria.
- Ruber J., Scherer P., Kar A., Göritz A., Zwirglmaier K., Geist J., Gege P., Bamler R., IMOTOX - Identification and monitoring of toxic cyanobacteria (Water 01), 9th IGSSE Forum Raitenhaslach (July 2015), Burghausen, Germany. (*Vodafone poster award*)
- Ruber J., Scherer P., Göritz A., Zwirglmaier K., Geist J., Gege P., Bamler R., IMOTOX - Identification and monitoring of toxic cyanobacteria (Water 01), 10th IGSSE Forum Raitenhaslach (June 2016), Burghausen, Germany.
- Göritz A., Gege P., A study on absorption and fluorescence characteristics of cyanobacteria: In vivo spectroscopy for remote sensing algorithms, XXXIII Congress of the International Society of Limnology (August 2016), Torino, Italy.
- Ruber J., Scherer P., Göritz A., Riedel S., Zwirglmaier K., Raeder U., Geist J., Gege P., Bamler R., IMOTOX - Identifzierung und Monitoring giftiger Cyanobakterien, Raitenhaslach opening exhibition (June 2017), Burghausen, Germany.
- Ruber J., Scherer P., Göritz A., Riedel S., Zwirglmaier K., Raeder U., Geist J., Gege P., Bamler R., IMOTOX - quo vadis? Identification and monitoring of toxic cyanobacteria (Water 01), 11th IGSSE Forum (June 2017), Raitenhaslach, Burghausen, Germany.